WL-TR-97-3079

UNSTRUCTURED GRID ASSESSMENT FOR VISCOUS FLOW SIMULATIONS

T.R. Michal

McDonnell Douglas
P.O. Box 516
St. Louis, MO 63166-0516

FLIGHT DYNAMICS DIRECTORATE
WRIGHT LABORATORY
AIR FORCE MATERIEL COMMAND
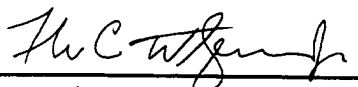WRIGHT-PATTERSON AFB OH 45433-7562

DTIC QUALITY INSPECTED 4
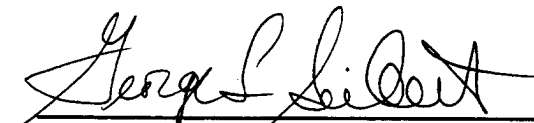
19980225 083

NOTICE

USING GOVERNMENT DRAWINGS, SPECIFICATIONS, OR OTHER DATA INCLUDED IN THIS DOCUMENT FOR ANY PURPOSE OTHER THAN GOVERNMENT PROCUREMENT DOES NOT IN ANY WAY OBLIGATE THE US GOVERNMENT. THE FACT THAT THE GOVERNMENT FORMULATED OR SUPPLIED THE DRAWINGS, SPECIFICATIONS, OR OTHER DATA DOES NOT LICENSE THE HOLDER OR ANY OTHER PERSON OR CORPORATION; OR CONVEY ANY RIGHTS OR PERMISSION TO MANUFACTURE, USE, OR SELL ANY PATENTED INVENTION THAT MAY RELATE TO THEM.

THIS REPORT IS RELEASABLE TO THE NATIONAL TECHNICAL INFORMATION SERVICE (NTIS). AT NTIS, IT WILL BE AVAILABLE TO THE GENERAL PUBLIC, INCLUDING FOREIGN NATIONS.

THIS TECHNICAL REPORT HAS BEEN REVIEWED AND IS APPROVED FOR PUBLICATION.

Frank C. Witzeman, Jr.
CFD Research Branch

George L. Seibert, Chief
CFD Research Branch

Dennis Sedlock, Chief
Aeromechanics Division

IF YOUR ADDRESS HAS CHANGED, IF YOU WISH TO BE REMOVED FROM OUR MAILING LIST, OR IF THE ADDRESSEE IS NO LONGER EMPLOYED BY YOUR ORGANIZATION PLEASE NOTIFY WL/_FIMC___WRIGHT-PATTERSON AFB OH 45433_-7913_ TO HELP MAINTAIN A CURRENT MAILING LIST.

Do not return copies of this report unless contractual obligations or notice on a specific document requires its return.

REPORT DOCUMENTATION PAGE

1. AGENCY USE ONLY *(Leave blank)*	2. REPORT DATE	3. REPORT TYPE AND DATES COVERED
	JULY 1997	FINAL, 1 JULY 96 - 31 JULY 97

4. TITLE AND SUBTITLE

UNSTRUCTURED GRID ASSESSMENT FOR VISCOUS FLOW SIMULATIONS

6. AUTHOR(S)

MICHAL, T.R.

5. FUNDING NUMBERS

C: F33615-96-D-3003
PE: 62201
PR: 2404
TA: 10
WU: TT

7. PERFORMING ORGANIZATION NAME(S) AND ADDRESS(ES)

MCDONNELL DOUGLAS

PO Box 516

ST. LOUIS, MO 63166-0516

8. PERFORMING ORGANIZATION REPORT NUMBER

9. SPONSORING/MONITORING AGENCY NAME(S) AND ADDRESS(ES)

FLIGHT DYNAMICS DIRECTORATE
WRIGHT LABORATORY
AIR FORCE MATERIEL COMMAND
WRIGHT PATTERSON AIR FORCE BASE, OHIO 45433-7734
POC: FRANK WITZEMAN, WL/FIMC (937)255-3788

10. SPONSORING/MONITORING AGENCY REPORT NUMBER

WL-TR-97-3079

11. SUPPLEMENTARY NOTES

12a. DISTRIBUTION AVAILABILITY STATEMENT

APPROVED FOR PUBLIC RELEASE; DISTRIBUTION UNLIMITED

12b. DISTRIBUTION CODE

13. ABSTRACT *(Maximum 200 words)*

A systematic assessment of the strengths and weaknesses of three viscous flowfield simulation methods for unstructured grids has been performed. The methods evaluated represent the primary viscous unstructured griding approaches currently in use including anisotropic tetrahedral, zonal hybrid (hexahedral/tetrahedral), and grids containing a mixture of cell types. The strengths and weaknesses of each method have been identified and grid resolution guidelines have been developed through a systematic study of the flow fields about a flat plate and ONERA M6 wing. Run conditions were selected to provide comparisons of a wide variety of flow field features including transonic and separated flows. Solutions are compared with theoretical and experimental data, and computational requirements of the three methods are compared to provide a relative evaluation of each method's accuracy and efficiency.

Each of the unstructured grid approaches was found to provide adequate solution accuracy provided sufficient grid resolution and quality is employed. The zonal hybrid approach was found to provide the best solution computation efficiency at the expense of a long grid generation cycle time. The tetrahedral approach provided the fastest grid generation cycle time and the mixed cell approach provides the most flexibility.

14. SUBJECT TERMS

COMPUTATIONAL FLUID DYNAMICS
UNSTRUCTURED GRIDS

15. NUMBER OF PAGES
89

16. PRICE CODE

17. SECURITY CLASSIFICATION OF REPORT	18. SECURITY CLASSIFICATION OF THIS PAGE	19. SECURITY CLASSIFICATION OF ABSTRACT	20. LIMITATION OF ABSTRACT
UNCLASSIFIED	UNCLASSIFIED	UNCLASSIFIED	SAR

TABLE OF CONTENTS

APPENDICES 65

LIST OF FIGURES

LIST OF TABLES

1. INTRODUCTION AND SUMMARY

The advent of unstructured grid technology has greatly reduced grid generation time for complex configurations and has the potential to increase solution quality through techniques like grid adaptation. Until recently these benefits have been limited to inviscid applications due to the difficulty of generating unstructured tetrahedral grids appropriate for viscous computations. These problems require grid clustering normal to the surface to resolve the boundary layer. Standard unstructured tetrahedral grid generation methods attempt to maintain a unitary aspect ratio causing the grids to become excessively large in the viscous layer. Recently, a wide variety of approaches have arisen in an attempt to overcome these difficulties. This variety of approaches makes it difficult to select a direction for future development of unstructured grid methods. This report documents a systematic assessment of the relative strengths and weaknesses of three new approaches to unstructured grid viscous flow field simulation. This information will help guide future development efforts and will help the computational fluid dynamics (CFD) user select an appropriate unstructured grid approach for a given application based on accuracy and efficiency requirements.

The methods evaluated in this study are the VGRID/USM3D, MACGS/NASTD, and TETMESH /Cobalt grid generation/flow solver software packages developed by NASA Langley Research Center, McDonnell Douglas Corporation (MDC), and Air Force WL/FIMC respectively. Each of these methods use a different unstructured grid cell topology to model the viscous layer. An illustration of the unstructured grid types used with each approach is shown in Figure 1. The VGRID/USM3D software package uses tetrahedral elements throughout the domain with anisotropic stretching near the surface. This approach will be referred to as the tetrahedral approach. The zonal hybrid approach used by the MACGS/NASTD software package combines a structured grid consisting of hexahedral elements at the surface with tetrahedral elements defined away from the body. The TETMESH/Cobalt software package uses semi-structured layers of grid cells in the viscous region where the layers are normal extrusions of the triangular surface grid resulting in prismatic elements. These elements merge with a tetrahedral grid defined outside the viscous region. This approach will be referred to as the mixed cell approach.

Each of these modeling approaches have a unique set of advantages and disadvantages. The zonal hybrid approach, while being straight forward to implement, does not offer the geometric flexibility of the tetrahedral and mixed cell approaches. This approach requires a structured grid to be defined near the geometry surface which typically takes a long time to generate. The triangular surface grids used in the tetrahedral and mixed cell methods are generally easier to generate but provide poor resolution of highly curved geometries. Volume grid generation is much easier for the tetrahedral approach than for the zonal hybrid or mixed cell methods which require separate grid generation techniques in the viscous and farfield regions. However, grid requirements for anisotropic tetrahedral grids are not well known since relatively few tetrahedral viscous computations have been performed.

1

Anisotropic Tetrahedral	Hybrid Struct/Unstructured	Prismatic
(VGRID/USM3D)	(MACGS/NASTD)	(TETMESH/COBALT)
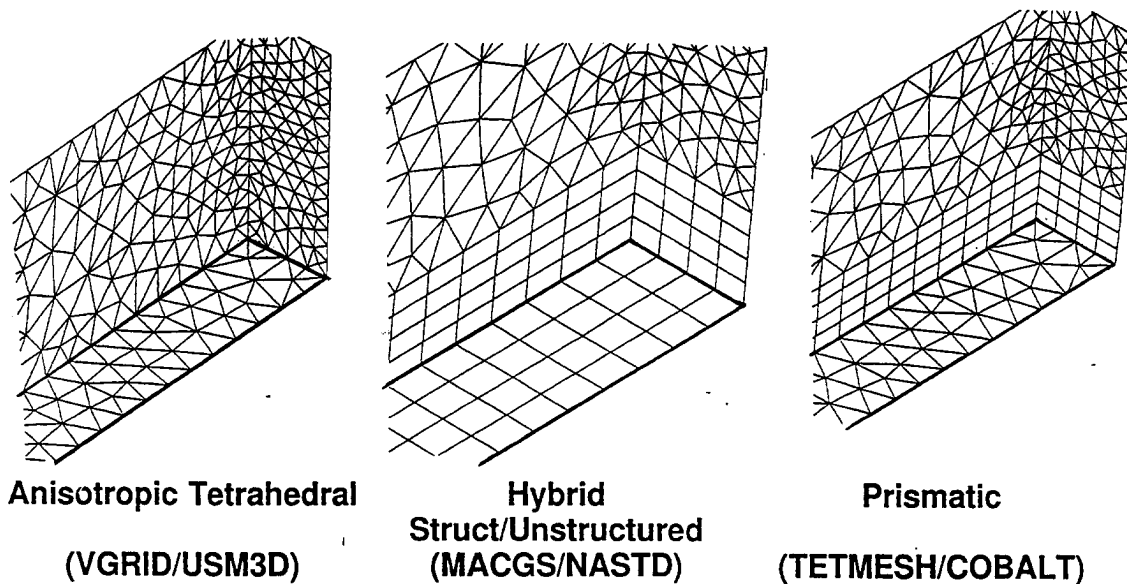
Figure 1. Three Flat Plate Unstructured Grid Topologies

The choice of grid cell shape can have a large influence on flow solution efficiency. For instance, solution computation on a tetrahedral grid will result in at least four times more work per node than a hexahedral grid. However, tetrahedral grids may require fewer nodes to obtain the same level of accuracy due to the increased directional information available at each node. Solutions computed on zonal hybrid grids can take advantage of the structured data storage to provide very high efficiencies, but generally contain more grid cells than tetrahedral grids.

In order to identify the best and worst attributes of each method, a comprehensive study of the strengths and weaknesses of these approaches has been performed. This study includes an assessment of the relative accuracy, efficiency, robustness and ease of use of each method.

An essential element in performing an objective assessment is the determination of the grid resolution required by each method. A grid that is too coarse will adversely affect solution accuracy while a grid that is too fine will reflect poorly on the method's efficiency. In this study, grid resolution requirements were established by performing a grid refinement study on laminar and turbulent flat plates over a range of Reynolds numbers. For each unstructured grid method a study was performed to determine the spacing of the first point off the wall and the number of points across the boundary layer required to obtain an accurate solution.

Once the grid resolution requirements were known, the viscous prediction capabilities of each method were evaluated by comparing solutions for sample test cases. These cases were selected to cover a wide range of flow field physics. Solutions about the ONERA M6 wing were generated at two run conditions. At the first run condition of Mach 0.7, angle of attack of 0.0 degrees, and Reynolds number of 11.7 million the flowfield is subsonic and remains attached across the entire wing span. At the second run condition of Mach 0.85, angle of attack of 5.0 degrees and Reynolds number of 11.7 million, the flow field contains several complex viscous interactions including shock-induced separation over the outer one third of the wing.

For each method, comparisons of solution accuracy, computational requirements, and grid generation time were made. The convergence properties are compared and an assessment of the ease of use of the grid generation and flow solver software is made.

2. SOFTWARE INSTALLATION

In this section a short description of each of the three software packages is given. The steps that were employed in installing this software on various computer systems are also documented.

The VGRID unstructured grid generation system was developed by ViGYAN, Inc. under contract from NASA Langley Research Center. A complete description of the method is provided in Reference (1). VGRID is based on the Advancing-Front Method for the generation of Euler tetrahedral grids and the Advancing-Layers Method for producing thin-layered tetrahedral grids suitable for computation of viscous fluid flows. A multi-directional grid stretching substantially decreases the final grid size. A graphic user interface tool, Grid Tool, is available for converting given Computer Aided Design (CAD) geometries into Non-Uniform Rational B-Splines (NURBS) surfaces for convenient manipulation and geometry modification. After a volume grid is generated, a grid postprocessing program POSTGRID improves the grid quality by replacing isolated defects in the volume grid using local remeshing. The USM3D flow solver was developed by Neal Frink at NASA Langley Research Center. The methodology is based on an upwind, tetrahedral cell-centered finite-volume scheme and uses a Spalart-Allmaras one-equation turbulence model coupled with a wall function to reduce the number of cells required in the sublayer region of the boundary layer. Detailed descriptions and results from the method are presented in Reference (2).

The VGRID grid generation system was distributed by NASA Langley Research Center. The distribution uses a keying system whereby each software executable is keyed to a specific machine and ip address. The VGRID system executables are only available for Silicon Graphics computer systems. The USM3D software was distributed as source code with a Makefile valid for several computer systems (not including HP). Very minor changes were required to the Makefile to compile and install the USM3D software on the MDC Hewlett Packard (HP) and government supplied CRAY computer systems.

The McDonnell Aircraft Computational Grid System (MACGS) is a versatile interactive system that includes capabilities for geometry manipulation, structured, unstructured and chimera grid generation, and boundary condition specification. MACGS consists of the modules, ZONI3G, GMAN, and GPRO. ZONI3G is used for boundary grid generation, GMAN contains the volume grid generation, and GPRO performs grid manipulations such as scaling transformations etc. The NAvier Stokes Time Dependent (NASTD) flow solver is the primary flow solver in use at MDC/St. Louis. This zonal flow solver contains capabilities for structured, unstructured and chimera grids. NASTD and MACGS have been used on a wide range of diverse problems at MDC and at several government sites. These tools were already installed on all of the computer systems used in this study.

The TETMESH grid generation software was developed by Computational Mechanics Company under contract from USAF Wright Laboratory. TETMESH uses a constrained Delaunay procedure for generation of Euler tetrahedral grids and a surface extrusion method for the viscous layer grid. Cobalt was developed at the USAF Wright Laboratory. The methodology is based on an upwind, cell-centered finite-volume scheme and uses a Spalart-Allmaras one-equation turbulence model. Cobalt can use grids composed of cells of arbitrary type and different cell types are permitted within the same grid.

3

The TETMESH software was distributed by WL/FIMC personnel as a file containing the TETMESH executable and several utility files. The software only runs on Silicon Graphics computer systems and was installed without difficulty. The Cobalt software was distributed as source code with a Makefile appropriate for several computer systems (not including HP). Several minor changes were required to the Makefile to compile and install the software on the MDC HP and government supplied CRAY computer systems.

3. UNSTRUCTURED GRID ASSESSMENT: FLAT PLATE FLOWFIELDS

The extensive availability of test and analytical data for flat plate flow fields makes this an important case for evaluating the accuracy of flow solver algorithms. In addition, the simple nature of the flat plate geometry reduces grid generation and solution run times. These properties enabled us to generate a large number of grids and solutions in a relatively short amount of time. These solutions were used to evaluate the relative accuracy and to identify appropriate grid spacing requirements of each method over a range of flow field conditions.

The viscous layer grid requirements of each flow simulation method vary due to differences in numerical algorithms. Before an equitable comparison of the efficiency and accuracy of each method can be made, grid spacing requirements must be established. These requirements were identified by performing a grid refinement study on turbulent and laminar flat plates at three different run conditions. Three grid spacing parameters were determined to be critical to the accuracy of the flow solution for each method. These are the spacing of the first point normal to the wall, the number of points across the boundary layer, and the surface grid density. The grid spacing requirements for each flow simulation method were determined by sequentially reducing one of the grid spacing parameters and generating a solution. This was continued until a nearly grid independent solution was obtained.

Once adequate grid spacings requirements were identified, a relative assessment of the accuracies of each method was made. Laminar solutions were evaluated to study the diffusion properties of each method in the absence of turbulence model differences. Differences in the turbulence modeling implementation were investigated by comparing turbulent flat plate solutions.

3.1 Grid Generation

A flat plate spanning 30 inches long and 3 inches wide was selected for this study. The solution domain extends 5 inches upstream of the plate leading edge and protrudes 5 inches into the flowfield normal to the plate surface (See Figure 2).

The flow field outside the boundary layer plays a minor role in the flow solution over a flat plate. The grid topology outside the viscous layer, therefore, has little effect on the flat plate solution. For this study, grid generation was simplified by extending the viscous layer grid topology to the outer boundary so that a single grid topology exists throughout the domain (*i.e.* hexahedral, tetrahedral or prismatic). Flat plate hexahedral grids were generated using the MACGS software. Prismatic grids were generated by extruding a surface mesh consisting of triangular faces into prisms. Tetrahedral flat plate grids were generated by subdividing a hexahedral grid into tetrahedra (each hexahedral cell was subdivided into 2 prismatic cells, which were further subdivided into 3 tetrahedra each). A total of 31 flat plate grids were generated including 12 prismatic. 13 hexahedral, and 6 tetrahedral grids. Three measures were selected to describe the grid density. These are spacing of the first point normal to the wall, surface grid density, and number of points across the boundary layer. A summary of the grid sizes, and grid density for each grid is given in Table 1.

5
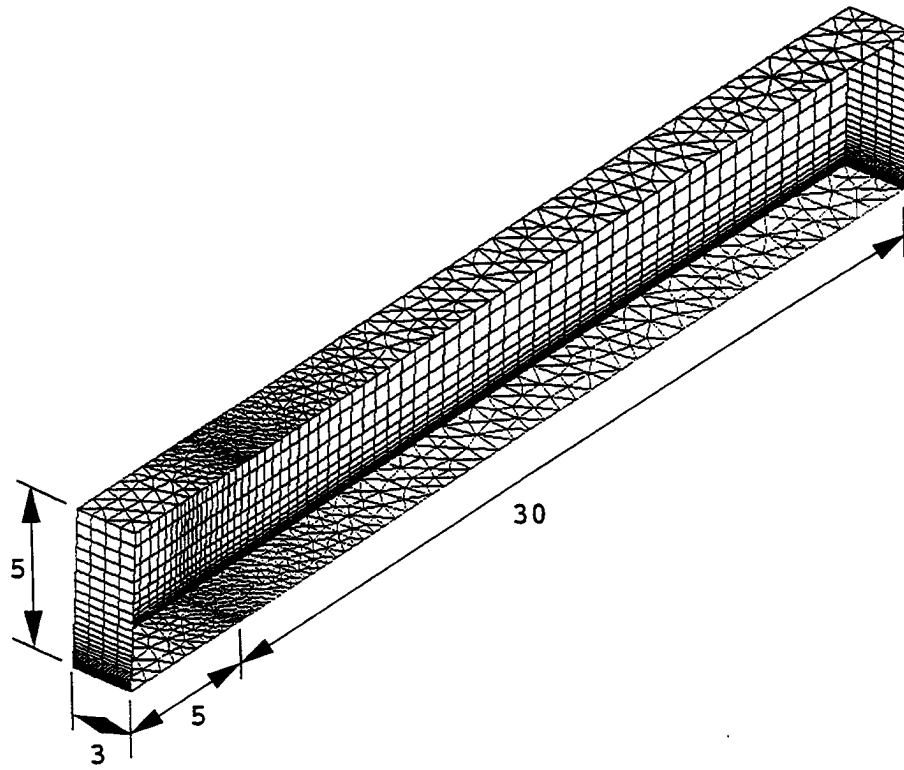
Figure 2. Flat Plate Grid Domain

Table 1. Flat Plate Unstructured Grids

Grid Name	Grid Type	Surface Faces	Normal Points	Number of Points	Number of Cells	Δy at the wall
c-2	Prismatic	2662	29	43,590	77,198	0.0001
c-3	Prismatic	2662	27	42,137	74,536	0.00037
c-4	Prismatic	2662	25	39,231	69,212	0.00084
c-5	Prismatic	2662	22	33,419	58,564	0.0014
c-6	Prismatic	696	29	12,630	20,184	0.0001
c-7	Prismatic	696	27	11,788	18,792	0.00037
c-8	Prismatic	696	25	10,946	17,400	0.00084
c-9	Prismatic	696	22	9,683	15,312	0.0014
c-11	Prismatic	696	59	24,839	40,368	0.0001
c-12	Prismatic	696	39	16,840	27,144	0.005
c-13	Prismatic	696	39	16,840	27,144	0.01
c-14	Prismatic	696	39	16,840	27,144	0.0028
n-2	Hexahedral	118x5	31	18,290	14,040	0.0001
n-3	Hexahedral	118x5	29	17,110	13,104	0.00037
n-4	Hexahedral	118x5	27	15,930	12,168	0.00084
n-5	Hexahedral	118x5	24	14,160	10,764	0.0014

Grid Name	Grid Type	Surface Faces	Normal Points	Number of Points	Number of Cells	Δy at the wall
n-6	Hexahedral	69x5	31	10,695	8,160	0.0001
n-7	Hexahedral	69x5	29	10,005	7,616	0.00037
n-8	Hexahedral	69x5	27	9,315	7,072	0.00084
n-9	Hexahedral	69x5	24	8,280	6,256	0.0014
n-10	Hexahedral	69x5	59	20,355	15,776	0.00085
n-11	Hexahedral	69x5	59	20,355	15,776	0.0001
n-12	Hexahedral	69x5	41	14,145	10,880	0.005
n-13	Hexahedral	69x5	41	14,145	10,880	0.01
n-14	Hexahedral	59x5	41	14,145	10,880	0.0028
u-1	Tetrahedral	192	15	2205	8064	.0014
u-2	Tetrahedral	192	17	2499	9216	.0004
u-3	Tetrahedral	192	13	1911	6912	.01
u-4	Tetrahedral	192	12	1764	6336	.03
u-5	Tetrahedral	192	12	1764	6336	.02
u-6	Tetrahedral	192	13	1911	6912	.0056

3.2 Flow Solutions

Several solutions were computed on the grids listed in Table 1 using the Cobalt, NASTD, and USM3D flow solvers. These methods were evaluated across a range of flow conditions. Laminar flat plate solutions were generated at a Mach number 0.1 and Reynolds number of 1.77 million at the plate trailing edge. This condition provided the ability to evaluate the diffusion properties of each of the method in the absence of turbulent modeling effects. The second run condition of Mach 0.1 and Reynolds number of 1.77 million was selected to provide an assessment of a turbulent flowfield at a low to moderate Reynolds number. In addition, the relatively low Mach number of 0.1 provided an almost incompressible flow field. Compressibility effects were evaluated by computing turbulent solutions at a Mach number of 0.7 and Reynolds number of 12 million at the plate trailing edge.

A total of 57 flat plate solutions were computed consisting of 23 Cobalt, 24 NASTD, and 10 USM3D solutions. A summary of the run conditions for each solution is shown in Table 2. A heavy line separates solutions from each run condition and each flow solver. In addition to providing relative assessments of accuracy, each solution was used to evaluate one or more grid measures as part of the grid refinement study. The grid measures that were assessed with a particular solution are indicated in the shaded columns with a + for spacing of the first grid point normal to the surface, b for the number of boundary layer points, and s for the surface grid density.

7

Table 2. Flat Plate Run Matrix

Flow Solver	Mach	$Re_x 10^{-6}$	Turb Model	y^+	bndry layer points	Surface Faces	Grid	Iterations $\times 10^{-3}$	CFL Number	CPU Time sec/iter*cell $\times 10^6$	Comments	Grid Measure		
Cobalt	0.1	1.77	Laminar	0.39	16	696	c-7	250	.7			+	b	
Cobalt	0.1	1.77	Laminar	0.91	14	696	c-8	260	.7		did not use	+		
Cobalt	0.1	1.77	Laminar	1.49	11	696	c-9	306	.7			+		
Cobalt	0.1	1.77	Laminar	0.16	33	696	c-11		.7		not converged		b	
Cobalt	0.1	1.77	Laminar	6.25	12	696	c-12		.7		not converged	+		
Cobalt	0.1	1.77	Laminar	12.22	8	696	c-13	190	.7			+		
Cobalt	0.1	1.77	Spalart	0.84		2662	c-3	38	.7		did not use			
Cobalt	0.1	1.77	Spalart	1.87	13	2662	c-4	46	.7		did not use			s
Cobalt	0.1	1.77	Spalart	0.16	22	696	c-6	182	.7			+	b	
Cobalt	0.1	1.77	Spalart	0.58	15	696	c-7	165	.7	290		+		
Cobalt	0.1	1.77	Spalart	1.32	13	696	c-8	192	.7			+		s
Cobalt	0.1	1.77	Spalart	2.24	9	696	c-9	166	.7			+		
Cobalt	0.1	1.77	Spalart	0.24	40	696	c-11		.7		not converged		b	
Cobalt	0.1	1.77	Spalart	4.48	18	696	c-14	110	.7			+		
Cobalt	0.7	12	Spalart	0.87	17	2662	c-2	57	.7		did not use			♦
Cobalt	0.7	12	Spalart	3.27	15	2662	c-3	57	.7		did not use			♦
Cobalt	0.7	12	Spalart	8.54	12	2662	c-4	57	.7		did not use			♦
Cobalt	0.7	12	Spalart	13.81	9	2662	c-5	60	.7		did not use			♦
Cobalt	0.7	12	Spalart	0.8	17	696	c-6	40	.7	290		+	b	s
Cobalt	0.7	12	Spalart	2.99	15	696	c-7	52	.7			+		s
Cobalt	0.7	12	Spalart	7.66	12	696	c-8	50	.7			+		s
Cobalt	0.7	12	Spalart	12.76	9	696	c-9	53	.7			+		s
Cobalt	0.7	12	Spalart	0.8	40	696	c-11	62	.7				b	
NASTD	0.1	1.77	Laminar	0.1	18	272	n-6	65	5			+	b	
NASTD	0.1	1.77	Laminar	0.4	16	272	n-7	54	5		did not use	+		
NASTD	0.1	1.77	Laminar	0.85	14	272	n-8	46	5		did not use	+		
NASTD	0.1	1.77	Laminar	1.45	11	272	n-9	31	5			+		
NASTD	0.1	1.77	Laminar		33	272	n-11	15	5				b	
NASTD	0.1	1.77	Laminar	5.75	12	272	n-12	20	5			+		
NASTD	0.1	1.77	Laminar	10.22	8	272	n-13	21	5			+		
NASTD	0.1	1.77	Spalart	1.99	13	468	n-4	16	5					s
NASTD	0.1	1.77	Spalart	3.61	9	468	n-5	27	5		did not use			s
NASTD	0.1	1.77	Spalart	0.23	22	272	n-6	37	5	925		+	b	
NASTD	0.1	1.77	Spalart	0.86	15	272	n-7	21	5			+		
NASTD	0.1	1.77	Spalart	1.98	13	272	n-8	24	5			+		s

Flow Solver	Mach	Rex10⁻⁶	Turb Model	y+	bndry layer points	Surface Faces	Grid	Iterations x10³	CFL Number	CPU Time sec/ iter*cell x10⁶	Comments	Grid Measure		
NASTD	0.1	1.77	Spalart	4.0	9	272	n-9	7	5			+		s
NASTD	0.1	1.77	Spalart	0.23	40	272	n-11	12	5				b	
NASTD	0.1	1.77	Spalart	8.0	18	272	n-14	20	5			+		
NASTD	0.7	12	Spalart	1.26	17	468	n-2	6	5					s
NASTD	0.7	12	Spalart	4.86	15	468	n-3	4	5		did not use			s
NASTD	0.7	12	Spalart	12.43	12	468	n-4	3	5		did not use			s
NASTD	0.7	12	Spalart	23.63	9	468	n-5	4	5	925	did not use			s
NASTD	0.7	12	Spalart	1.26	17	272	n-6	20	5			+	b	s
NASTD	0.7	12	Spalart	4.86	15	272	n-7	11	5			+		s
NASTD	0.7	12	Spalart	12.42	12	272	n-8	5	5			+		s
NASTD	0.7	12	Spalart	23.62	9	272	n-9	9	5			+		s
NASTD	0.7	12	Spalart	1.26	30	272	n-11	3	5				b	
USM3D	0.1	1.77	Laminar	1.5		192	u-1		200		did not use	+		
USM3D	0.1	1.77	Laminar	6.25	5	192	u-3	20	200			+		
USM3D	0.1	1.77	Laminar	12.22	6	192	u-6	6	200			+		
USM3D	0.1	1.77	Spalart/wf	1.1	13	192	u-2	12	200			+		
USM3D	0.1	1.77	Spalart/wf	25.4	8	192	u-3	6	200			+		
USM3D	0.1	1.77	Spalart/wf	73.8	5	192	u-4	6	200	1750		+		
USM3D	0.1	1.77	Spalart/wf	49.0	5	192	u-5	5	200			+		
USM3D	0.7	12	Spalart/wf	18.2	8	192	u-1	10	200			+		
USM3D	0.7	12	Spalart/wf	122.4	4	192	u-3	8	200	1750		+		
USM3D	0.7	12	Spalart/wf	68.9	5	192	u-6	8	200			+		

An attempt was made to minimize the differences between the flow solver algorithms by selecting similar algorithm features when available. For instance, all solutions were generated using a second-order accurate (in computational space) algorithm and the Spalart/Allmaras turbulence model (for turbulent computations). Even with these choices several differences remain between the flow solver algorithms. One such difference is in the flux computations. Both NASTD and USM3D use Roe's approximate Reimann solver for these computations while Cobalt uses the approximate Reimann solution method due to Collela in combination with the iterative method of Gottlieb and Groth. There are also differences in the viscous term computations between the methods. For turbulent flow fields USM3D uses a wall function to model the near wall region. The time integration schemes of each method are very different. Cobalt uses an explicit Runge-Kutta algorithm while NASTD uses an approximate factorization implicit method and USM3D uses a point Jacobi implicit method. The spatial discretization is also substantially different in the three codes with Cobalt and USM3D using cell centered methods and NASTD using a vertex based scheme.

Solution converge of all solutions was determined by monitoring the integrated drag and skin friction. Convergence data for each solution is provided in Appendices A,B, and C.

3.3 Laminar Flat Plate Results

Laminar flat plate solutions were generated at a Mach number 0.1 and Reynolds number of 1.77 million. This condition provided the ability to evaluate the diffusion properties of each of the method in the absence of turbulence modeling effects. Flow solution accuracy was evaluated by comparing the predicted velocity profile results with the well known theoretical profile of Blasius. The skin friction was compared with the theoretical skin friction for laminar flow of $C_f = 1.328 \, (Re_x)^{-0.5}$

3.3.1 <u>Cobalt Results</u>

Cobalt Laminar flat plate solutions were run on grids c-7, c-8, c-9, c-11, c-12, and c-13. The solutions on grids c-11 and c-12 did not fully converge and so the results are not shown in this report. All of these grids contain the same number of surface points. Attempts to run on grids c-2 through c-5 with larger surface sizes required an excessively large amount of time to converge. After several weeks of running these solutions were abandoned. The explicit time integration scheme used by Cobalt dictated a relatively low CFL number of 0.7. As a result the Cobalt laminar flat plate solutions were found to converge very slowly requiring upwards of 300,000 iterations.

The effect of wall grid spacing on solution accuracy is illustrated by the solutions on grids c-7, c-9 and c-13. These solutions provide wall grid spacings of $y^+ = 0.39$, 1.5 and 12 respectively. The Cobalt predicted velocity profile across the boundary layer is compared with the Blasius profile at four plate locations in Figures 3 through 5. The profiles from grids c-7, and c-9 are similar. The profiles from grids c-9 and c-13 differ primarily in the upstream portion of the plate. The predicted skin friction from these solutions is compared with the theoretical value in Figure 6. The wall grid spacing was found to have little effect on the predicted skin friction for the two sizes that were run. The solution near the leading edge of the plate is slightly better on grid c-9 (y^+ of 1.5) compared to grid c-13 (y^+ of 12). Clearly additional data is needed to determine the required grid spacing for these run conditions. The solution on grid c-12 would have provided an intermediate data point for the wall grid spacing. Unfortunately this solution did not fully converge. From the data that we do have we can conclude that the required wall grid spacing for laminar solutions is somewhere between 1.5 and 12.

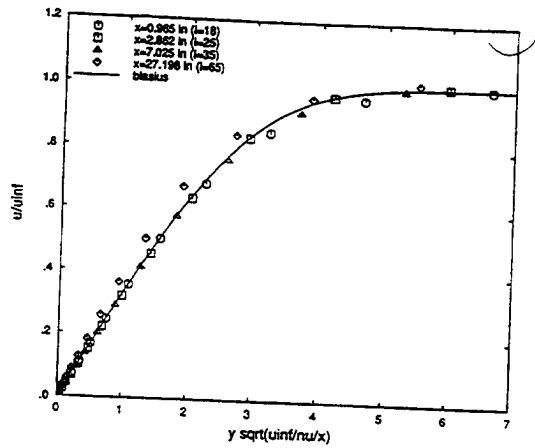Figure 3. Velocity profile, Cobalt laminar solution, Mach 0.1, Re=1.77x10^6, Grid c-7.

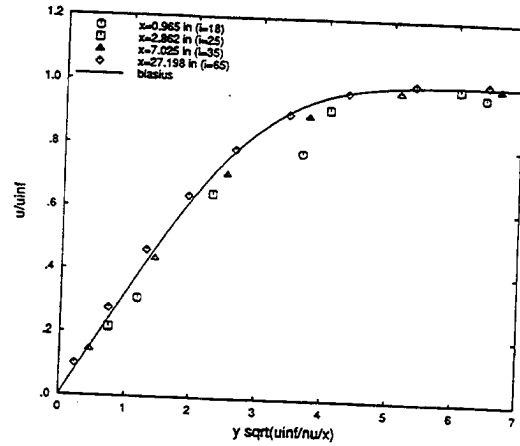

Figure 5. Velocity profile, Cobalt laminar solution, Mach 0.1, Re=1.77x10^6, Grid c-13.
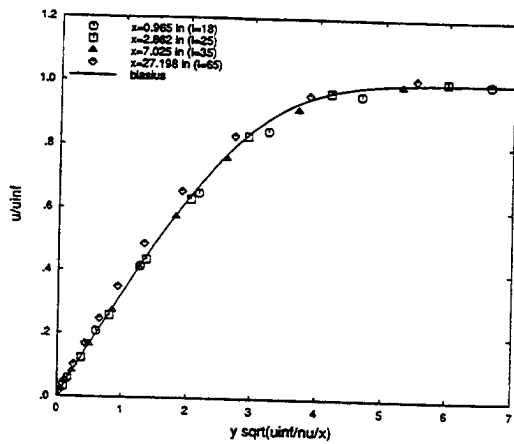

Figure 4. Velocity profile, Cobalt laminar solution, Mach 0.1, Re=1.77x10^6, Grid c-9.

11
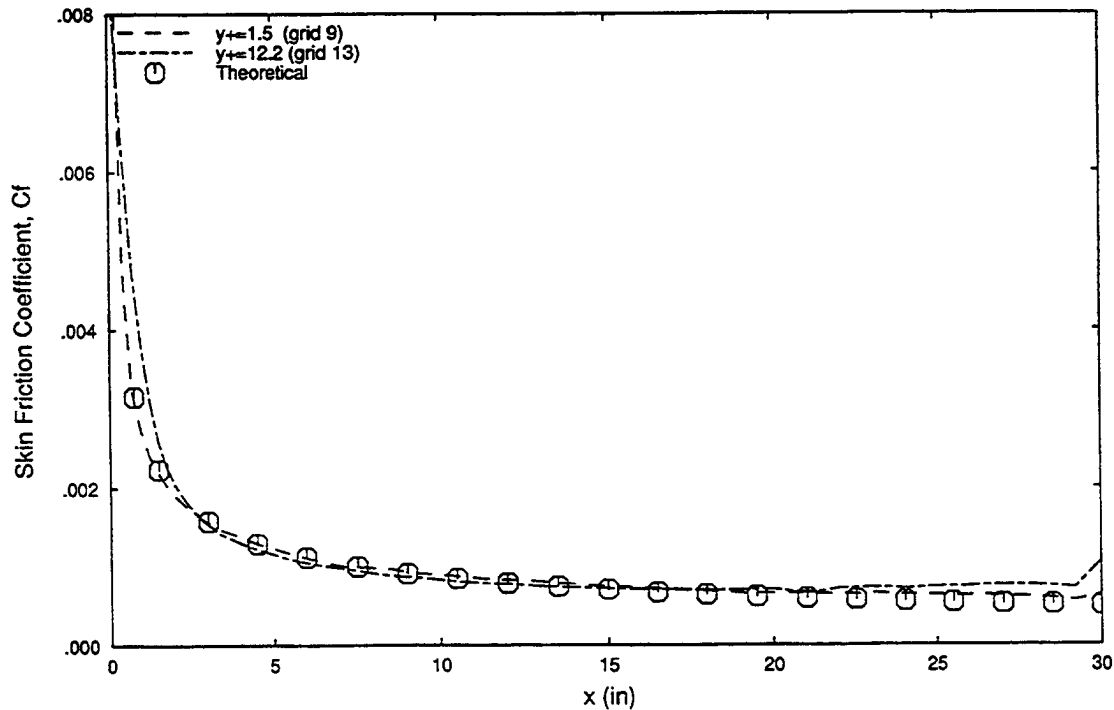
Figure 6. Effect of wall grid spacing on skin friction coefficient,
Cobalt laminar solutions, Mach 0.1, Re=1.77 million

3.3.2 NASTD Results

NASTD Laminar flat plate solutions were run on grids n-6, n-7, n-8, n-9, n-11, n-12, and n-13. The solutions on grids n-7 and n-8 were virtually identical to the solution on grid n-6 and so the results are not shown. Grids n-9, n-12 and n-13 provided a comparison of solutions with wall grid spacings of y^+ = 1.5, 6, and 10 and grids n-6 and n-11 provide a comparison of two different distributions of points across the boundary layer. All of these grids have the same surface grid size. The time integration was performed with a factored implicit scheme permitting CFL numbers of approximately 5.0. The NASTD laminar flat plate solutions were found to converge slower than the NASTD turbulent cases requiring between 30,000 and 80,000 iterations.

The effect of the wall grid spacing on solution accuracy is demonstrated by the solutions on grids n-9, n-12 and n-13. The NASTD predicted velocity profile on these grids at four plate locations is compared with the Blasius profile in Figures 8, 10, and 11. Predicted skin friction is compared with the theoretical value in Figure 12. Once the boundary layer was developed, the wall grid spacing was found to have little effect on the predicted skin friction for the three sizes that were run. The solution near the leading edge of the plate, however, was predicted better on the grid with a y^+ of 1.5 compared to the other two grids. The predicted velocity profiles also agree very well with the theoretical Blasius solution once the boundary layer was developed.

The effect of the number of points across the boundary layer was investigated by comparing the solutions on grids n-6 and n-11. These grids have 18 and 33 points across the viscous layer. The predicted velocity profiles using these grids are shown in Figures 7 and 9, and the predicted skin friction is shown in Figure 13. The distribution of points was found to have little effect on the skin friction and velocity profile predictions.

12

Figure 7. Velocity profile, NASTD laminar solution, Mach 0.1, Re=1.77x10^6, Grid n-6.

Figure 8. Velocity profile, NASTD laminar solution, Mach 0.1, Re=1.77x10^6, Grid n-9.

Figure 9. Velocity profile, NASTD laminar solution, Mach 0.1,Re=1.77x10^6, Grid n-11.

Figure 10. Velocity profile, NASTD laminar solution, Mach 0.1, Re=1.77x10^6, Grid n-12.

Figure 11. Velocity profile, NASTD laminar solution, Mach 0.1, Re=1.77x10^6,Grid n-13

13

Figure 12. Effect of wall grid spacing on skin friction coefficient, NASTD laminar solutions, Mach 0.1, Re=1.77 million.

Figure 13. Effect of number of points in boundary layer on skin friction coefficient, NASTD laminar solutions, Mach 0.1, Re=1.77 million.

14

3.3.3 USM3D Results

USM3D laminar flat plate solutions were run on grids u-3 and u-6 providing a comparison of solutions with wall grid spacings of $y^+ = 6.25$ and 12.22. Both solutions have the same surface grid size. The time integration was performed with a point Jacobi implicit scheme permitting CFL numbers of approximately 200. The solutions on grid u-3 and u-6 required 20,000 and 12,000 iterations to converge.

USM3D predicted velocity profiles using these grids are shown in Figures 14 and 15. The skin friction predictions are compared with the theoretical value in Figure 16. Once the boundary layer is developed, the wall grid spacing has little effect on the predicted skin friction for the two wall spacing sizes that were run. The solution near the leading edge of the plate, however, is predicted better on the grid with tighter wall spacing. The predicted velocity profiles agree very well with the theoretical Blasius solution once the boundary layer is developed. The profiles near the leading edge do not agree well with the Blasius solution, probably due to poor grid resolution.
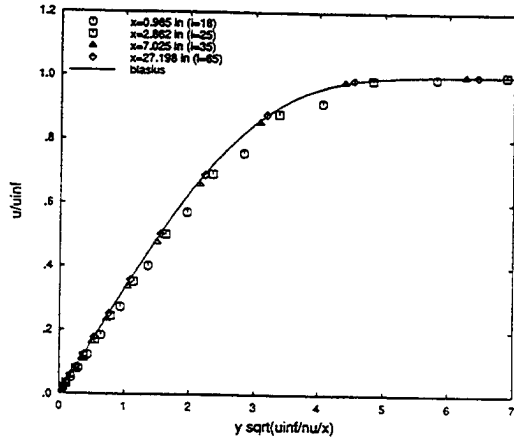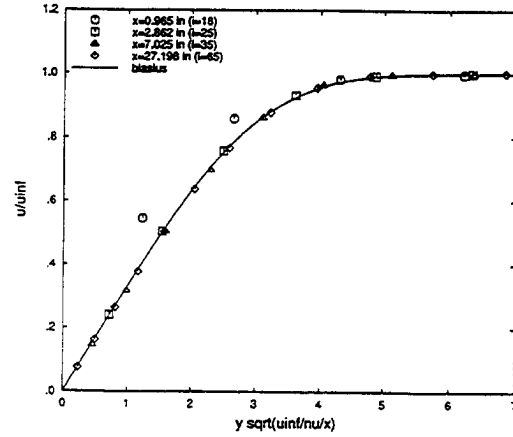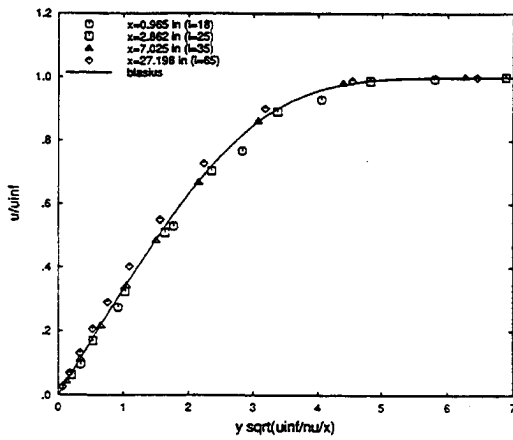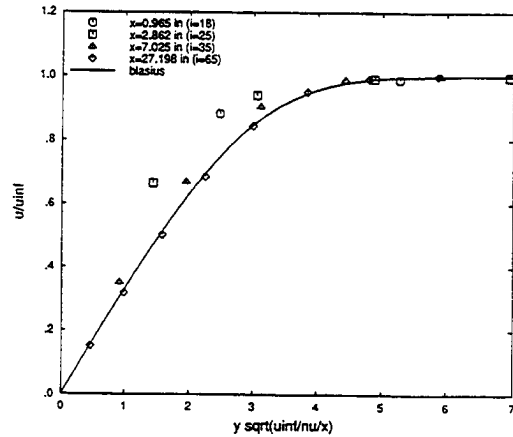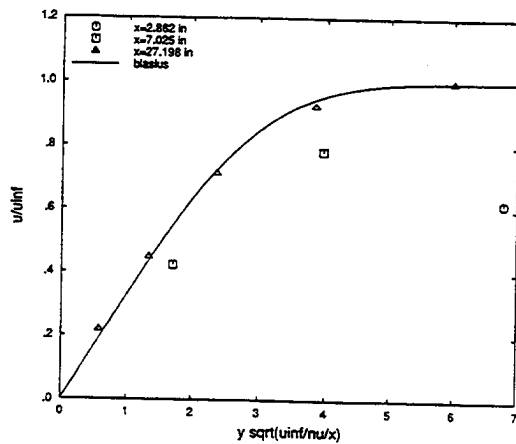

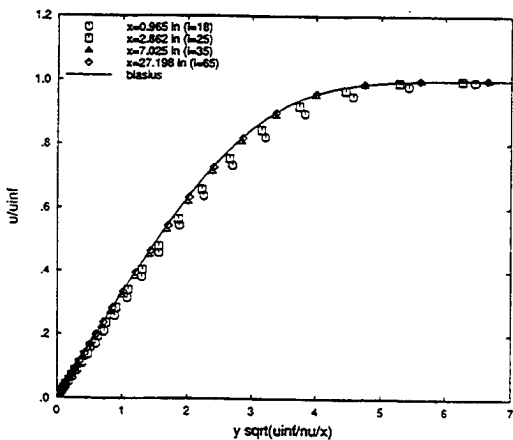Figure 14. Velocity profile, USM3D laminar solution, Mach 0.1, Re=1.77x10⁶, Grid u-3.
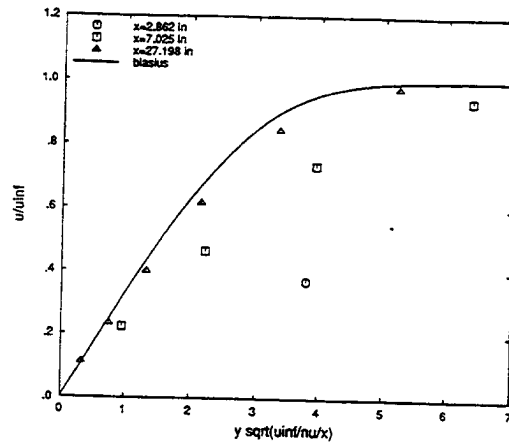
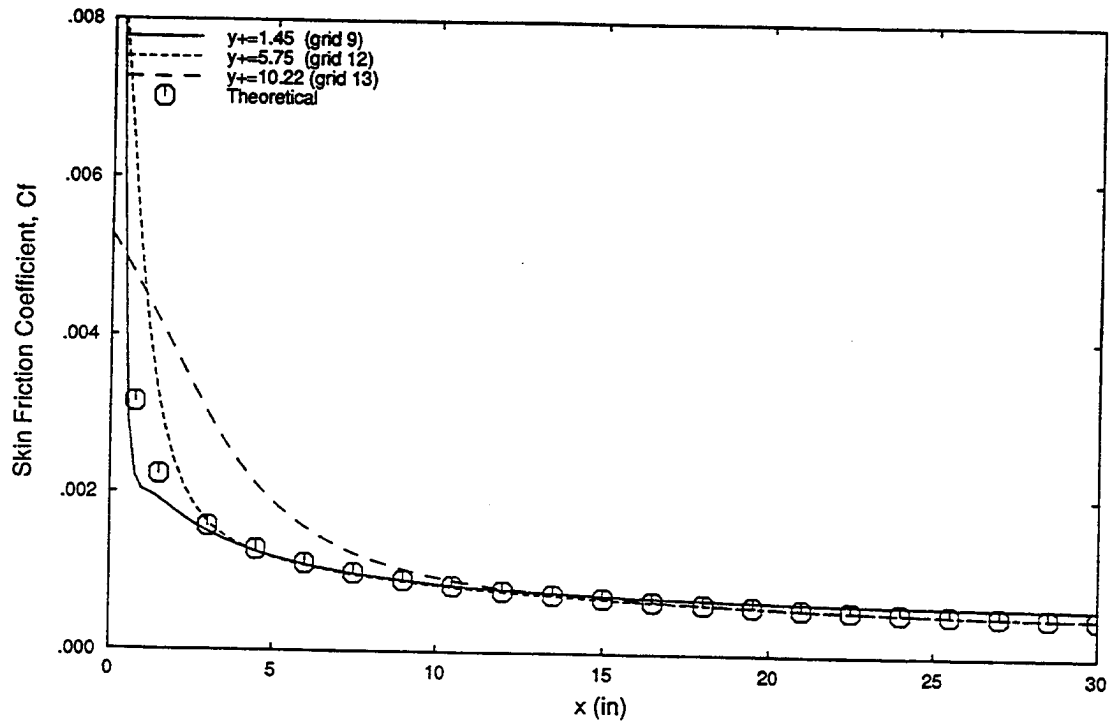Figure 15. Velocity profile, USM3D laminar solution, Mach 0.1, Re=1.77x10⁶, Grid u-6.

15
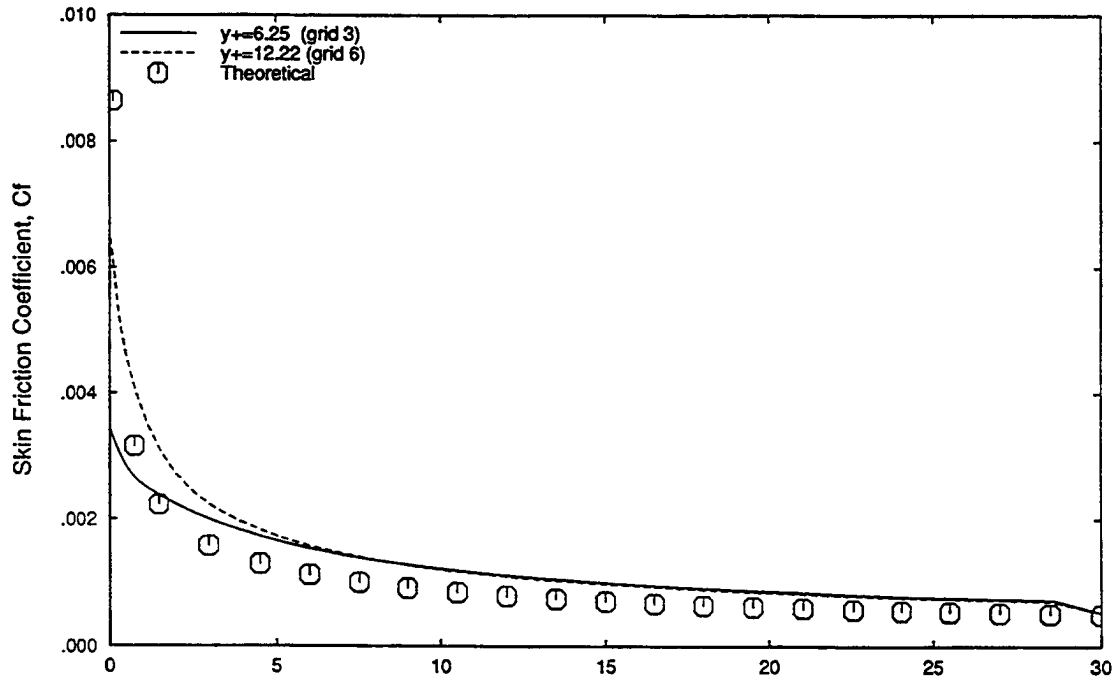
Figure 16. Effect of wall grid spacing on skin friction coefficient,
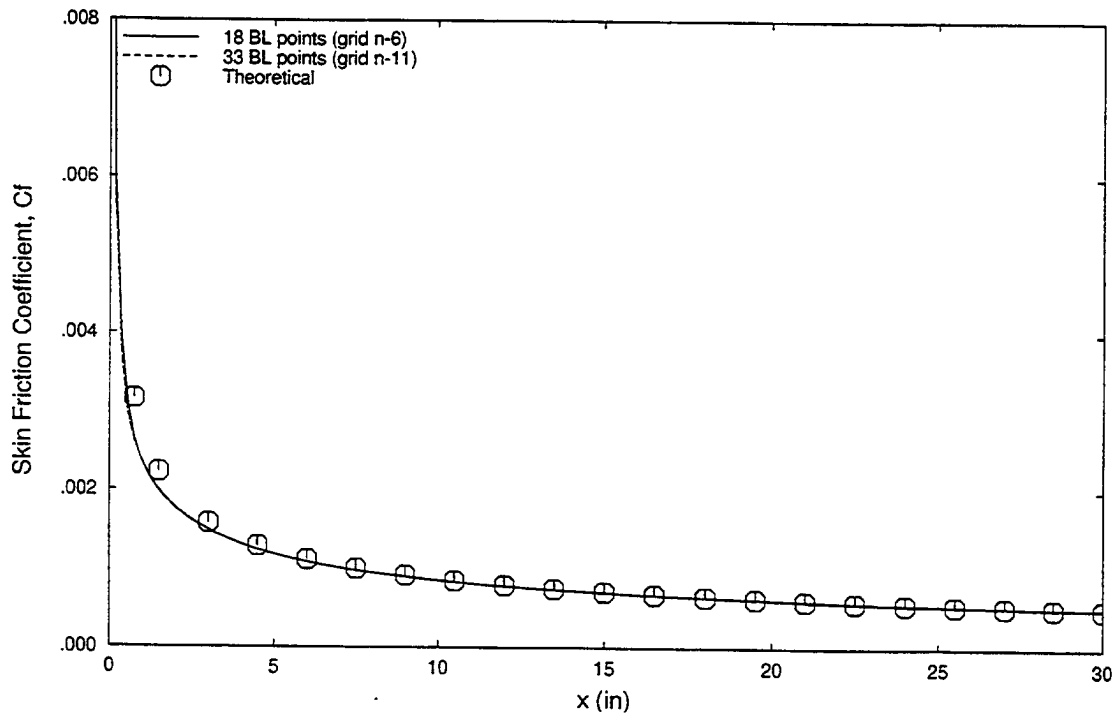USM3D laminar solutions, Mach 0.1, Re=1.77 million.

3.4 Turbulent Flat Plate Results

Turbulent flat plate solutions were computed at two run conditions with all three of the flow solution methods. Nearly incompressible solutions were computed at a run condition of Mach 0.1, Reynolds number of 1.77 million while the effects of compressibility were investigated at run conditions of Mach 0.7 and Reynolds number of 12 million. All of the solutions were computed using the Spalart/Allmaras turbulence model. Flow solution accuracy was evaluated by comparing the predicted velocity profile results with the theoretical law of the wall velocity profile. The skin friction was compared with the theoretical skin friction for fully turbulent flow of $C_f = 0.0583$ $(Re_x)^{-1/5}$ which is based on Prandtl's power law assumption. For the high Reynolds number case, the skin friction is also compared against the relationship $C_f = 0.455/(\ln^2(0.06\ Re_x))$ which is taken from Reference (3).

3.4.1 Cobalt Results

After running the Cobalt flat plate solutions to convergence, a change in the Cobalt implementation of the Spalart/Allmaras turbulence model was made in mid October 1996. Rather than rerun all of the turbulent Cobalt solutions from scratch, these solutions were restarted from their previous states. The number of iterations shown in Table 2 includes only the iterations required to reach convergence before the software change. The software change resulted in a slight change in the converged value of integrated drag as shown in the drag convergence plots in Appendix A.

Turbulent flat plate solutions at the first run condition of Mach 0.1 were generated on

16

grids u-1, u-2, c-6, c-7, c-8, c-9, c-11, and c-14. Solutions on grids c-3 and c-4 were also run but were not restarted after the turbulence model modification was made to Cobalt. The solution on grid c-11 would not converge and was discontinued after 163,000 iterations. The reason for this lack of convergence is not known although it may be grid related since the laminar solution on this grid also failed to converge. These solutions converged relatively slowly requiring approximately 150,000 iterations to reach a converged solution.

The solutions on grids c-7, c-8, c-9, and c-14 have wall grid spacings of y^+=0.58, y^+=1.32, y^+=2.24, and y^+=4.48. Predicted velocity profiles across the boundary layer at four plate locations are compared with the law of the wall in Figures 17 through 21. The predicted skin friction from these solutions is compared with the theoretical value in Figure 22. The skin friction changes as the wall grid spacing is refined until a spacing of y^+=1.32 is reached. The predicted skin friction and velocity profiles at wall spacings of y^+=0.58 and 1.32 are nearly identical. We were unable to determine the effect of grid density across the boundary layer due to lack of convergence of the solution on grid c-11.

The effect of grid cell shape on solution accuracy was evaluated by comparing Cobalt solutions on prismatic cell grids c-7 and c-9 with solutions generated on tetrahedral cell grids u-2 and u-1. The wall grid spacing for grids c-7 and u-2 are 0.00037 and 0.0004 which results in a y^+ of approximately 0.6 at these run conditions. The wall grid spacing for grids c-9 and u-2 is 0.0014 resulting in a y^+ of approximately 2.24. The predicted skin friction for these solutions is compared with the theoretical value in Figure 23. The solutions on grids c-9 and u-1 are nearly identical. However, the solution on tetrahedral grid u-2 is closer to the theoretical value than the solution on prismatic grid c-7. This indicates that cell shape does influence solution accuracy in some instances.

Figure 17. Velocity profile, Cobalt solution, Mach 0.1, Re=1.77 million, Grid c-6.

Figure 18. Velocity profile, Cobalt solution, Mach 0.1, Re=1.77 million, Grid c-7.

17

Figure 19. Velocity profile, Cobalt solution, Mach 0.1, Re=1.77 million, Grid c-8.

Figure 21. Velocity profile, Cobalt solution, Mach 0.1, Re=1.77 million, Grid c-14.

Figure 20. Velocity profile, Cobalt solution, Mach 0.1, Re=1.77 million, Grid c-9.

18
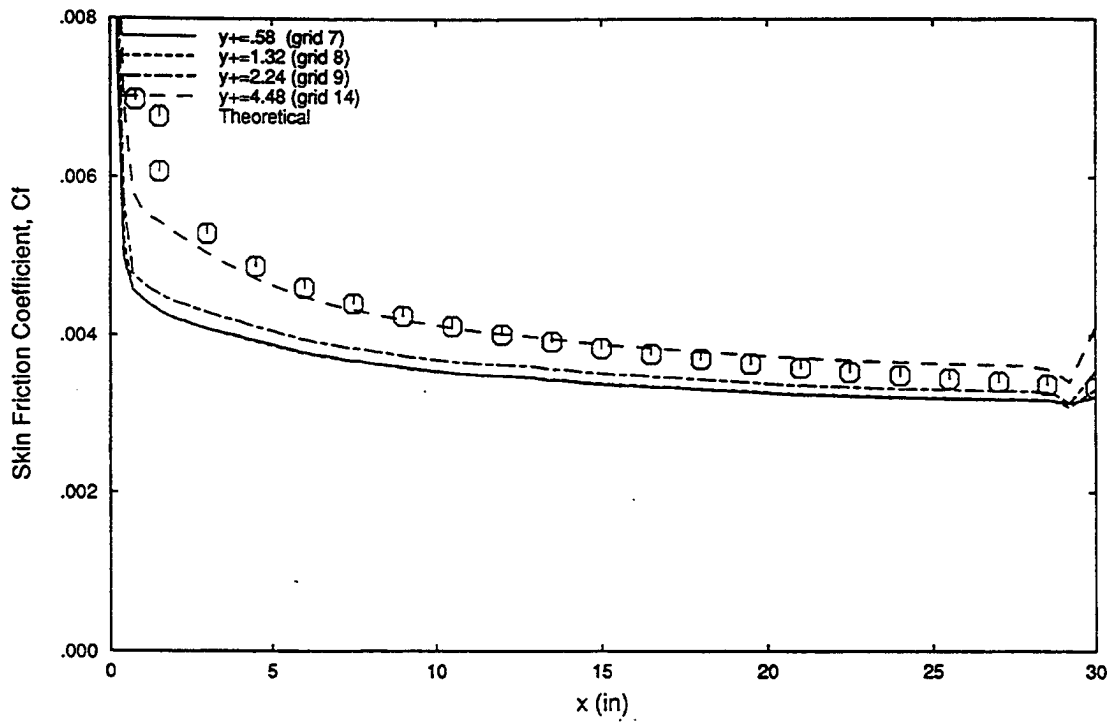
Figure 22. Effect of wall grid spacing on predicted skin friction coefficient,Cobalt turbulent solutions, Mach 0.1, Re=1.77 million
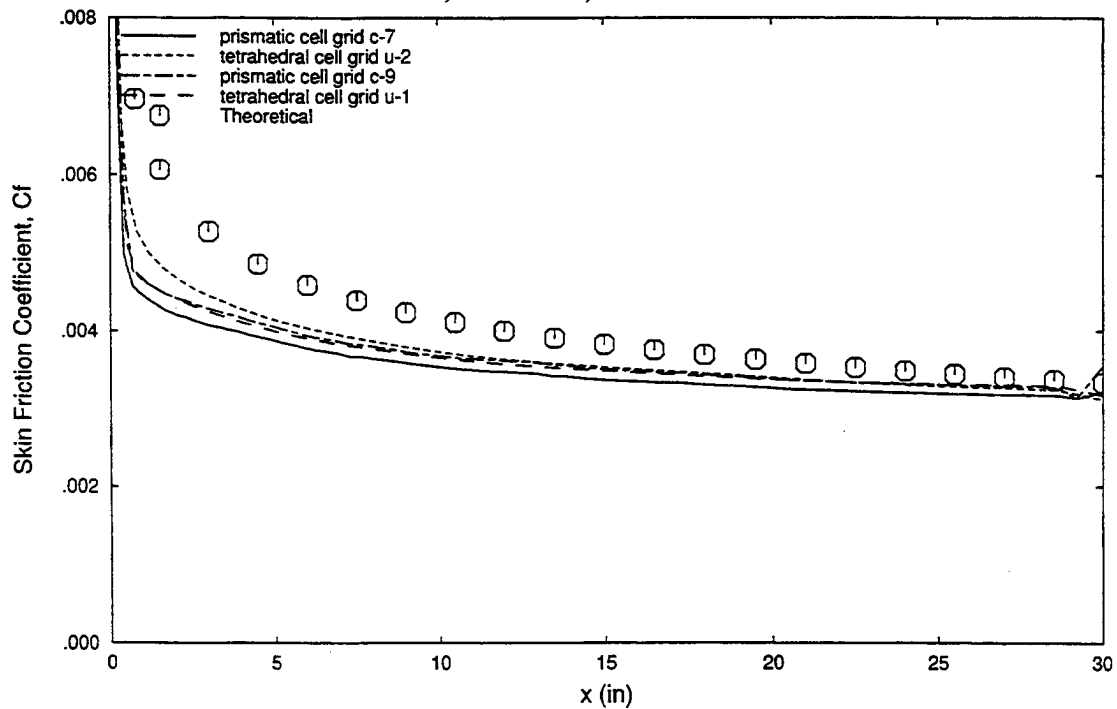
Figure 23. Effect of cell shape on predicted skin friction coefficient,Cobalt turbulent solutions, Mach 0.1, Re=1.77 million

Cobalt turbulent flat plate solutions were run at a second run condition of Mach 0.7, and Reynolds number of 12 million. At these run conditions, solutions were generated on grids u-2, c-6, c-7, c-8, c-9, and c-11. Solutions on grids c-3, c-4, and c-5 were also run but were not restarted after the turbulence model modification was made to Cobalt. These solutions converged much faster than the low Reynolds number solutions requiring approximately 60,000 iterations.

The solutions on grids c-6, c-7, c-8, and c-9 have wall grid spacings of y^+=0.8, y^+=3.0, y^+=7.7, and y^+=12.8. These solutions were used to evaluate the effect of wall grid spacing on solution accuracy. Velocity profiles across the viscous layer from the Cobalt solutions are shown in Figures 24-27. The predicted skin friction from these solutions is compared with the theoretical value in Figure 29. The solutions do not appear to change at wall grid spacings below y^+=3.0.

The solutions on grids c-6 and c-11 were used to evaluate the effect of viscous layer grid resolution on solution accuracy. These grids contain 17 and 40 points across the viscous layer ($y^+ < 800$) respectively. Predicted velocity profile and skin friction from the two solutions is shown in Figures 24,28 and 30. Comparison of the skin friction and velocity profiles from the two solutions indicates that adequate viscous layer grid resolution is achieved with 17 grid points.

The effect of cell shape on solution accuracy was evaluated by comparing the solutions on grids c-7 and u-2. These grids have a wall spacing of .0004 which results in a y^+ of approximately 3.0 at these run conditions. The predicted skin friction for these two solutions is compared with the theoretical value in Figure 31. Once again the cell shape does not have a large influence on the solution accuracy.
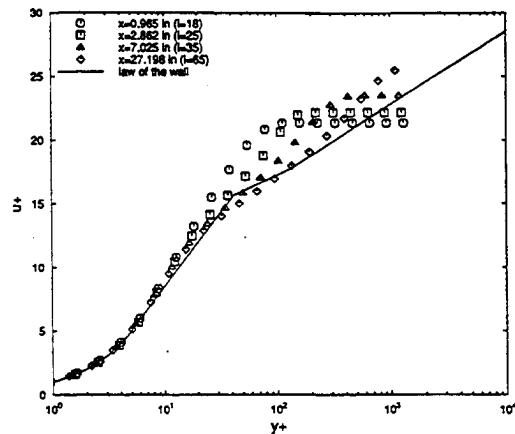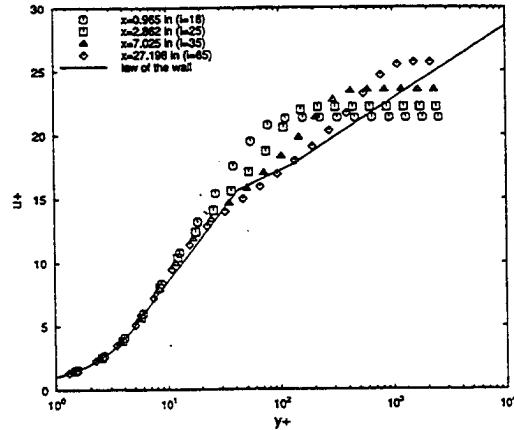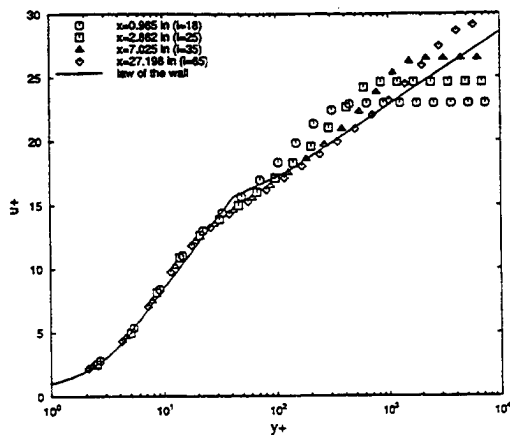
Figure 24. Velocity profile, Cobalt solution, Mach 0.7, Re=12 million, Grid c-6.

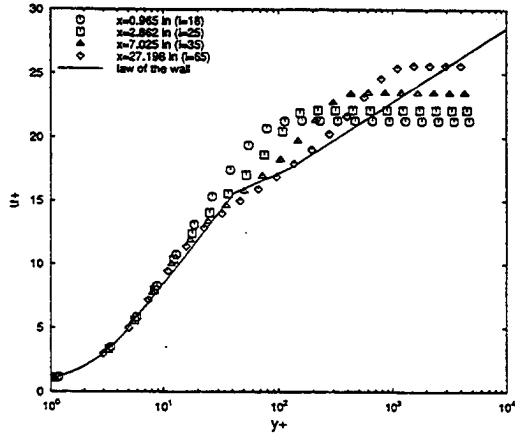Figure 25. Velocity profile, Cobalt solution, Mach 0.7, Re=12 million, Grid c-7.

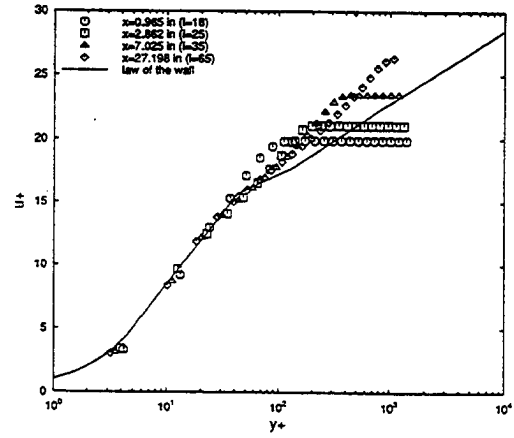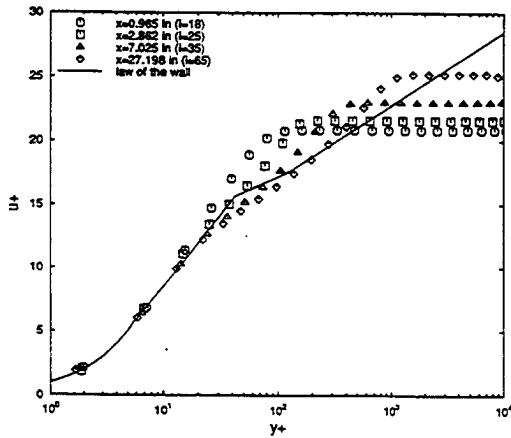Figure 26. Velocity profile, Cobalt solution, Mach 0.7, Re=12 million, Grid c-8.
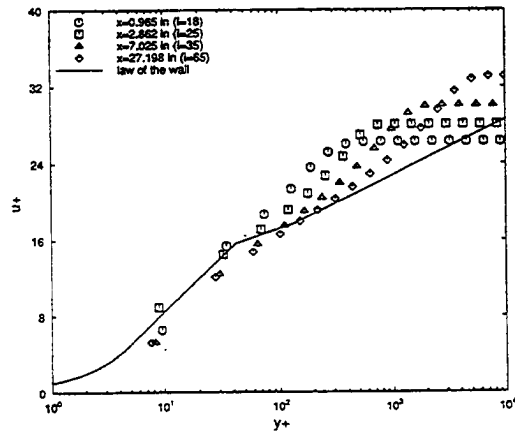
Figure 27. Velocity profile, Cobalt solution, Mach 0.7, Re=12 million, Grid c-9.
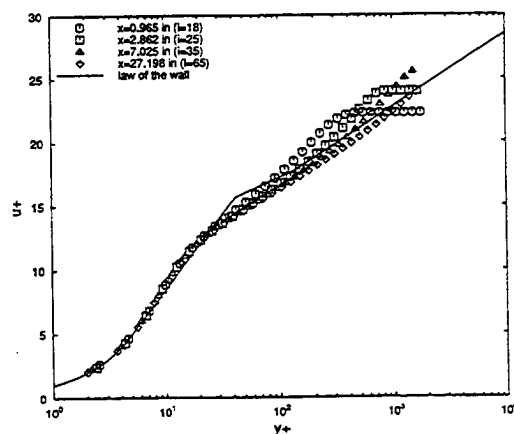
Figure 28. Velocity profile, Cobalt solution, Mach 0.7, Re=12 million, Grid c-11.
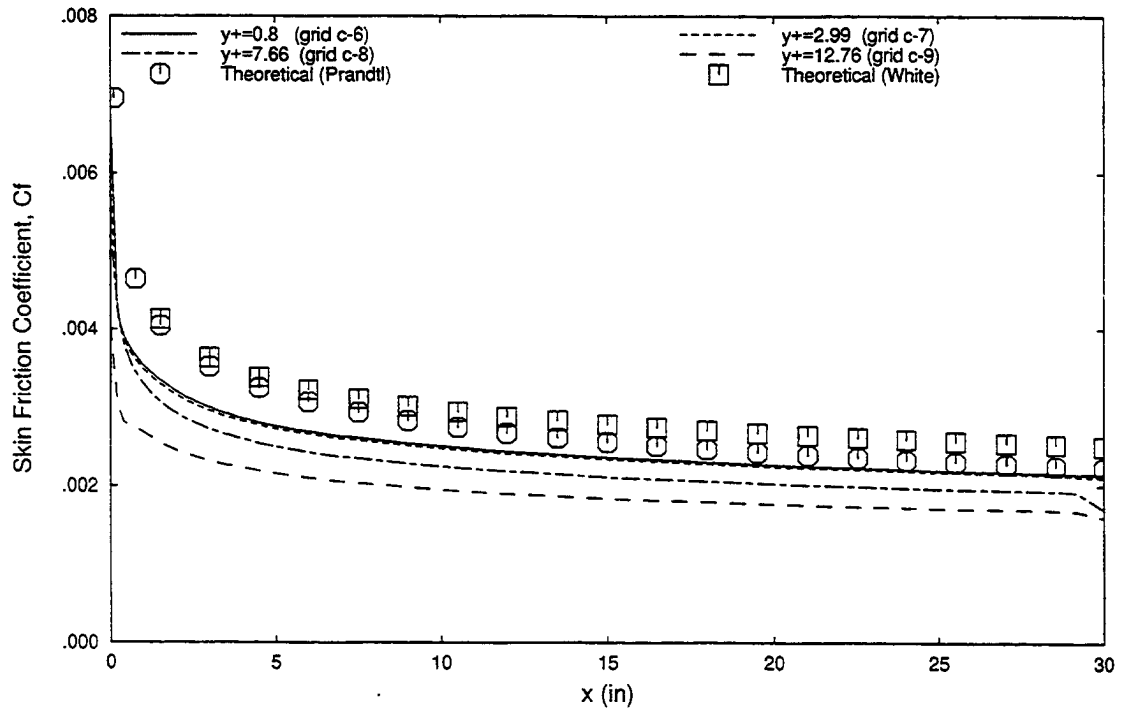
Figure 29. Effect of wall grid spacing on predicted skin friction coefficient, Cobalt turbulent solutions, Mach 0.7, Re=12 million.
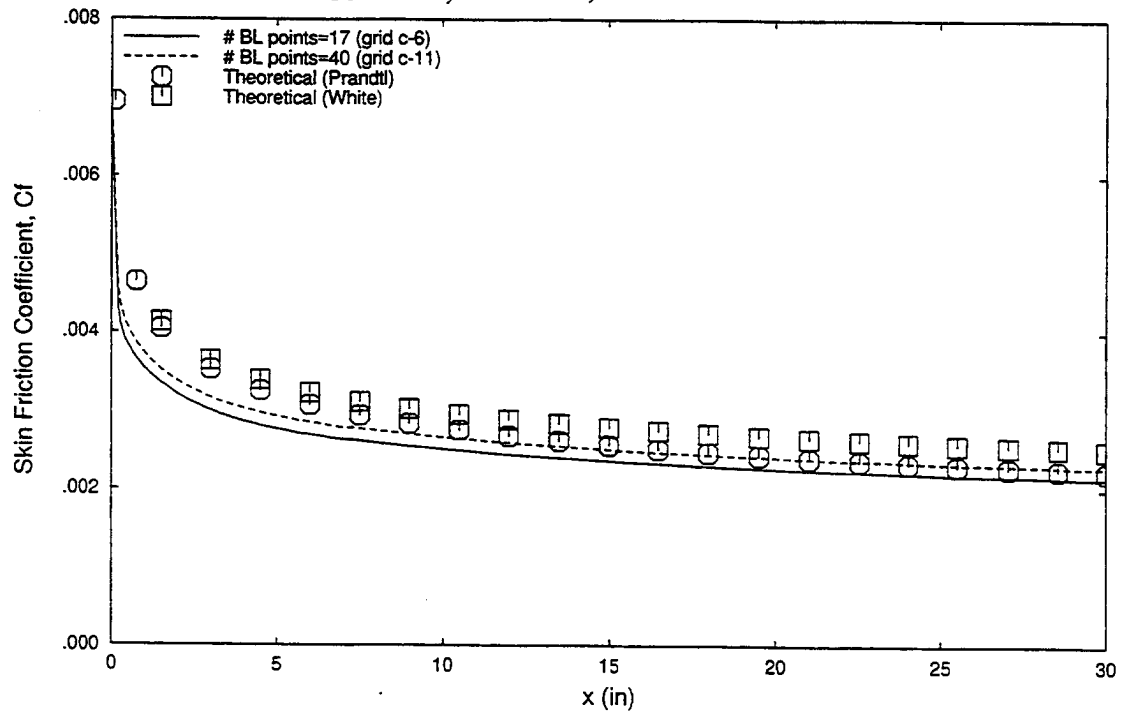
Figure 30. Effect of number of boundary layer points on predicted skin friction coefficient, Cobalt turbulent solutions, Mach 0.7, Re=12 million.

Figure 31. Effect of cell shape on predicted skin friction coefficient, Cobalt turbulent solutions, Mach 0.7, Re=12 million.

3.4.2 NASTD Results

NASTD turbulent flat plate solutions were generated at the first run condition of Mach 0.1, Reynolds number of 1.77 million on grids n-4, n-6, n-7, n-8, n-9, n-11, and n-14. These solutions were run at a CFL number of 5.0 and required between 10,000 and 40,000 iterations to reach convergence.

The effect of wall grid spacing on solution accuracy was evaluated by computing solutions on grids n-7, n-8, n-9, and n-14. At this run condition these grids provide wall grid spacings of $y^+=0.9$, $y^+=2.0$, $y^+=4.0$, and $y^+=8.0$. The NASTD predicted velocity profile across the viscous layer for these grids is compared with the law of the wall in Figures 33 through 35 and 37. The predicted skin friction from these solutions is compared with the theoretical value in Figure 38. The velocity profiles and skin friction reach a nearly grid independent solution at a wall spacing of $y^+=2.0$.

The effect of viscous layer grid resolution was evaluated using grids n-6 and n-11. Solutions on these grids contain 22 and 40 points across the viscous layer ($y^+ < 800$) respectively. The predicted velocity profile across the viscous layer for these grids is shown in Figures 32 and 36. The predicted skin friction is compared with the theoretical value in Figure 39. The two solutions are very similar indicating that adequate grid resolution is achieved with 22 points.

The effect of surface grid resolution was evaluated by comparing NASTD solutions on grids n-4 and n-8. These grids have surface grid sizes of 118x5 and 69x5 respectively. The skin friction predicted using grids n-4 and n-8 is compared in Figure 40. The similarity of the two solutions indicates that the coarser surface grid provides adequate resolution.

23
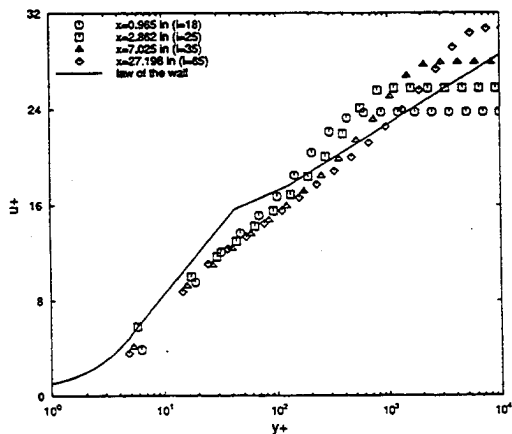
Figure 32. Velocity profile, NASTD solution, Mach 0.1, Re=1.77x10^6, Grid n-6.

Figure 35. Velocity profile, NASTD solution, Mach 0.1, Re=1.77x10^6, Grid n-9.
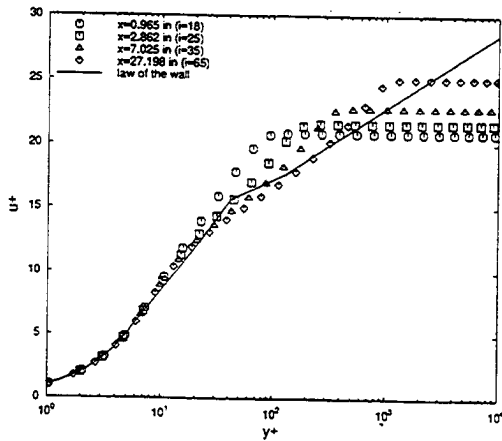
Figure 33. Velocity profile, NASTD solution, Mach 0.1, Re=1.77x10^6, Grid n-7.
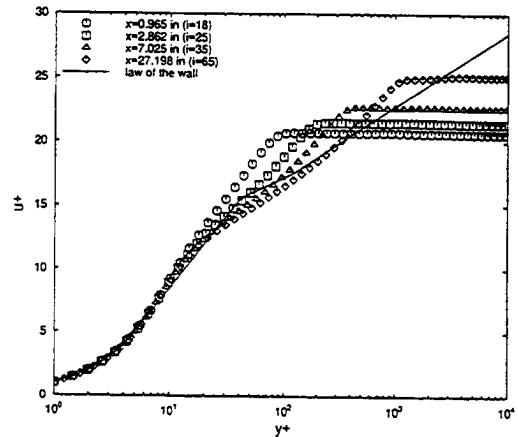
Figure 36. Velocity profile, NASTD solution, Mach 0.1, Re=1.77x10^6, Grid n-11.
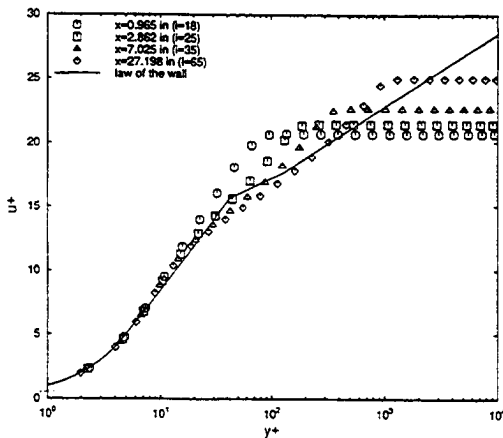
Figure 34. Velocity profile, NASTD solution, Mach 0.1, Re=1.77x10^6, Grid n-8.
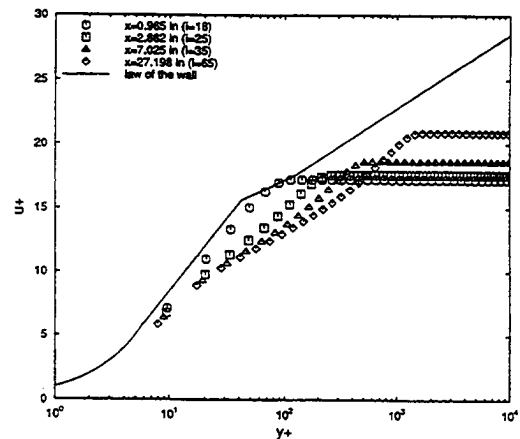
Figure 37. Velocity profile, NASTD solution, Mach 0.1, Re=1.77x10^6, Grid n-14.

24
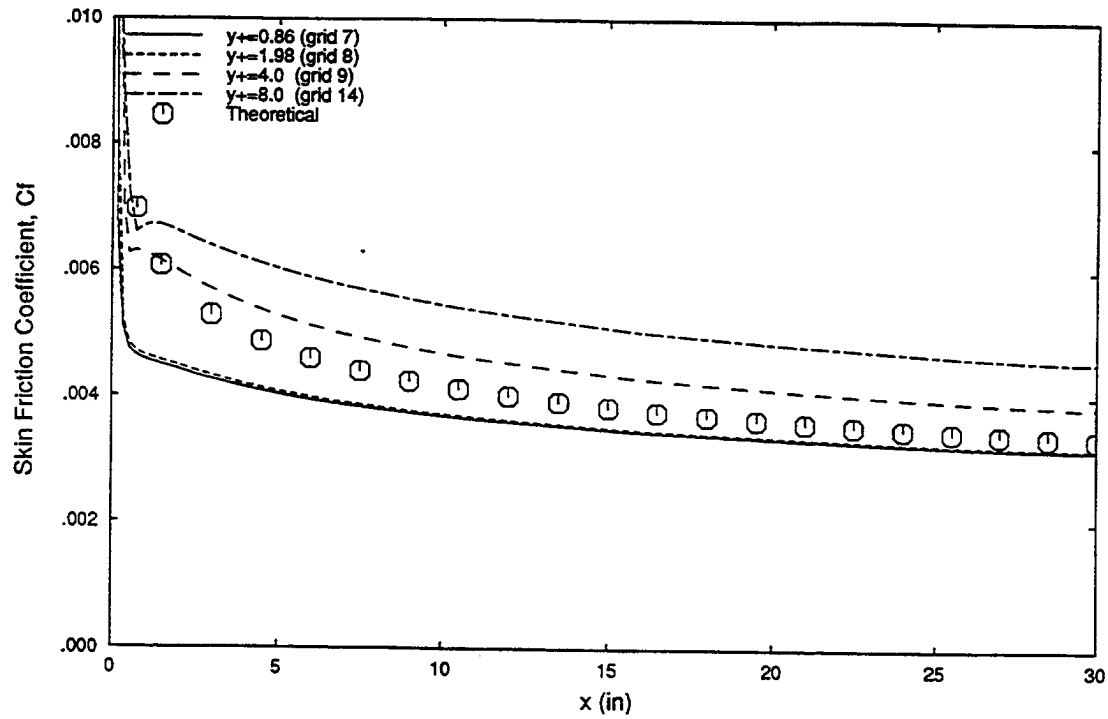
Figure 38. Effect of wall grid spacing on skin friction coefficient, NASTD turbulent solutions, Mach 0.1, Re=1.77 million.

Figure 39. Effect of number of boundary layer points on skin friction coefficient, NASTD turbulent solutions, Mach 0.1, Re=1.77 million.
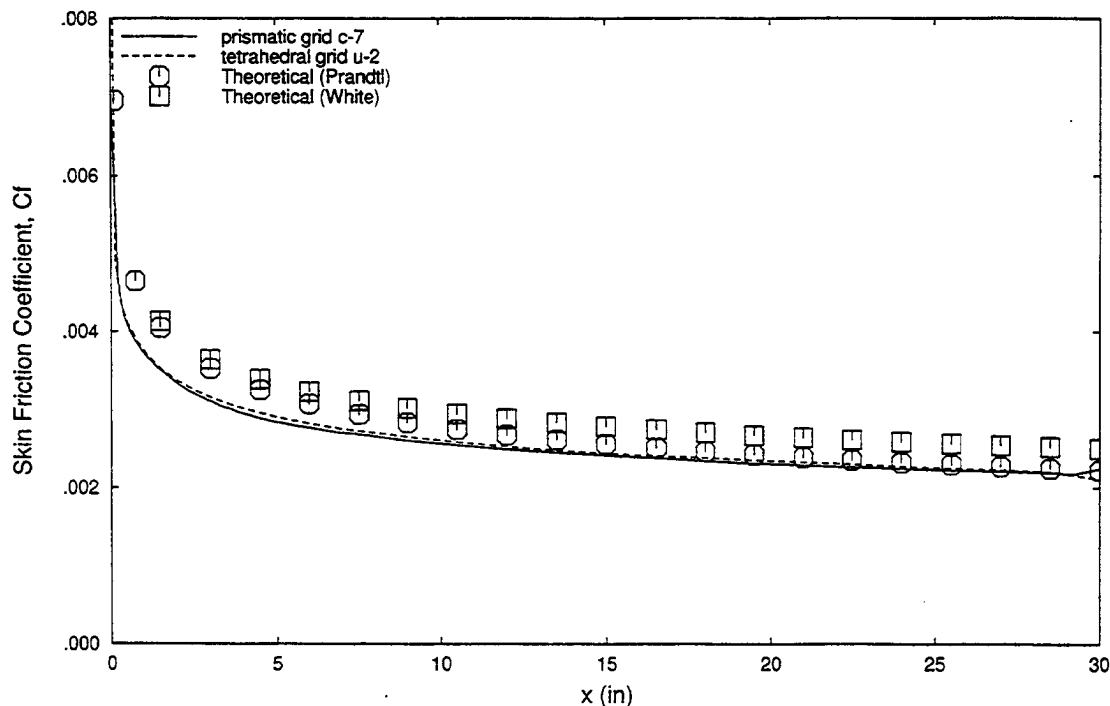
25

Figure 40. Effect of surface grid spacing on skin friction coefficient, NASTD turbulent
solutions, Mach 0.1, Re=1.77 million.

NASTD turbulent flat plate solutions were run at the second run condition of Mach 0.7, and Reynolds number of 12 million. At these run conditions, solutions were generated on grids n-2, n-6, n-7, n-8, n-9, and n-11. These solutions converged relatively quickly requiring approximately 4,000 iterations.

The required wall grid spacing was evaluated by computing solutions on grids n-6, n-7, n-8, and n-9. These grids have wall spacings of $y^+=1.3$, $y^+=4.9$, $y^+=12.4$, and $y^+=23.6$. The predicted velocity profile for these solutions is shown in Figures 41 through 44. The skin friction is compared with the theoretical value in Figure 46. The predicted skin friction is different on all four grids. This indicates that a y^+ value below 4.9 is necessary to reach a nearly grid independent solution.

The effect of viscous layer grid resolution was evaluated with the solutions on grids n-6 and n-11. These grids contain 17 and 30 points across the viscous layer ($y^+ < 800$) respectively at the given run condition. Velocity profile predictions from NASTD solutions on these grids are shown in Figures 41 and 45 and the skin friction is shown in Figure 47. The skin friction and velocity profiles from the two solutions are very similar indicating that adequate grid resolution is achieved with 17 points. The effect of surface mesh resolution was evaluated by comparing solutions on grids n-2 and n-6. These grids contain surface grid sizes of 118x5 and 69x5 respectively. Skin friction predictions for these two solutions are shown in Figure 48. The similarity of these two solutions indicates the coarser surface grid provides adequate grid resolution.
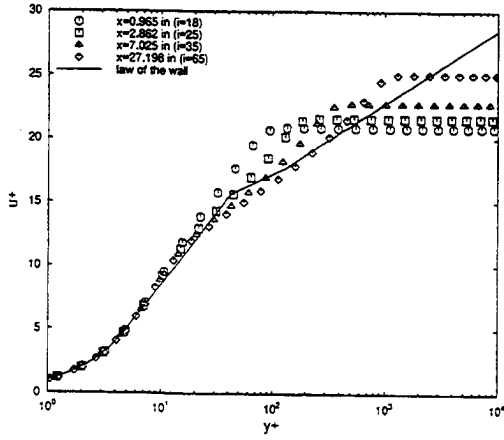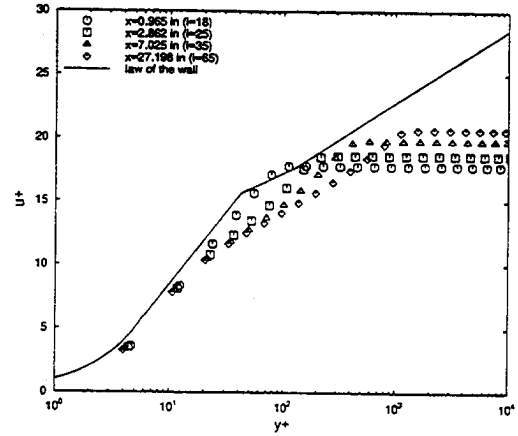
26
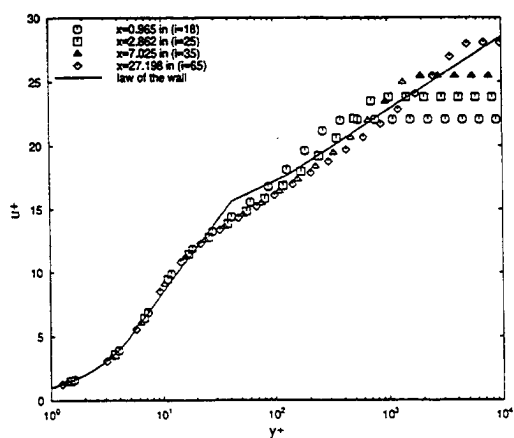
Figure 41. Velocity profile, NASTD solution, Mach 0.7, Re=12 million, Grid n-6.

Figure 44. Velocity profile, NASTD solution, Mach 0.7, Re=12 million, Grid n-9

Figure 42. Velocity profile, NASTD solution,Mach 0.7, Re=12 million, Grid n-7

Figure 45.Velocity profile, NASTD solution, Mach 0.7, Re=12 million, Grid n-11.

Figure 43. Velocity profile, NASTD solution, Mach 0.7, Re=12 million, Grid n-8.

27

Figure 46. Effect of wall grid spacing on skin friction coefficient,NASTD turbulent solutions, Mach 0.7, Re=12 million.
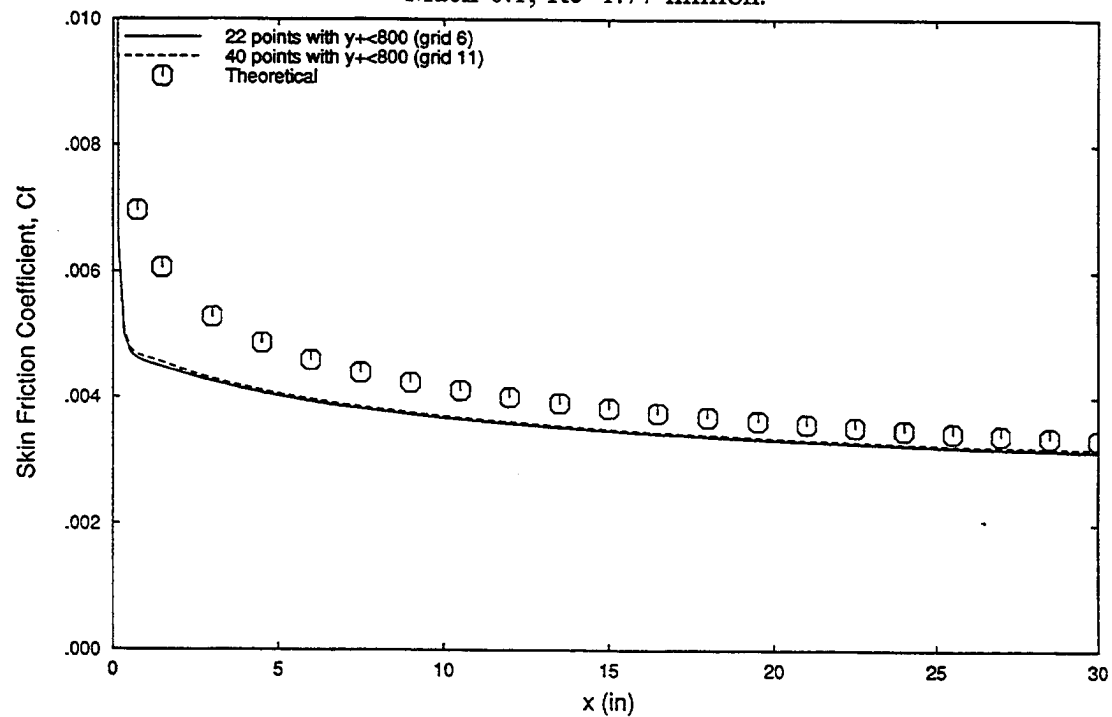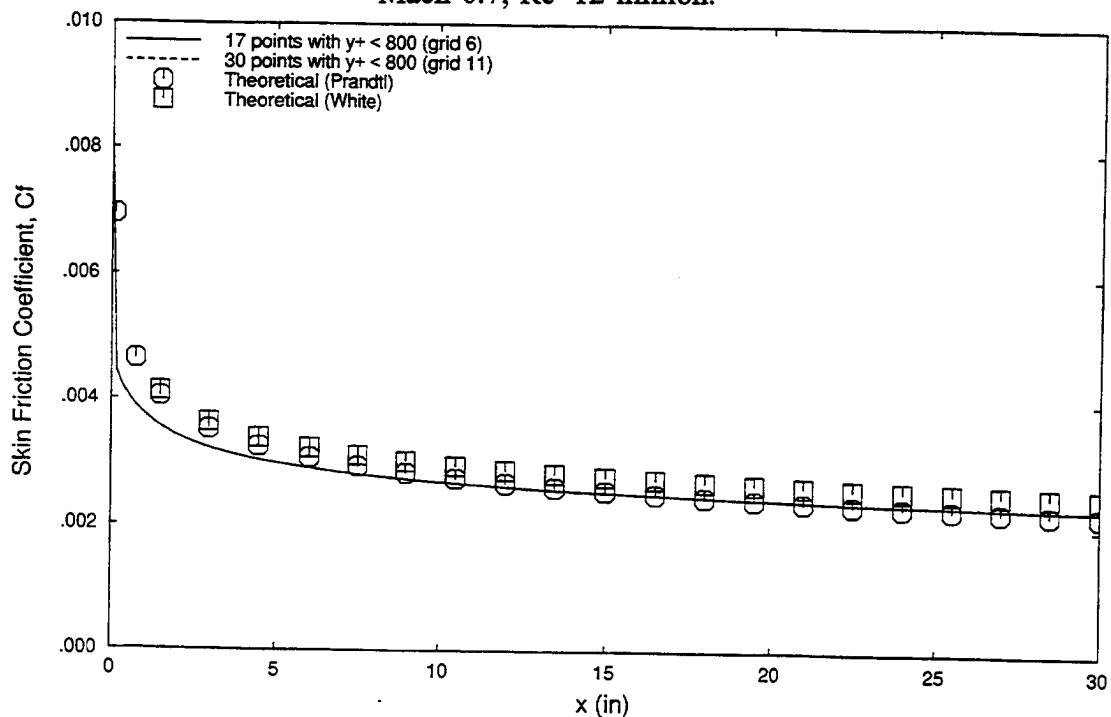

Figure 47. Effect of number of boundary layer points on skin friction coefficient, NASTD turbulent solutions, Mach 0.7, Re=12 million.

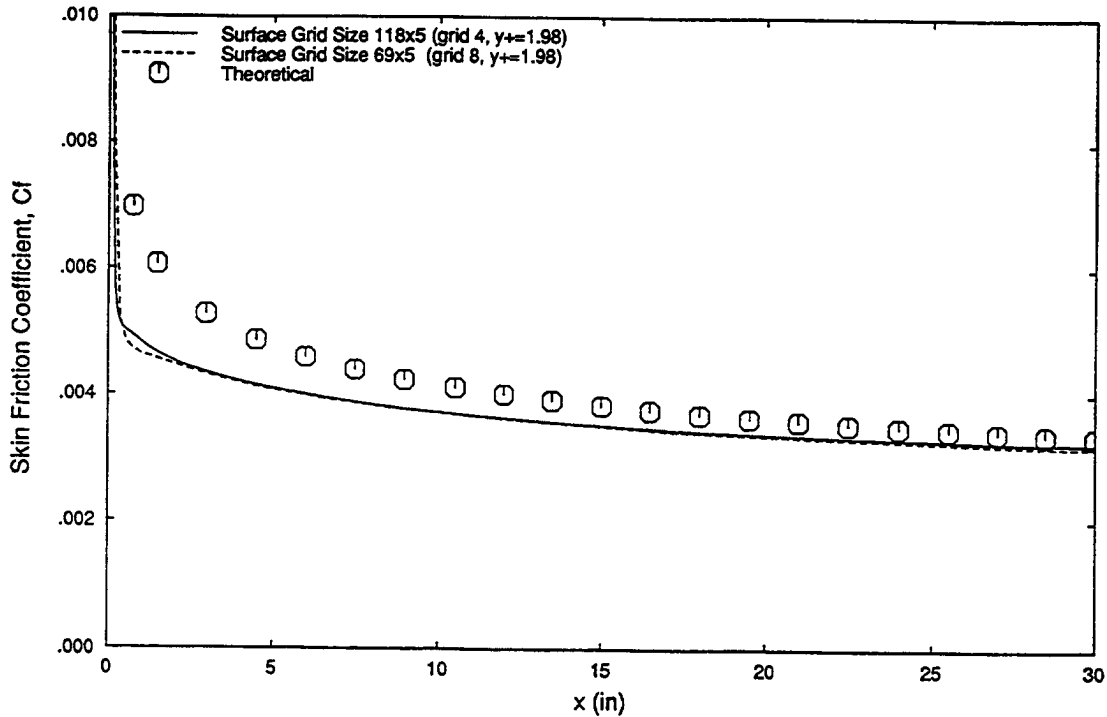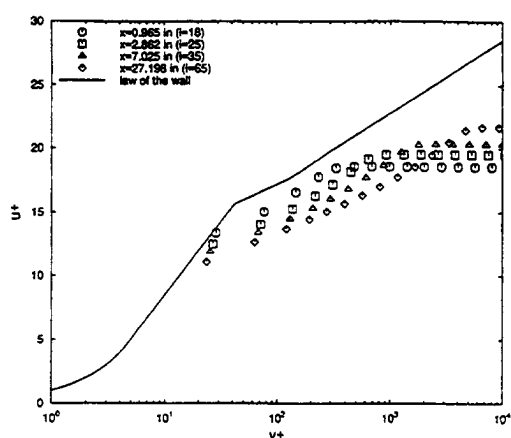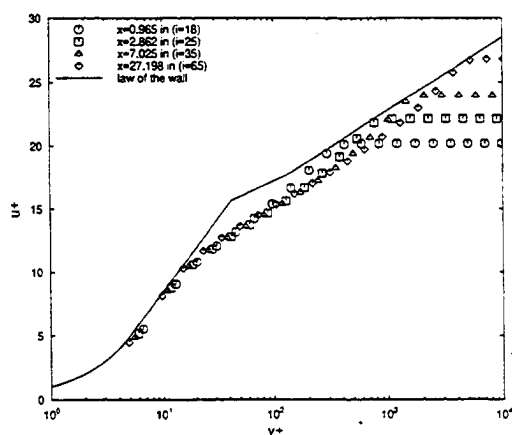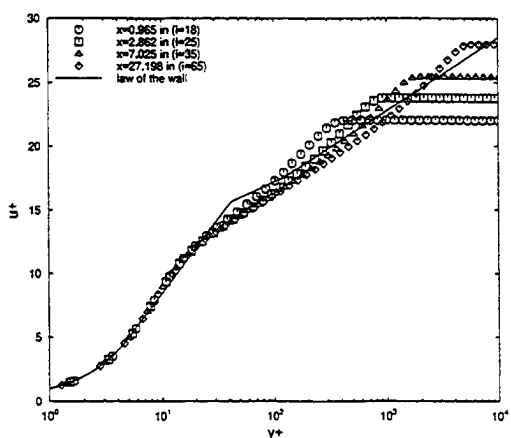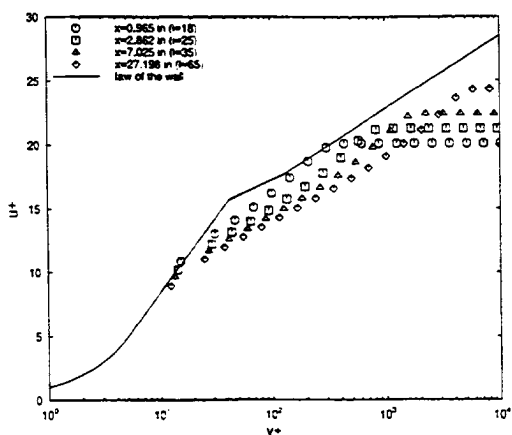28
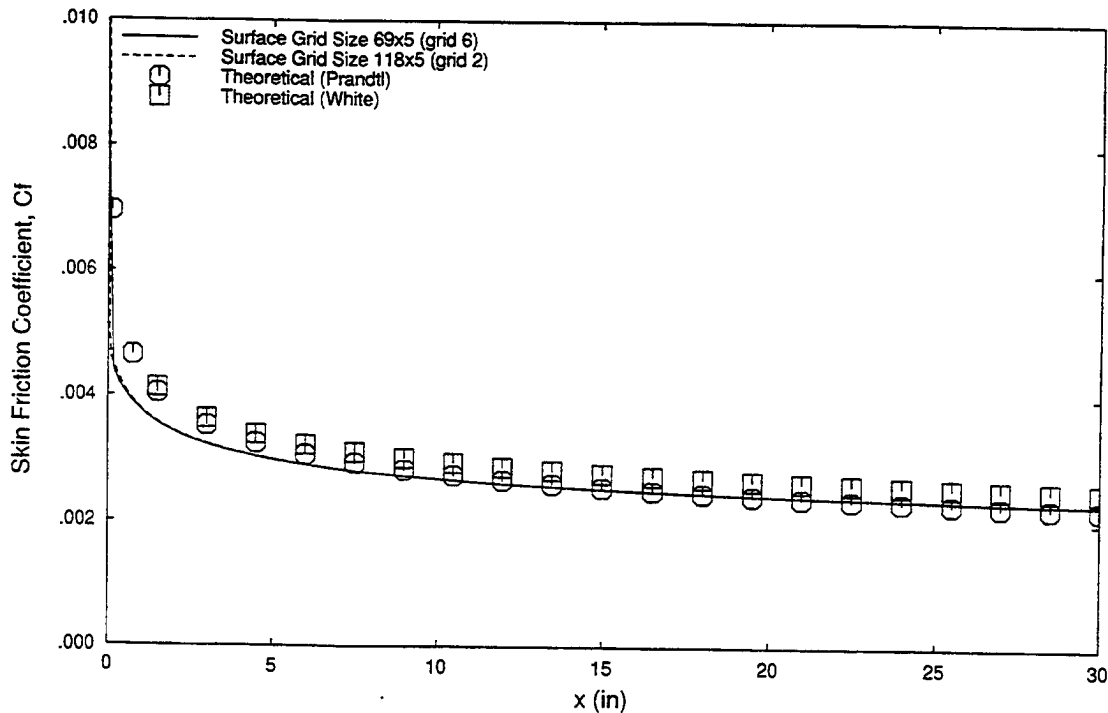
Figure 48. Effect of surface grid resolution on skin friction coefficient, NASTD turbulent solutions, Mach 0.7, Re=12 million.

3.4.3 USM3D Results

USM3D turbulent flat plate solutions were generated at the first run condition of Mach 0.1, Reynolds number of 1.77 million on grids u-2, u-3, u-5, and u-4. These solutions required between 5,000 and 10,000 iterations to reach solution convergence.

The required grid spacing at the wall was evaluated by comparing solutions on grids u-2, u-3, u-5, and u-4. These grids have wall grid spacings of $y^+=1.1$, $y^+=25.4$, $y^+=49.0$, and $y^+=73.8$ respectively. Predicted velocity profiles across the viscous layer are compared with the law of the wall at four locations on the plate in Figures 49 through 52. The predicted skin friction from each solution is compared with the theoretical value in Figure 53. For y^+ values above 49.0, the predicted skin friction compares very well with the theoretical values. At these large wall grid spacings, the skin friction is primarily governed by the wall function. The predicted skin friction on grids u-2 and u-3, however, does not agree as well. At these tighter wall grid spacings the wall function has a smaller influence on the near wall solution. The poor solution at the tighter grid resolution seems to indicate lack of convergence of the solution or improper treatment of the solution computation on highly stretched grid cells. Reasons for this discrepancy were not investigated beyond running the solution at a lower CFL number which had no effect.

USM3D turbulent flat plate solutions were generated at the second run condition of Mach 0.7, and Reynolds number of 12 million on grids u-1, u-6, and u-3. These solutions converged relatively quickly requiring approximately 4,000 iterations at a CFL number of 200.

Wall grid spacing sensitivity was evaluated by comparing the three solutions. These solutions have wall grid spacings of $y^+=18.2$, $y^+=68.9$, and $y^+=122.4$ respectively. The predicted

29

velocity profile is shown in Figures 54 through 56 and the skin friction is shown in Figure 57. Once again the skin friction is in excellent agreement with the theoretical values for grid spacings above $y^+=49.0$. However, at the smallest wall grid spacing where the wall function is losing its influence, the skin friction agreement is worse.
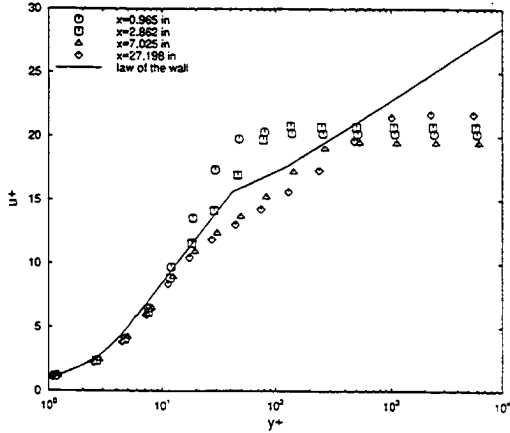
Figure 49.Velocity profile, USM3D turbulent solution, Mach 0.1, Re=1.77x10^6, Grid u-2.
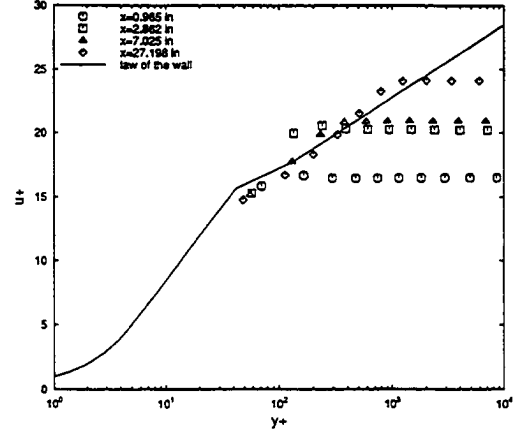
Figure 51.Velocity profile, USM3D turbulent solution, Mach 0.1, Re=1.77x10^6, Grid u-5.
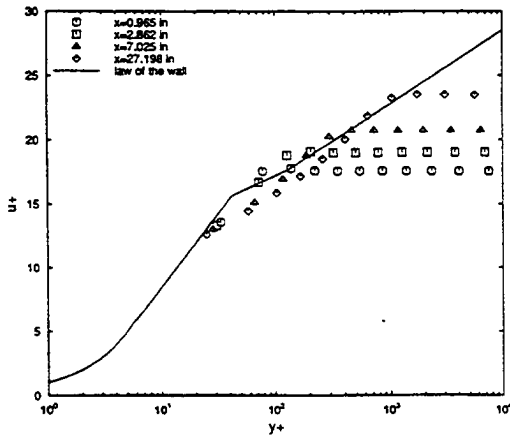
Figure 50. Velocity profile,USM3D turbulent solution, Mach 0.1, Re=1.77x10^6, Grid u-3.
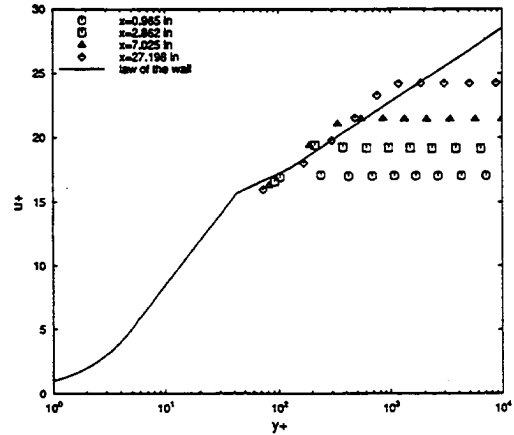
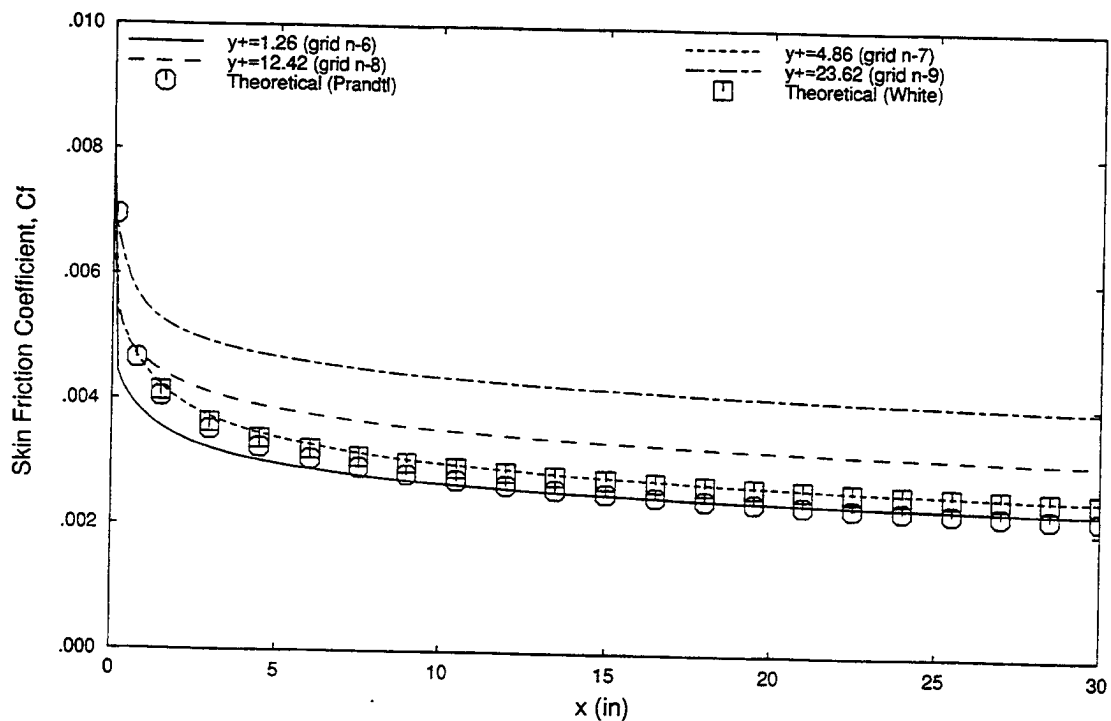Figure 52. Velocity profile,USM3D turbulent solution,Mach 0.1, Re=1.77x10^6, Grid u-4.
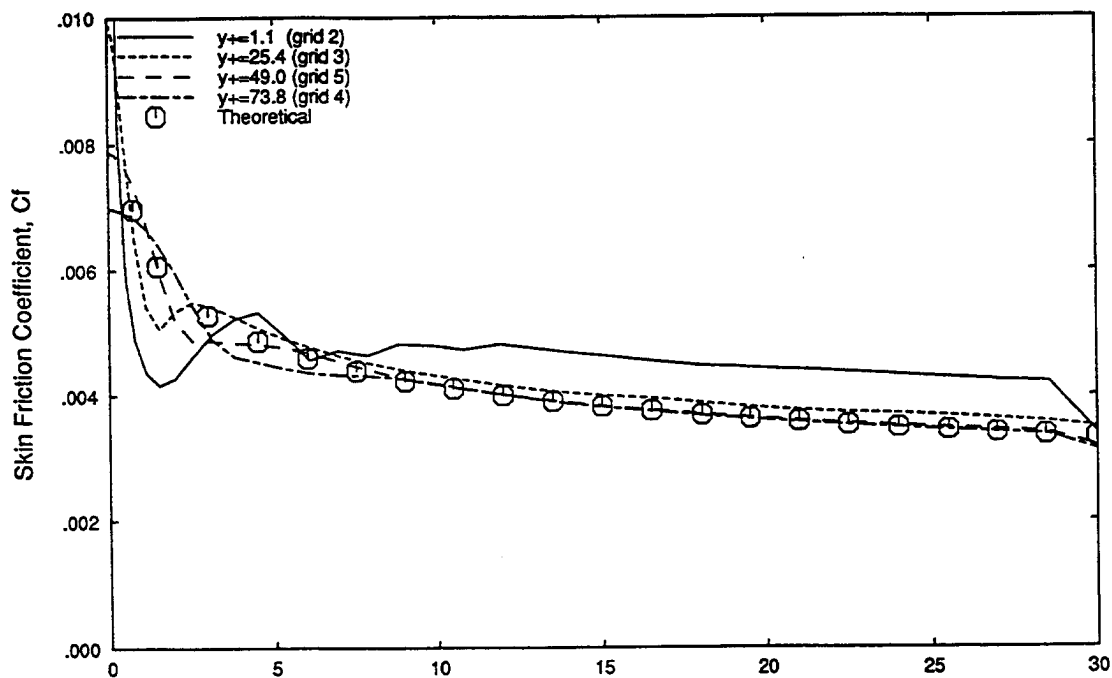
Figure 53. Effect of wall grid spacing on skin friction coefficient, USM3D turbulent solutions, Mach 0.1, Re=1.77 million.
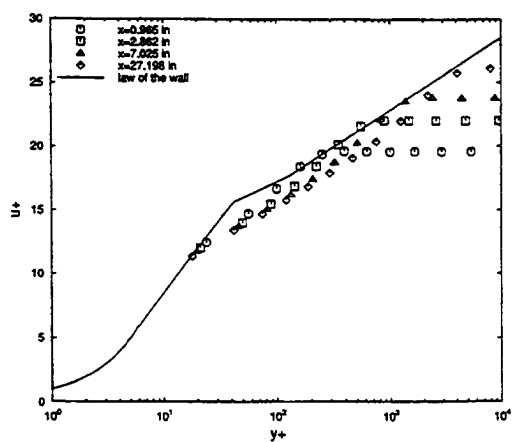

Figure 54.Velocity profile, USM3D turbulent solution, Mach 0.7, Re=12x10^6, Grid u-1.
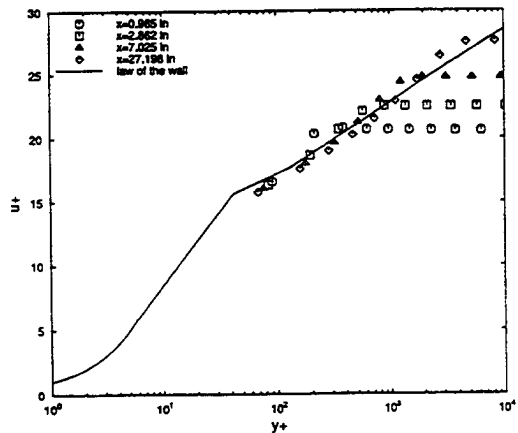
Figure 55.Velocity profile, USM3D turbulent solution, Mach 0.7, Re=12x10^6, Grid u-6.
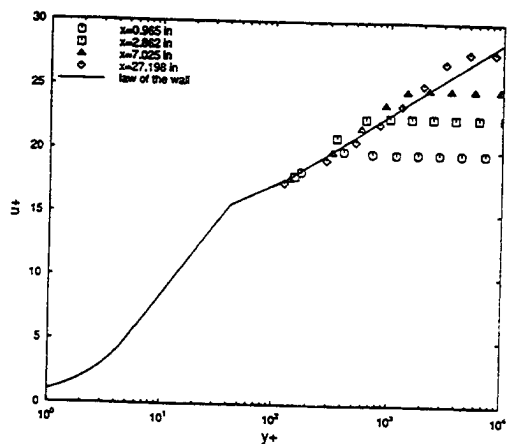
Figure 56. Velocity profile, USM3D turbulent
solution, Mach 0.7, Re=12x10^6, Grid u-3.
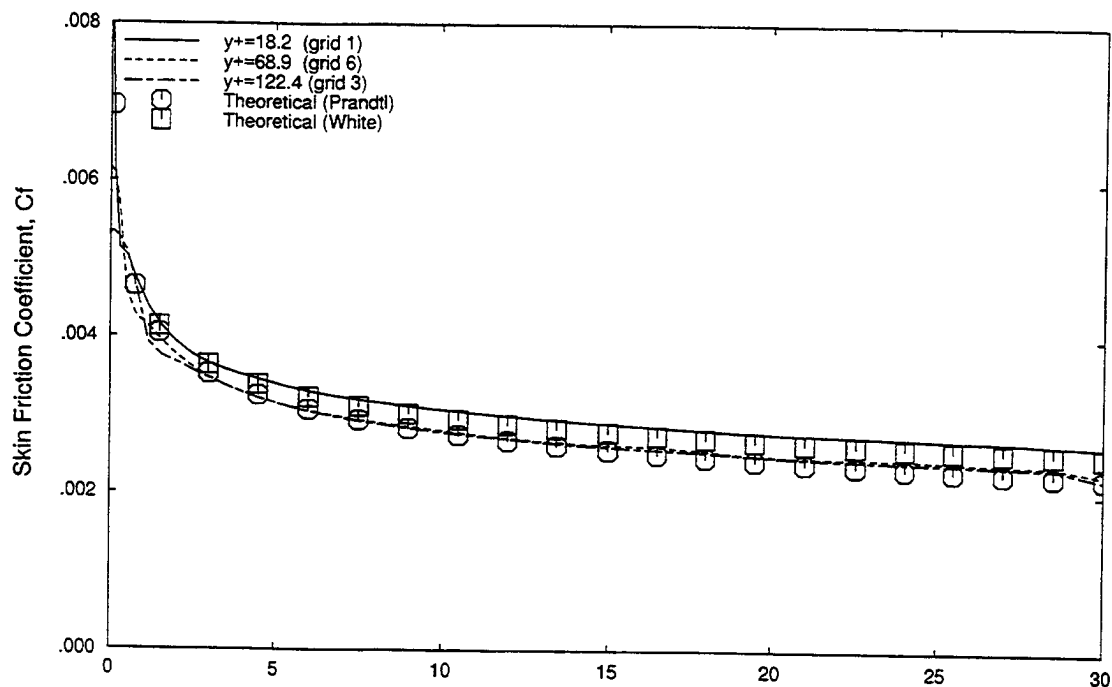
Figure 57. Effect of wall grid spacing on skin friction coefficient,USM3D turbulent solutions,
Mach 0.7, Re=12 million.

3.5 Unstructured Grid Requirements

The grid requirements identified in the previous section are summarized below. Most of the requirements that are given in this section are given as ranges rather than specific numbers. These requirements are meant to be used as guidelines in the development of future grids. Since these grids will most likely not be over flat plates, the given requirements should only be used as a reference point. These requirements are also only valid for the specific grid cell shape that was tested with each flow solver (*i.e.* prism for Cobalt, hexahedral for NASTD, tetrahedral for

32

USM3D).

A summary of the grid requirements identified for each flow solver is shown in Table 3. Two grid parameters are given for each case. These are the distance between the wall and the first point normal to the surface (wall spacing), and the number of points across the boundary layer identified as the number of points below $y^+ = 800$. A blank entry in Table 3 indicates the parameter was not determined for that case.

Table 3. Flat Plate Grid Requirements

Solver	Reynolds Number $x10^{-6}$	laminar/ turbulent	Grid Requirements		
			maximum wall spacing	# BL points	Surface Grid Size
Cobalt	1.77	laminar	$12.2 < y^+ <$		
Cobalt	1.77	turbulent	$1.3 < y^+ < 2.2$	> 22	
Cobalt	12.0	turbulent	$3.0 < y^+ < 7.7$	> 17	
NASTD	1.77	laminar	$10.2 < y^+ <$		
NASTD	1.77	turbulent	$2.0 < y+ < 4.0$	> 22	>272
NASTD	12.0	turbulent	$1.3 < y^+ < 4.9$	> 17	>272
USM3D	1.77	laminar	$12.2 < y^+ <$	> 6	
USM3D	1.77	turb/wall func	$73.8 < y^+ <$	> 5	
USM3D	12.0	turb/wall func	$122.4 < y^+ <$	> 5	

3.6 Flow Solver Comparisons

A comparison of the accuracy and efficiency of each of the three unstructured grid methods is presented in this section. The comparison is based on the data generated in the grid refinement study presented above.

3.6.1 Accuracy

The different grid topologies used with each flow solver precludes an equitable one-to-one comparison of flow solver accuracy independent of the grid. However, an indication of the relative accuracy of each flow solver/ grid combination can be made.

The results obtained at the laminar run condition of Mach 0.1, Re=1.77 provides the opportunity to compare flow solvers in the absence of turbulence model effects. The predicted skin friction from each of the methods is compared with the Blasius solution in Figure 58. The Cobalt and NASTD results are both very close to the Blasius solution with the USM3D solution being the worst of the three. The Cobalt solution does a slightly better job of predicting the skin friction near the leading edge of the plate. The predicted velocity profiles near the trailing edge of the plate are shown in Figure 59. All three methods do a good job of matching the Blasius profile.

33
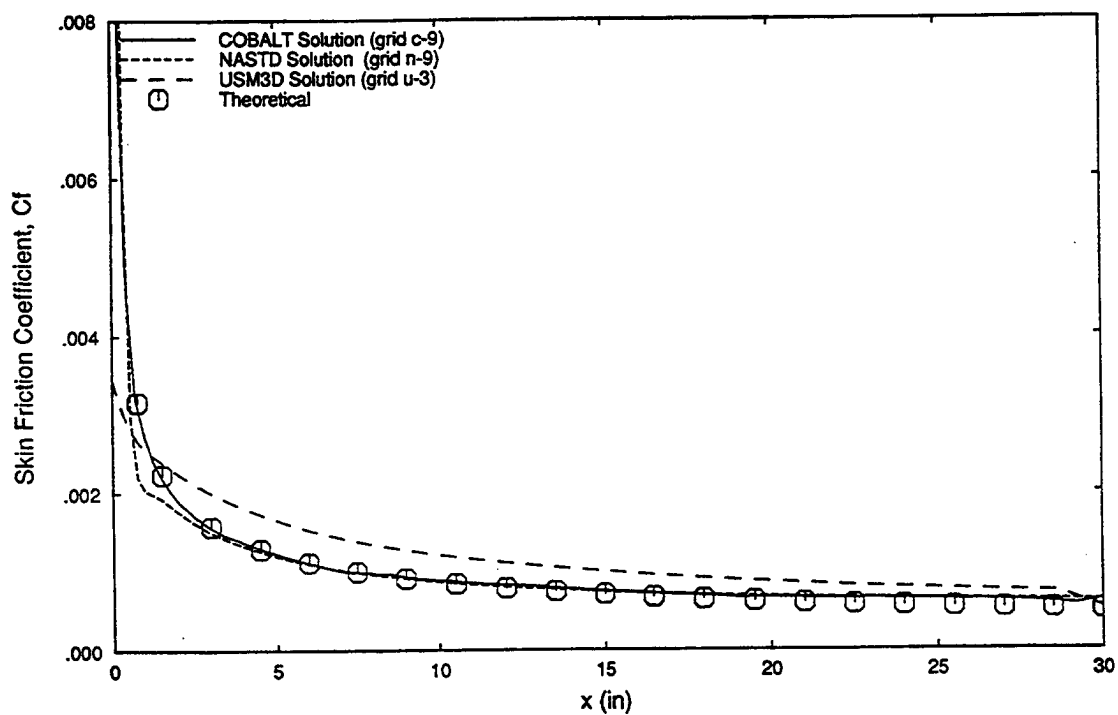
Figure 58. Comparison of Predicted Laminar Flat Plate Skin Friction, Mach 0.1, Re=1.77 Million.
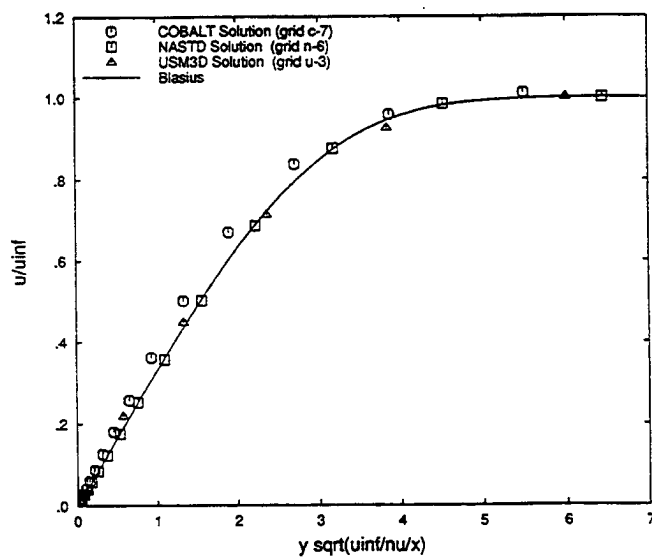
Figure 59. Comparison of Predicted Laminar Velocity Profile, Mach 0.1, Re=1.77 Million.

34

The second set of run conditions, Mach 0.1, Re=1.77 million, provides a comparison of the three methods in a turbulent nearly incompressible flow. In Figure 60 the predicted skin friction is compared with the theoretical skin friction for fully turbulent flow. The USM3D solution with the wall function does a very good job of matching the theoretical value. The Cobalt and NASTD results differ from the theoretical value near the leading edge and approach the theoretical value towards the trailing edge. Velocity profiles from the three methods are compared with the law of the wall profile in Figure 61. All three methods match the theoretical profile reasonably well.

Cobalt and USM3D solutions were generated on grid u-2 at Mach 0.1, Re=1.77 million. These solutions provide an equitable comparison of flow solver accuracy since any grid dependencies have been removed. The predicted skin friction from the two solutions is shown in Figure 62. Neither method matches the theoretical values. However, the Cobalt results are smooth and have the correct trends whereas the USM3D results are very erratic.

Figure 60. Comparison of Predicted Turbulent Flat Plate Skin Friction, Mach 0.1, Re=1.77x10^6
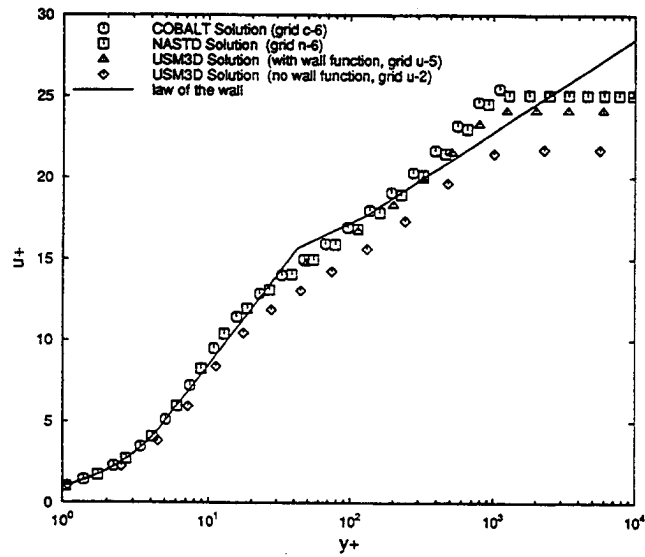
Figure 61. Comparison of Predicted Turbulent Velocity Profile, Mach 0.1, Re=1.77x 10^6
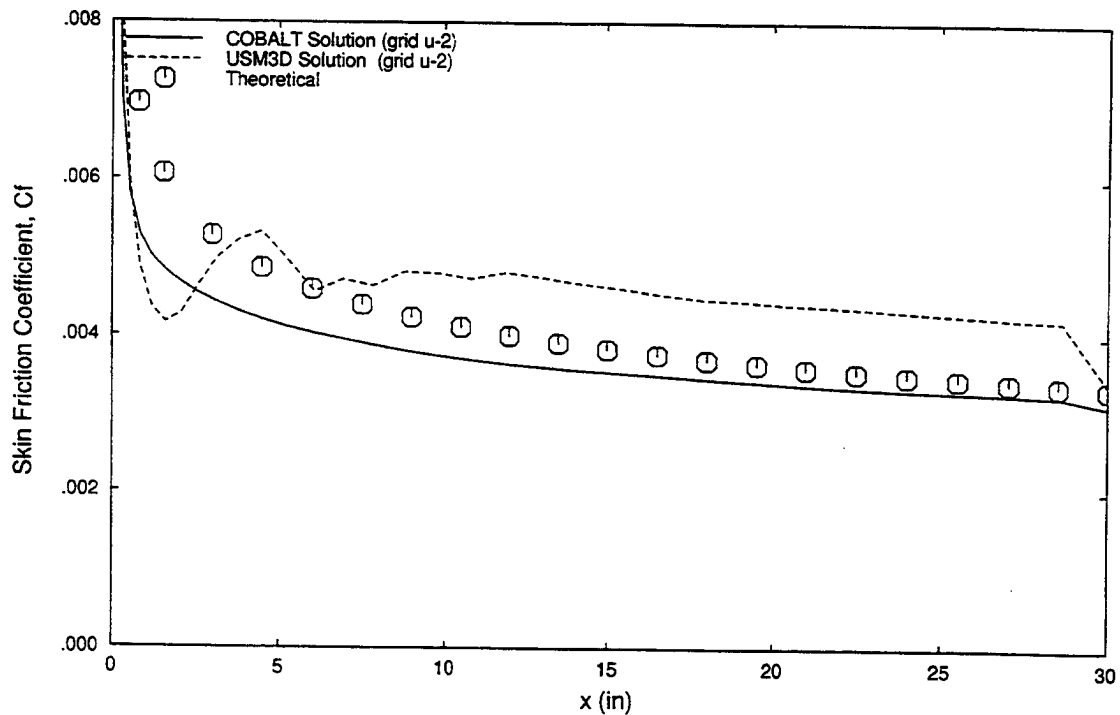
Figure 62. Comparison of Cobalt and USM3D Predicted Turbulent Flat Plate Skin Friction, Mach 0.1, Re=1.77x10^6, Grid u-2.

36

The final run condition of Mach 0.7, Re=12 million, provides a comparison of the three methods in a high Reynolds number turbulent flow. The skin friction from the three methods is compared with the theoretical value in Figure 63. Once again the USM3D results with the wall function compare very well with the theoretical value. The NASTD and Cobalt results also compare reasonably well. The predicted velocity profiles are compared with the law of the wall profile in Figure 64. All three methods provide similar results.
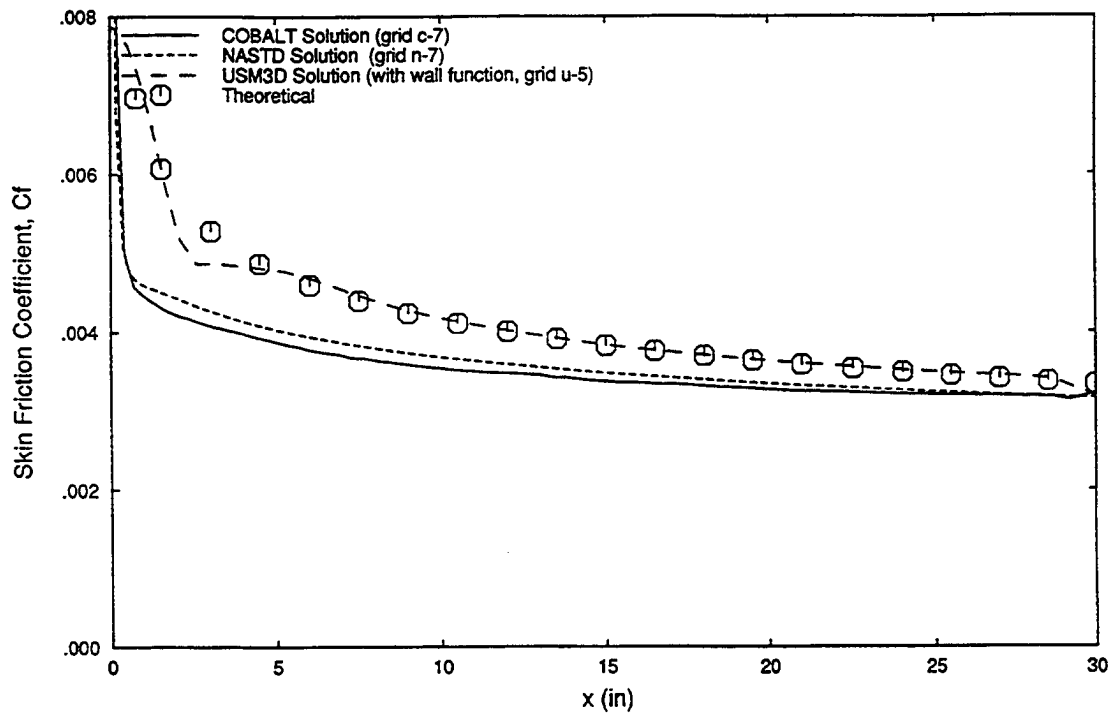

Figure 63. Comparison of Predicted Turbulent Skin Friction, Mach 0.7, Re=12x10^6

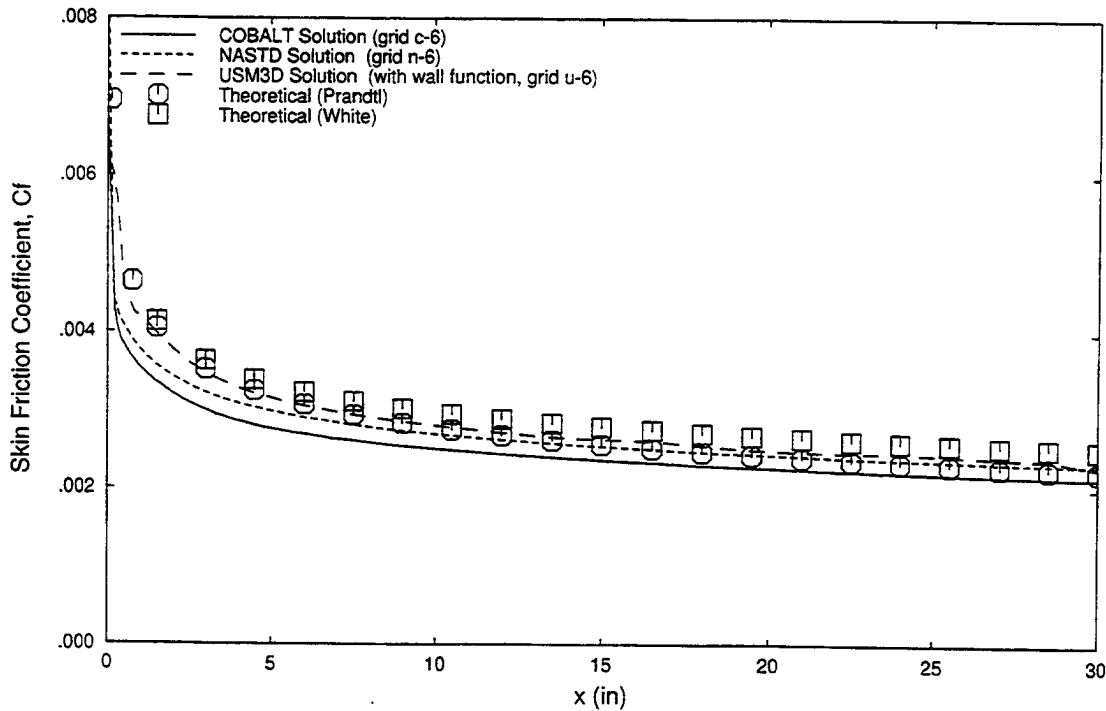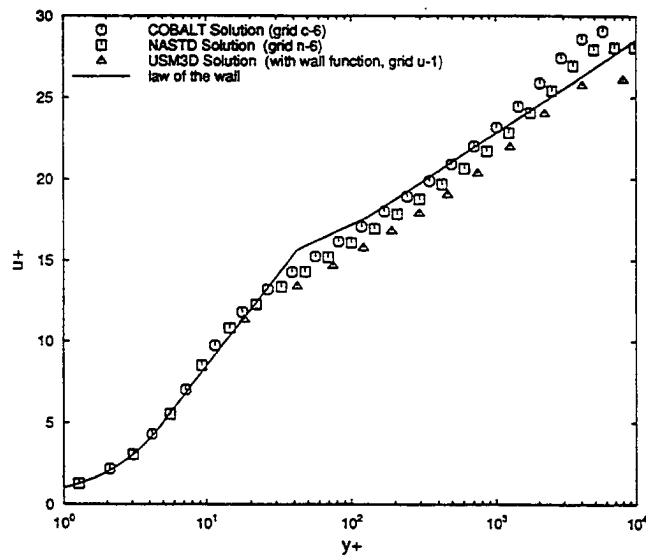Figure 64. Comparison of Predicted Turbulent Velocity Profile, Mach 0.7, Re=12x10^6.

37

3.6.2 Efficiency

It is difficult to compare the efficiencies of the flow solvers based on the solutions computed in this study due to differences in grid sizes. However, an estimate of the comparable run times for the different solvers can be made by comparing the time per iteration per cell and the total number of iterations required to reach convergence. This comparison does not include penalties associated with the grid cell topology. For instance, a tetrahedral cell grid will contain a larger number of cells in the boundary layer than a hexahedral cell grid. A discussion of these penalties is given below.

The run times per iteration per cell for each of the flow solvers is given in Table 2. These numbers were obtained by averaging run times for several solutions on an HP-735 workstation. If we multiply these numbers by the number of iterations required to reach convergence we obtain an overall solution time per cell for each flow solver. Comparing the numbers for the turbulent flat plate solutions at a Reynolds number of 1.77 million we find that the Cobalt, NASTD, and USM3D solvers take roughly 47, 24, and 20 seconds per solution per cell. These times were obtained using an average number of iterations per solution of 160,000 (Cobalt), 25,000 (NASTD), and 12,000 (USM3D) iterations. For an equal size grid, there is a ratio of 2:1 between Cobalt and NASTD or USM3D solution times. This difference is most likely due to the explicit time integration scheme of Cobalt versus the implicit schemes in NASTD and USM3D. When taking advantage of the wall function, (grids with $y^+ > 25$), USM3D was able to reduce the run time by another factor of 2.

There was a large variation in the memory requirements for each flow solver. Once again the comparisons will be made on a per cell basis ignoring any penalties associated with the grid cell topology. For the laminar flat plate solutions the Cobalt, NASTD and USM3D flow solvers each required 180, 95 and 253 single precision words of memory per cell. For the turbulent flat plate solutions these solvers required 185, 97 and 256 single precision words of memory per cell. The NASTD memory requirements are much lower than for Cobalt and USM3D. This is primarily due to the lower memory requirements of a structured grid data set. USM3D has the largest memory requirements most likely due to the implicit time integration scheme.

The grid cell topology can play a large role in the efficiency of the flow solution. This is primarily dependent on the number of cells required to resolve the viscous layer and the increase in work per cell to compute the fluxes across each cell face. Intuitively it would seem that a tetrahedral grid will require the largest number of cells to achieve a given level of resolution while prismatic and hexahedral cells should allow the most efficient modeling of the viscous layer. In this study, however, grids containing prismatic cells were much larger than the corresponding tetrahedral or hexahedral grids. This was driven by the attempt to maintain isotropic triangular faces near the leading edge of the plate where the streamwise spacing was reduced. The hexahedral and anisotropic tetrahedral grids were able to resolve this streamwise spacing without increasing the resolution in the crosswise direction. Further study of the effect of grid cell type on grid size is needed.

4. UNSTRUCTURED GRID ASSESSMENT: ONERA WING

The ONERA M6 wing has been used extensively throughout the CFD community for the evaluation and validation of CFD codes. The availability of an excellent set of test data for this geometry makes it well suited for evaluating CFD codes across a range of flow conditions (4). Viscous unstructured grid solutions were computed at two run conditions with each of the three unstructured grid methods. The flowfield at the first run condition of Mach 0.84, α=0.04, Re=11.7 million is subsonic and remains attached across the entire wing span. The flowfield at the second condition of Mach 0.84, α=5.06, Re=11.7 million is transonic with a shock induced separation over the outer one third of the wing. A total of 11 solutions were computed on 7 grids.

4.1 Grid Generation

Grids were generated about the ONERA wing using each of the three grid generator packages. Mixed cell grids containing prismatic and tetrahedral cells were generated within TETMESH. Zonal hybrid grids containing hexahedral and tetrahedral grids were generated in MACGS. Anisotropic tetrahedral grids were generated in VGRID. A summary of the seven grids generated for this study is given in Table 4. Each grid name provides three pieces of information, the first letter indicates the grid generator that was used to create the grid, the second letter indicates whether the grid is appropriate for euler (inviscid) or viscous analysis, and the last number is used to distinguish between multiple grids containing the same first two letters. For instance grid tv2 is the second viscous packed grid generated in TETMESH.

Table 4. ONERA Wing Grid Summary

Grid	Grid Generator	Surface Size	Number of Cells	Number of Points	$\Delta y/c_{Root}$
ne1		15,279	231,507	42,410	N/A
te1	TETMESH	11,568	163,930	30,308	N/A
te2	TETMESH	32,510	220,251	43,807	N/A
tv1	TETMESH	20,160[a]	422,614[a]	175,522[a]	0.000015
mv1	MACGS	3,264	366,273	138,148	0.000031
vv1	VGRID	6,483	356,472	62,883	0.000203
vv2	VGRID	6,483	414,038	96,116	0.000060

[a] sizes are for full wing grid (no symmetry plane)

4.2 Cobalt/TETMESH Results

A total of 5 Cobalt solutions were computed on 4 grids. All of the solutions were run with the single processor, explicit time integration version of Cobalt. Prior to this study, we have had very little experience running Cobalt on which to base a determination of adequate surface grid resolution. An inviscid study was therefore performed to identify an adequate surface grid resolution to model the important physics of the problem. We encountered several difficulties

while generating viscous grids on the ONERA M6 wing in TETMESH. As a result, only one viscous TETMESH grid was generated. These difficulties are outlined below along with a presentation of the Cobalt results.
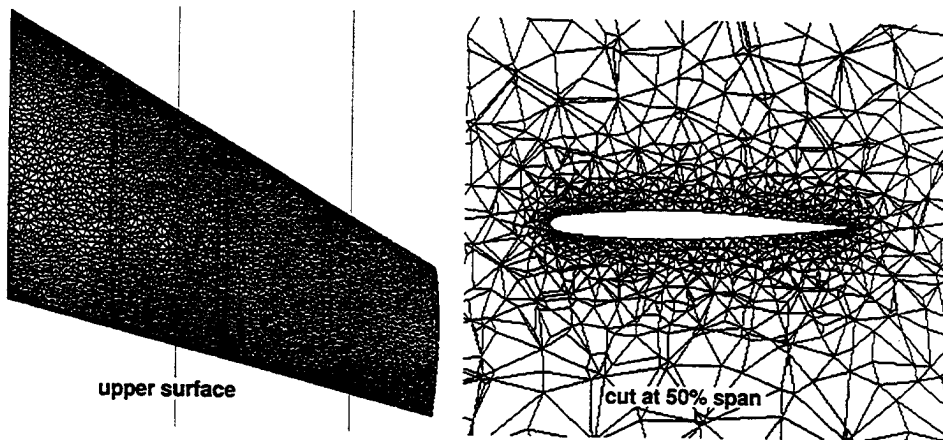
4.2.1 Surface Grid Resolution Study

A grid refinement study was performed to identify surface grid requirements for the Cobalt flow solver. Two grids (te1 and te2) were generated with TETMESH. A third mesh, ne1, which came from a NASA Langley workshop on unstructured grid methods was also used. The grid sizes are summarized in Table 4. The surface mesh and a mid-span cut through the volume grid of each mesh is shown in Figure 65. Grid ne1 has a higher concentration of surface grid nodes near the leading edge relative to the other grids. The volume cell size of the TETMESH grids grow very rapidly away from the wing surface. More control over this stretching would be desirable. Cobalt Euler solutions were computed at run conditions of Mach 0.84 and angle of attack of 3.04 degrees. Predicted surface pressures at four spanwise cuts are compared with experimental data in Figure 66. The solutions on all three meshes are similar.

The shock predictions on the te2 mesh are slightly crisper because of the increased surface resolution. The greatest differences can be seen at the 65% span location where the te1 mesh solution completely smears over the first shock. The surface solution on mesh ne1 is smoother than the solutions on meshes te1 and te2. This may be due to the smooth ordering of surfaces faces in mesh ne1. It appears that a surface mesh resolution somewhere between te1 and te2 is required to adequately resolve the flowfield features. Unfortunately we were unable to achieve this level of surface grid resolution in the viscous meshes we generated with TETMESH. The size of our viscous TETMESH grids was limited by the memory requirements of TETMESH and the available memory on the machine we were running on.

40
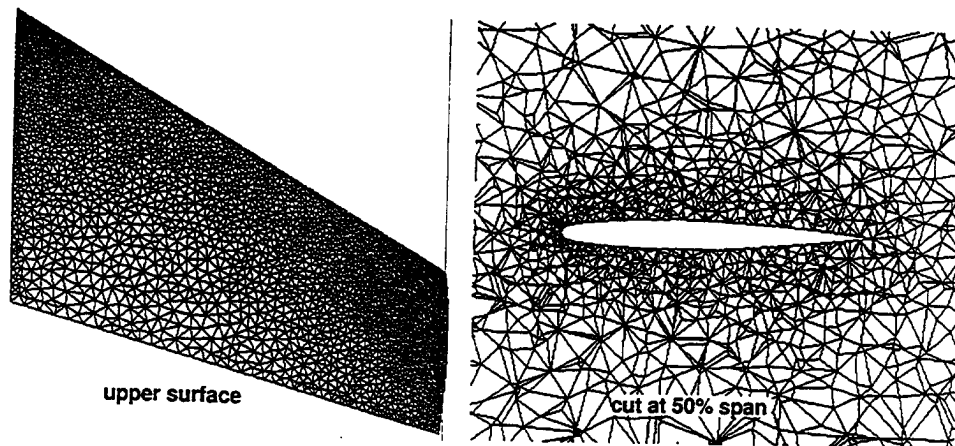
a) grid te1 (11,568 surface faces, 163,930 tetrahedra)

b) grid te2 (32,510 surface faces, 220,251 tetrahedra)
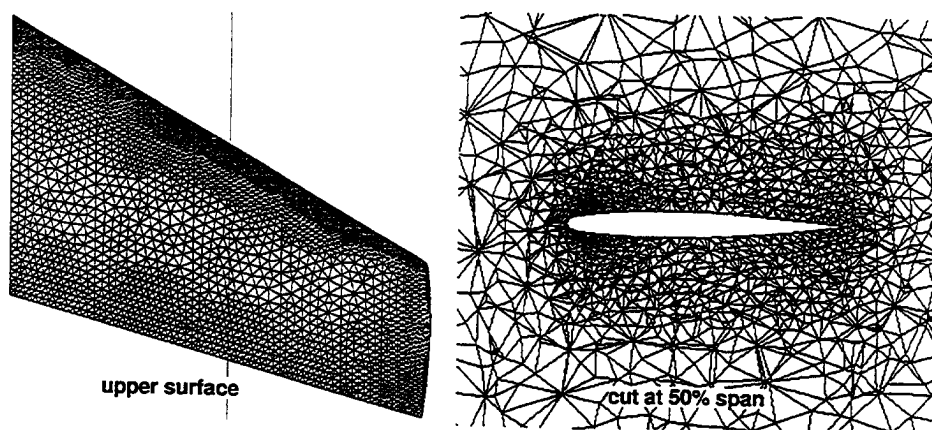
c) grid ne1 (15,279 surface faces, 231,507 tetrahedra)

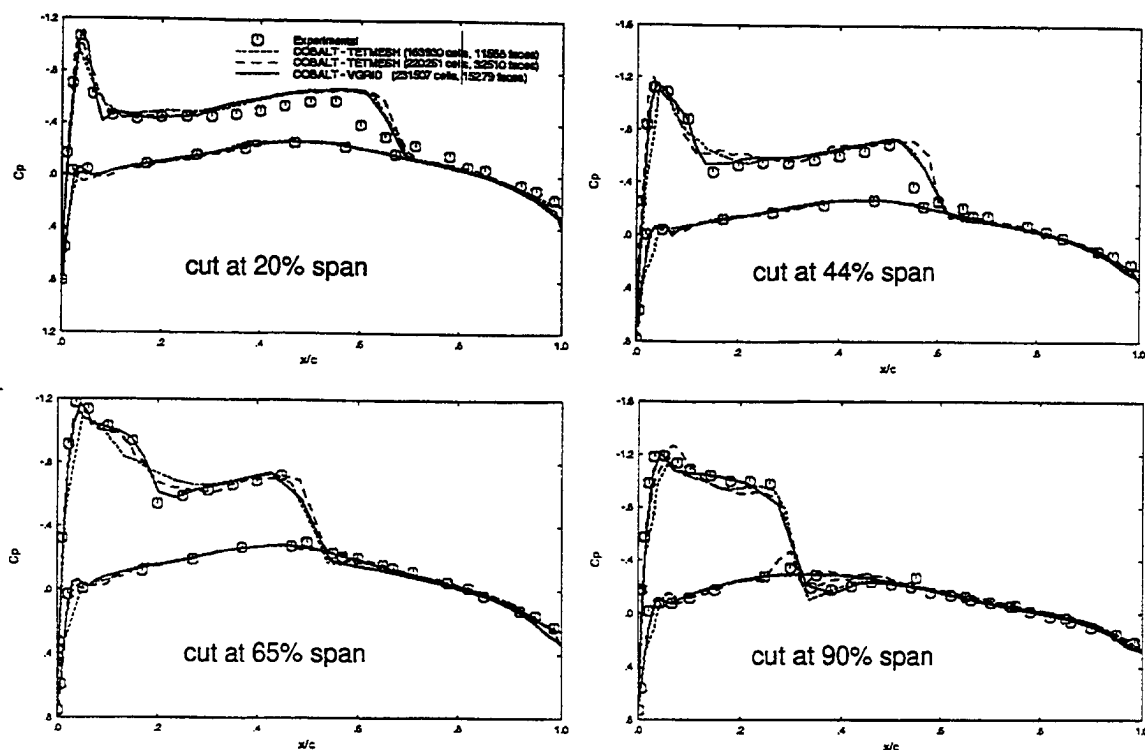Figure 65. Surface Grid Resolution Study - Tetrahedral Grids About ONERA M6 Wing.

Figure 66   Predicted Surface Pressure Coefficient From Cobalt Surface Grid Resolution Study on ONERA M6 Wing (Mach 0.84, α=3.04 degrees).

4.2.2 Viscous Results

TETMESH was used to generate prismatic/tetrahedral grids for viscous analysis of the ONERA M6 Wing. We were unable to generate a viscous packed grid about an object with a symmetry plane in TETMESH. The wing surface was therefore reflected about the symmetry plane and the volume grid was generated on the full wing geometry (no symmetry plane). This reduced the grid resolution by a factor of two since our grid sizes were limited by the amount of available memory. The surface grid and a cut through the volume grid of a TETMESH generated viscous mesh (tv1) are shown in Figure 67. This grid contains 20,160 surface faces and 422,614 grid cells. The normal spacing at the wall was selected to give a y^+ value of 4 at a Reynolds number of 11.7 million based on the mean aerodynamic chord length. A geometric stretching was used to extrude the surface mesh across a viscous layer thickness which corresponds to a y^+ value of 800. As seen in Figure 67, there is a large discontinuity in grid spacing between the edge of the extruded and tetrahedral grids. Extending the extruded region further into the field would reduce the jump in grid spacing, unfortunately, attempts to generate a grid with a thicker viscous layer resulted in crossed faces in the volume grid. Several unsuccessful attempts were made to eliminate the crossed faces by re-meshing the surface grid, and smoothing the surface normals.

Attempts were made to run Cobalt on grid tv1 at run conditions of Mach 0.7, 0.04 degrees

angle of attack, and Mach 0.84, 5.06 degrees angle of attack and Reynolds number of 11.7 million. The Spalart turbulence model was used in all solutions. The solution at 0.04 degrees angle of attack was run first-order for 4,000 iterations and second-order for 22,000 iterations at a CFL number of 0.8. The convergence history is shown in Figure 68. The drag converges for the first 10,000 iterations and then begins to oscillate. The cause for this lack of convergence is not known but probably is a consequence of the poor grid quality. The solution required 58.7 hours of CPU time and 60.9 million words of memory on a CRAY C90 processor. Spanwise cuts of the surface pressure from this solution are compared with experimental data in Figure 69. The comparison is relatively good with the exception of the leading edge region of the outboard cuts. The poor comparison in this region may be due to several factors including, lack of convergence, lack of grid resolution in the outer portion of the boundary layer and/or poor grid quality. The integrated forces from this solution are shown in Table 5. We were unable to get Cobalt to converge at 5.06 degrees angle of attack. Attempts were made to run Cobalt on grid vv1, a tetrahedral viscous packed grid created by the VGRID grid generator. This solution would have provided equitable comparisons between the Cobalt and USM3D flow solvers on the same grid. Unfortunately, we have been unable to get a Cobalt solution to converge on this grid.
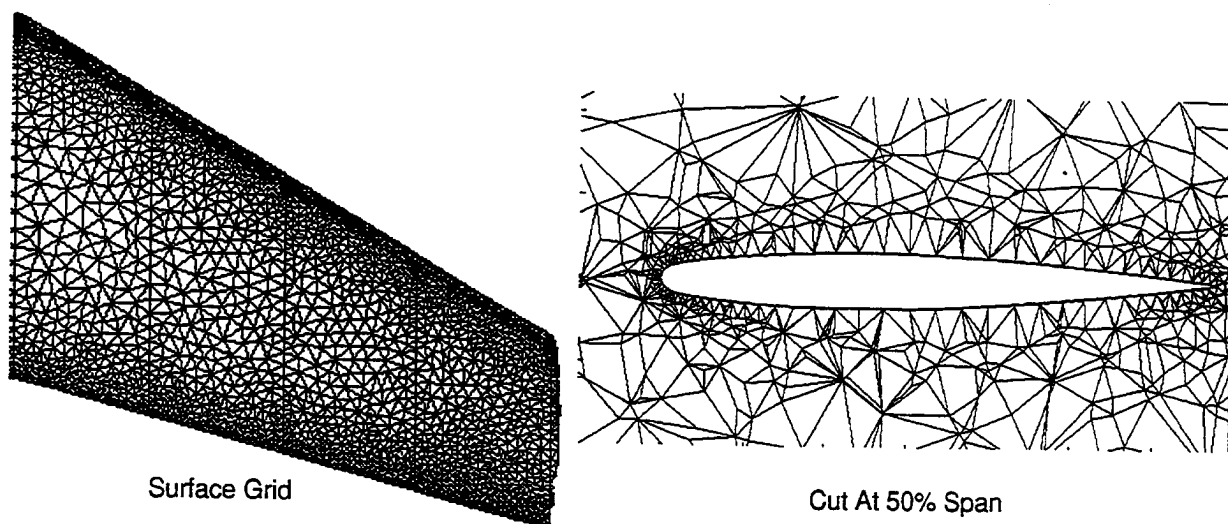

Surface Grid

Cut At 50% Span

Figure 67.   Surface and cut through volume of viscous packed TETMESH generated grid about ONERA M6 wing (grid tv1).
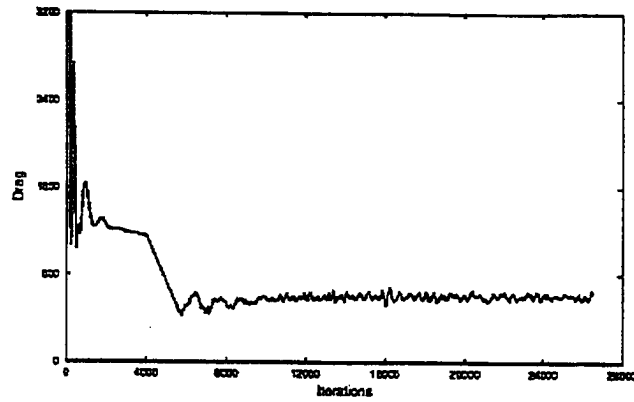
43

Figure 68. Cobalt solution convergence history for ONERA M6 wing (Mach 0.7, α=0.04 degrees, Re_c = 11.7 million, grid tv1).
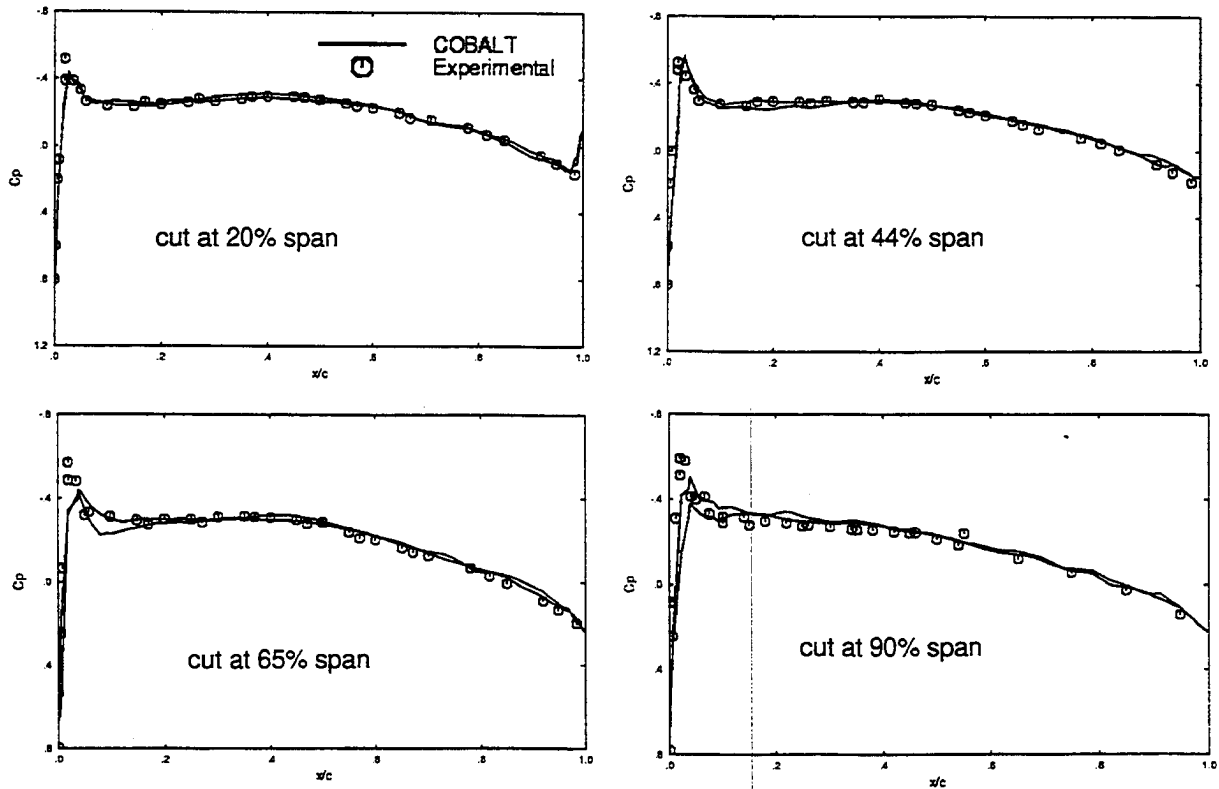

Figure 69. Cobalt predicted surface pressure coefficient at 4 spanwise cuts of ONERA M6 wing (Mach 0.7, α=0.04 degrees, Re_c = 11.7 million, grid tv1).

44

4.3 NASTD/MACGS Results

A total of 3 NASTD viscous solutions were computed on 1 MACGS generated grid (mv1). For comparison purposes, an Euler solution was also computed on grid ne1.

A multi-zone hybrid viscous packed grid was generated in MACGS. The surface and symmetry plane resolution are shown in Figure 70. This grid contains 3264 surface faces, 73,008 hexahedral volume cells, 293,265 tetrahedral volume cells, and 138,148 grid nodes. The interface between the structured and unstructured grids is non-point matched. The resolution of the unstructured surface mesh at the zonal interface was selected to minimize the jump in grid spacing between the structured and unstructured meshes. The grid spacing normal to the surface was selected to give a y^+ of 4 at a Reynolds number of 11.7 million. Care was taken to place the zone boundary between the structured hexahedral grid and the unstructured tetrahedral grid far enough away from the geometry to be outside of the viscous dominated region of the flow.

NASTD solutions were generated on grid mv1 at flow conditions of Mach 0.84, 0.04 degrees angle of attack, Reynolds number of 11.7 million, and Mach 0.7, 5.06 degrees angle of attack, and Reynolds number of 11.7 million. Turbulence was modeled using the Spalart/Allmaras (SA) turbulence model.

The convergence history of the 0.04 degree angle of attack case is shown in Figure 71. The solution was run for 12,000 iterations at a CFL number of 1.2 although convergence was achieved in roughly 6,000 iterations. The solution required 169.9 hours of CPU time for 12,000 iterations on an HP735 workstation (equivalent to 48.5 CRAY C-90 hours) and 4.9 million words of memory. Spanwise cuts of the predicted wing surface pressure for the 0.04 degree angle of attack case are compared with experimental data in Figure 72. The surface pressures agree well with the experimental data with the exception of the lower surface leading edge in the 65% span cut. The reason for this discrepancy is not known. The integrated lift and drag from this solution are presented in Table 5.

Surface flow patterns from the NASTD solution for the 5.06 degree angle of attack case are shown in Figure 73. These patterns reveal a substantial shock-induced separation on the outboard portion of the wing. Spanwise cuts of the wing surface pressure are compared with experimental data in Figure 74. The surface pressures agree very well with the experimental data. The predicted shock location matches the experimental data indicating that the location and magnitude of the separation is well predicted. There is some discrepancy between the NASTD solution and the experimental data just aft of the separation line. This may be due to the turbulence model.

To investigate the effects of the turbulence model choice, the 5.06 degree angle of attack case was recomputed in NASTD using the SST turbulence model (5). This turbulence model is a two-equation k-ω turbulence model. The convergence of this solution was similar to the Spalart Allmaras turbulence model solution, however, the solution time per iteration was lower due to fewer sub-iterations required by the turbulence model. The predicted surface pressure from this solution is compared with the Spalart turbulence model solution and experimental data in Figure 75. The two-equation turbulence model appears to have only minor effects on the solution. Most of the differences are in the separation region where the two-equation model solution is marginally better.
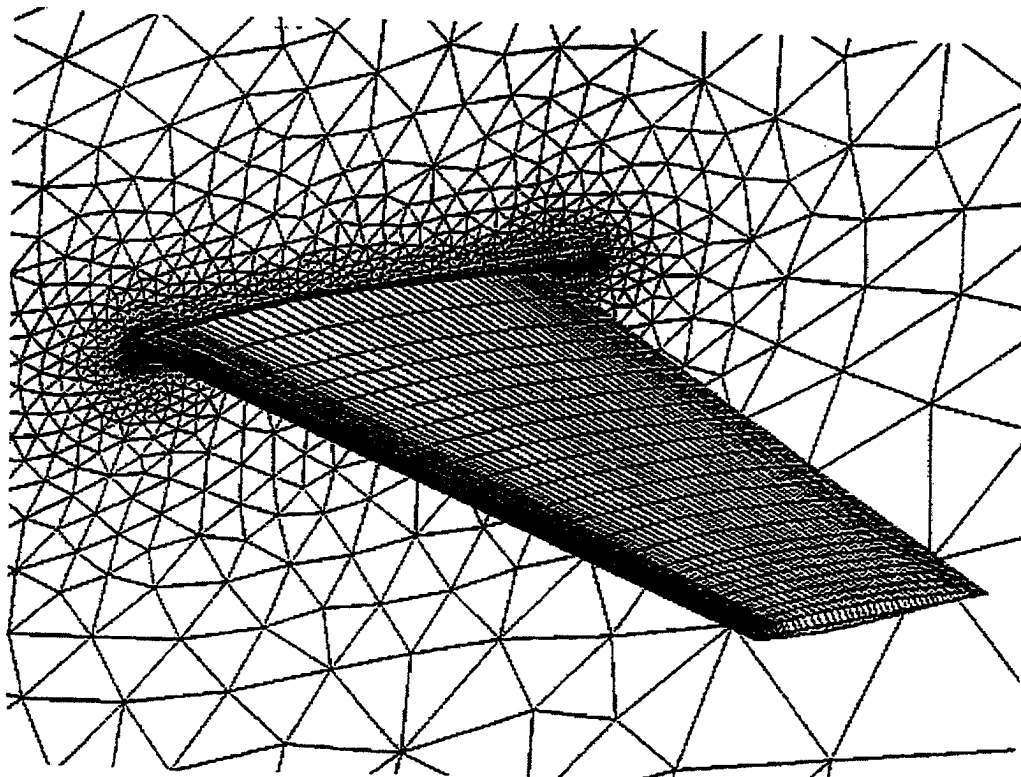
45

Figure 70. Mesh on surface and symmetry plane of MACGS generated hybrid grid about the ONERA M6 wing (grid mv1).
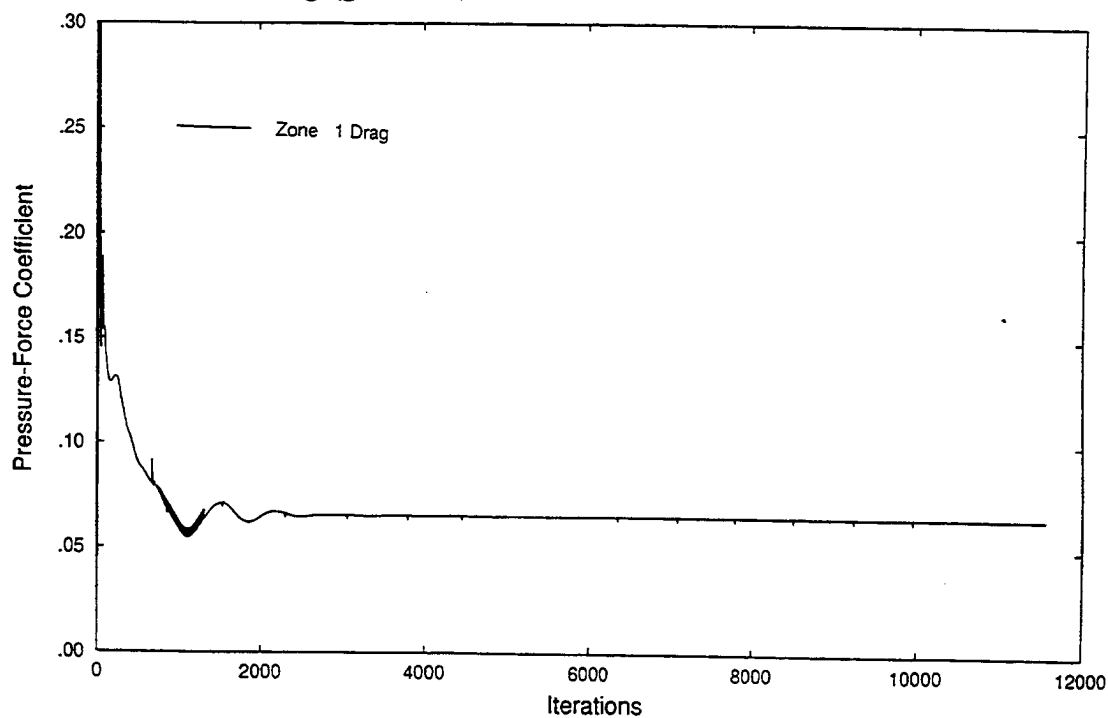

Figure 71. NASTD solution convergence history for ONERA M6 wing (Mach 0.7, α=0.04 degrees, Re_c = 11.7 million, grid mv1).
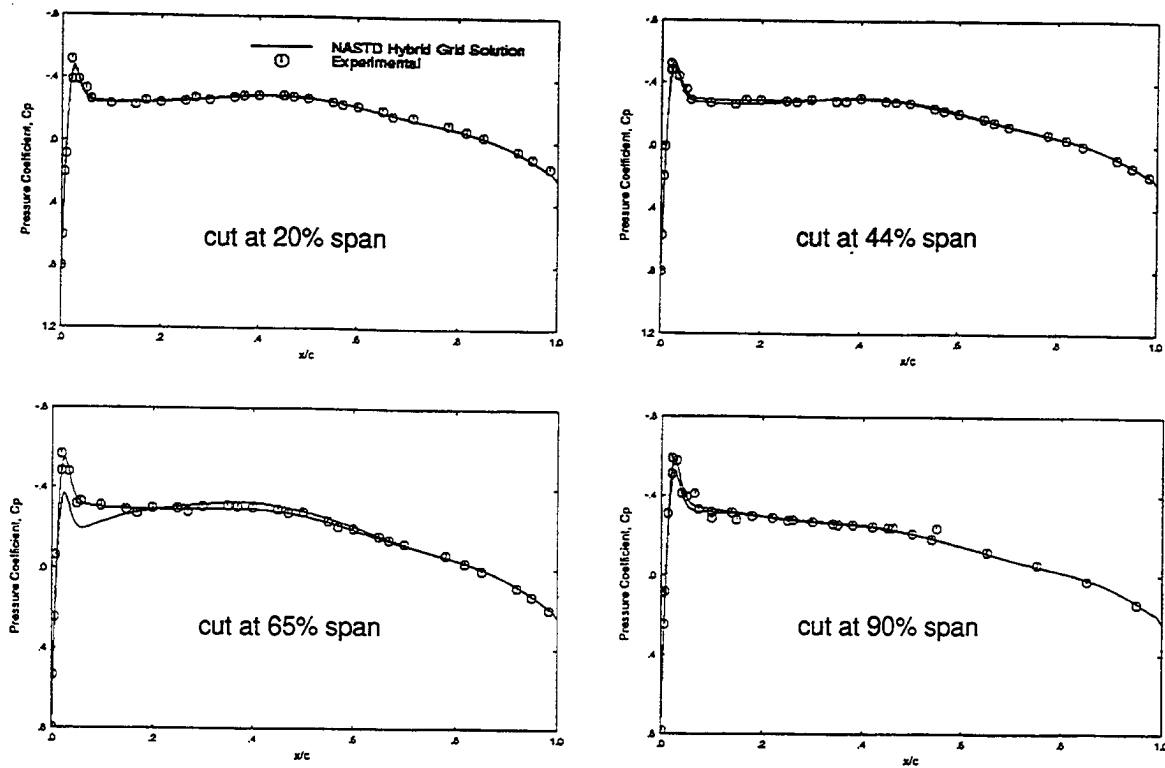
46

Figure 72. NASTD predicted surface pressure coefficient at 4 spanwise cuts of ONERA M6 wing (Mach 0.7, α=0.04 degrees, Re_c = 11.7 million, grid mv1).
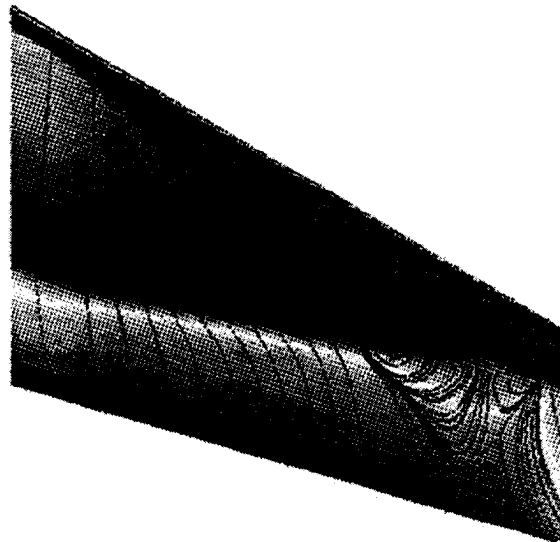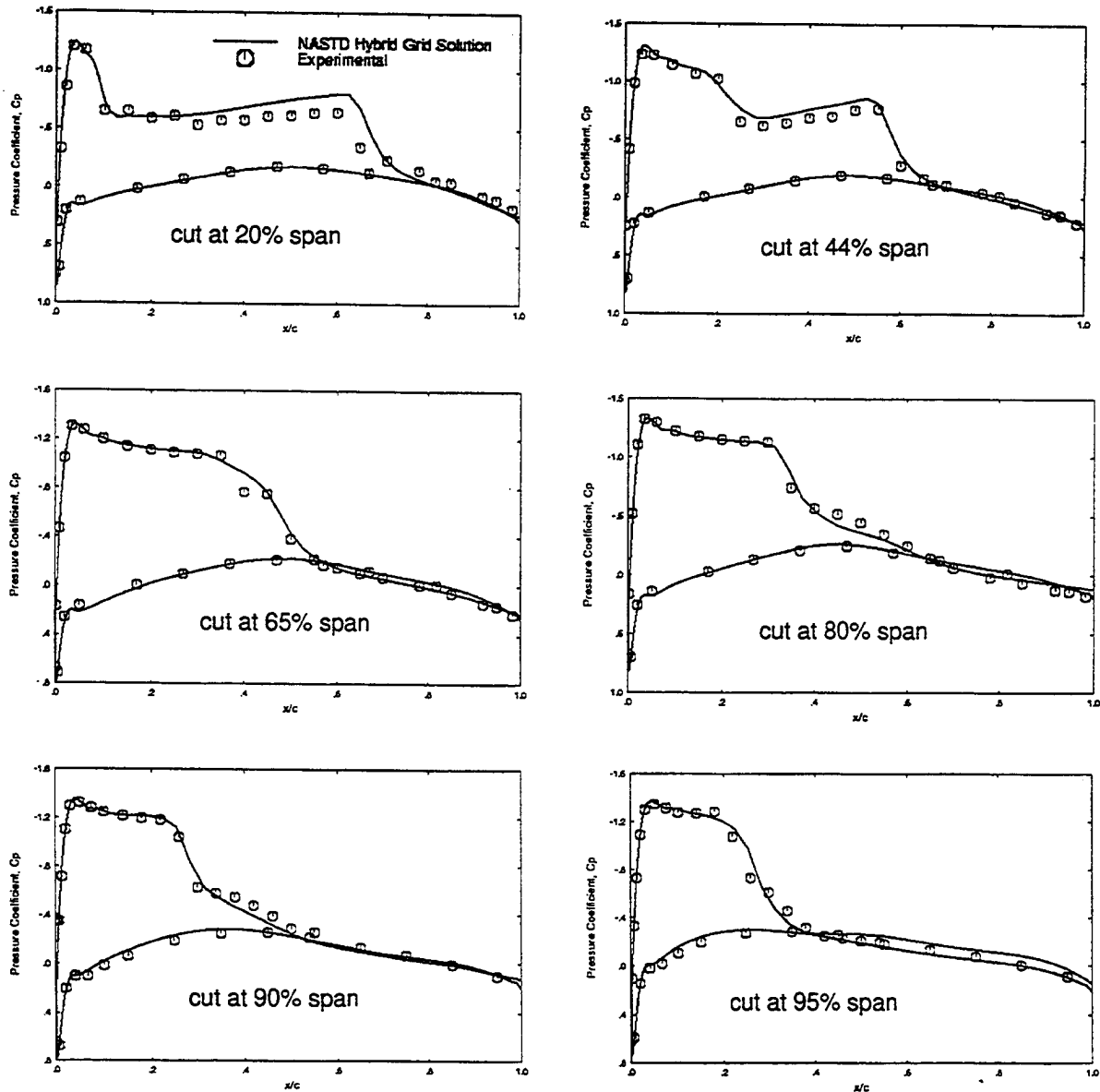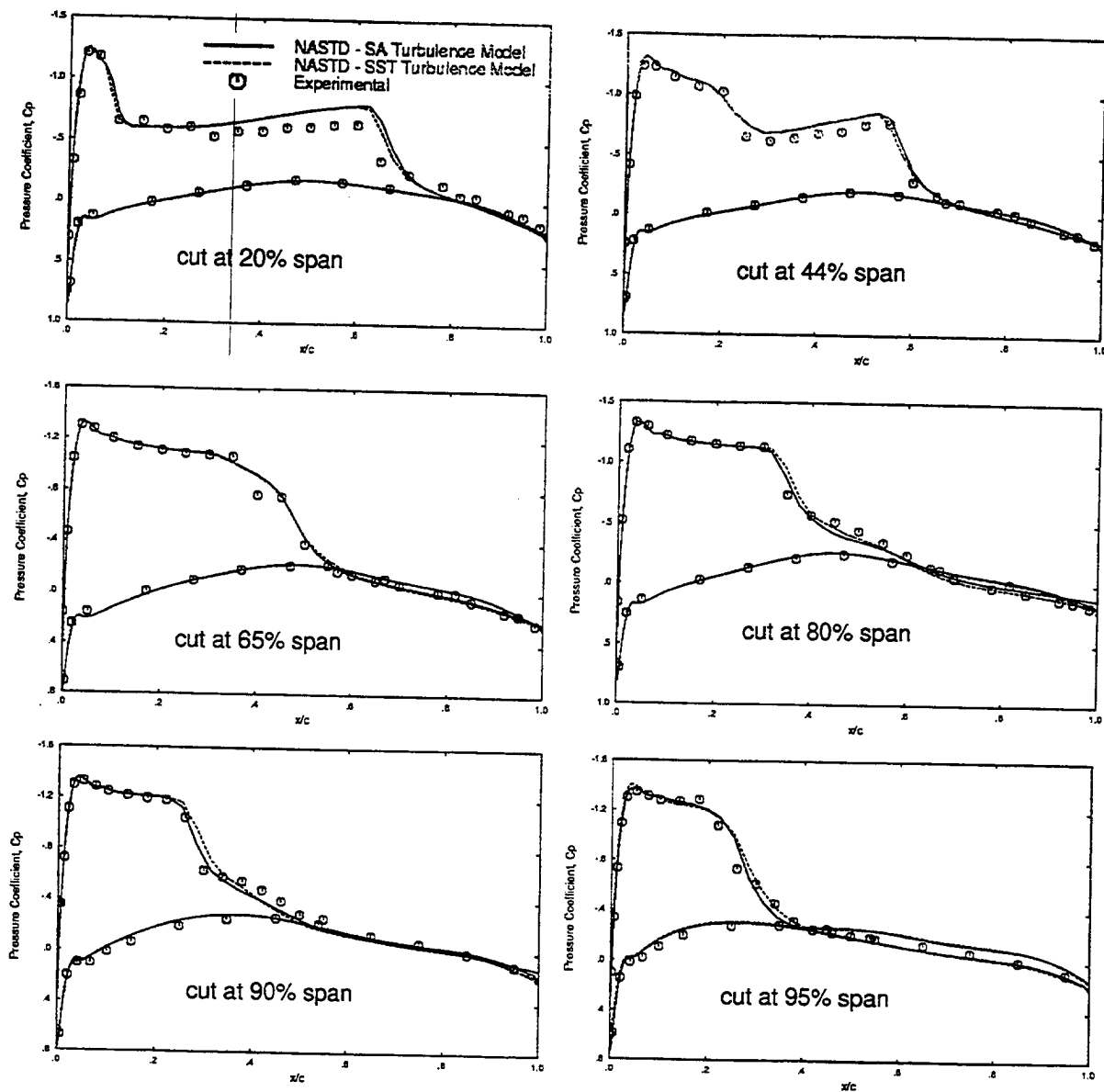

Figure 73. NASTD predicted particle traces confined to surface of ONERA M6 wing (Mach 0.84, α=5.06 degrees, Re_c=11.7 million, grid mv1).

Figure 74. NASTD predicted surface pressure coefficient at 6 spanwise cuts of ONERA M6 wing (Mach 0.84, α=5.06 degrees, Re_c = 11.7 million, grid mv1).

Figure 75.   Effect of turbulence model on NASTD predicted surface pressure coefficient for ONERA M6 wing (Mach 0.84, α=5.06 degrees, Re_c = 11.7 million, grid mv1).

4.4 USM3D/VGRID Results

A total of 3 USM3D viscous solutions were computed on 2 VGRID generated grids. For comparison purposes, an Euler solution was also computed on grid ne1. The viscous USM3D computations were performed on two existing grids, vv1 and vv2. A summary of the grid characteristics for each grid is presented in Table 4. The surface grid and symmetry plane of grids vv1 and vv2 are shown in Figure 76. The surface mesh is the same for both grids and is

stretched anisotropically in the streamwise direction in order to reduce the overall grid size. The viscous layer merges smoothly into the inviscid grid with a minimal jump in grid spacing. The grid spacing of the first point normal to the wall results in a y^+ value of 80 for grid vv1 and 4 for grid vv2 at a Reynolds number of 11.7 million. The large y^+ value of grid vv1 necessitates the use of a wall function to model the near wall viscous effects while grid vv2 was used without a wall function.

Two solutions were run on grid vv1 using the Spalart/Allmaras turbulence model and a wall function. The solutions were run at flow conditions of Mach 0.847, Re=11.7 million and angles of attack of 0.04 and 5.06 degrees. The 0.04 degree angle of attack case was run for 3600 iterations at a CFL number of 200. The solution required 29.4 hours of CPU time and 63.4 million words of memory on a CRAY C-90 processor. Spanwise cuts of the predicted wing surface pressure for the 0.04 degree angle of attack case are compared with experimental data in Figure 77. The surface pressures agree well with the experimental data. The integrated lift and drag from this solution are presented in Table 5.

Surface flow patterns from the USM3D solution for the 5.06 degree angle of attack case are shown in Figure 78. As with the NASTD solution, a large separation region is predicted on the outboard portion of the wing, however, the size and location of this separation are different. Spanwise cuts of the wing surface pressure are compared with experimental data in Figure 79. The solution at cuts inboard of the separation agree well with the experimental data, however, the solution at the cuts outboard of the separation show that the separation location is predicted too far forward. This may be due to the use of a wall function at a separated flow condition.

The effect of the wall function on the solution was investigated by computing a full viscous (no wall function) USM3D solution on grid vv2. The surface flow patterns from this solution are shown in Figure 80 and the predicted surface pressure is shown in Figure 81. Once again the surface flow traces indicate a substantial shock induced separation on the outboard portion of the wing. Without the wall function, the surface pressure agrees much closer with the experimental data at the outboard cut locations.

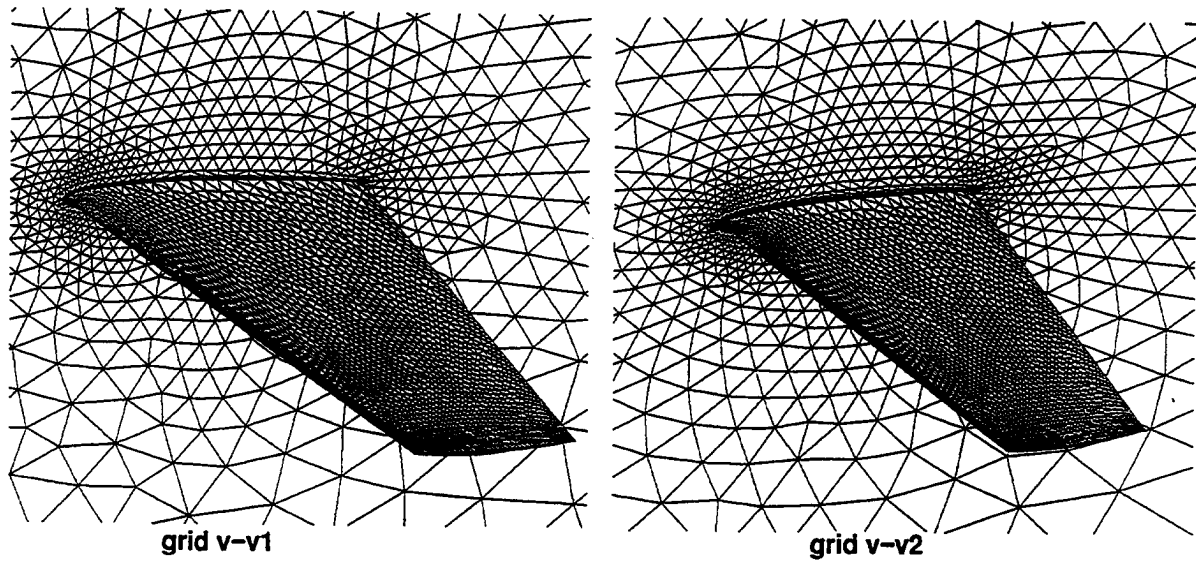**grid v–v1**   **grid v–v2**

Figure 76.   Mesh on surface and symmetry plane of two VGRID generated tetrahedral grids
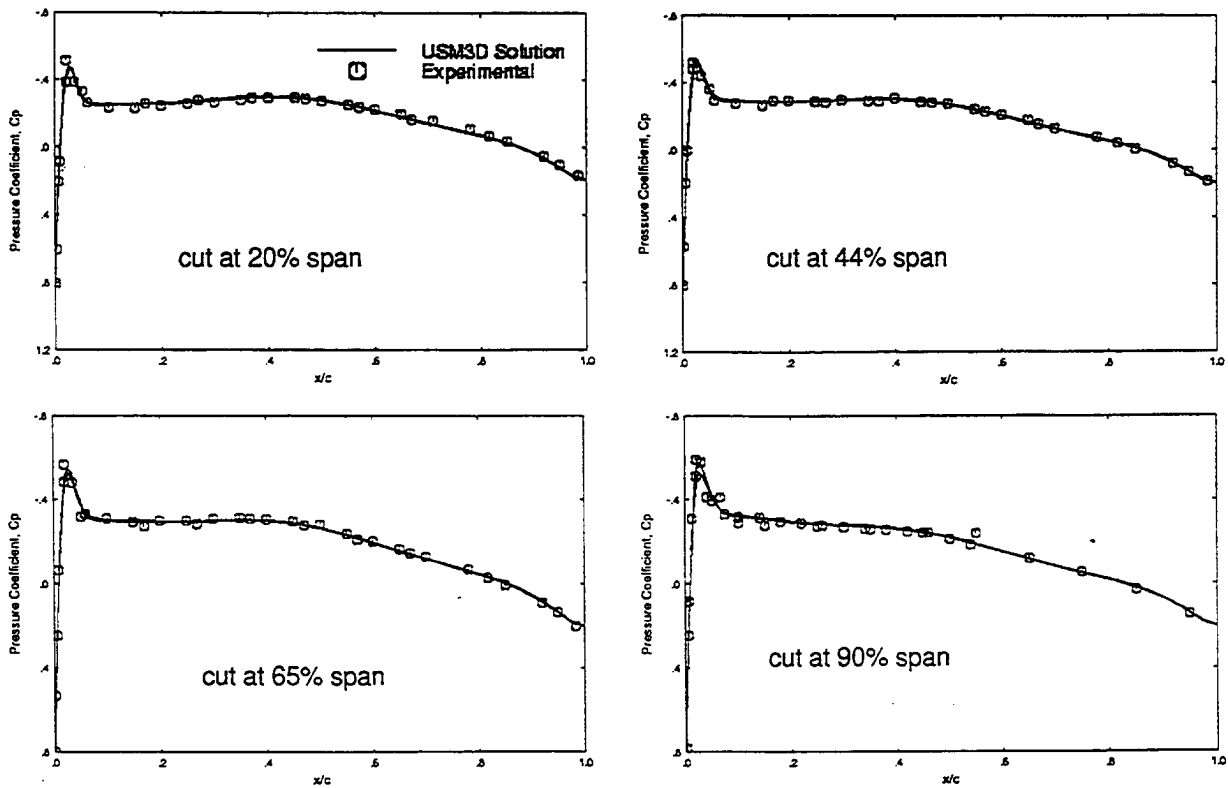about the ONERA M6 wing (grids vv1 and vv2).

Figure 77.   USM3D predicted surface pressure coefficient at 4 spanwise cuts of ONERA M6
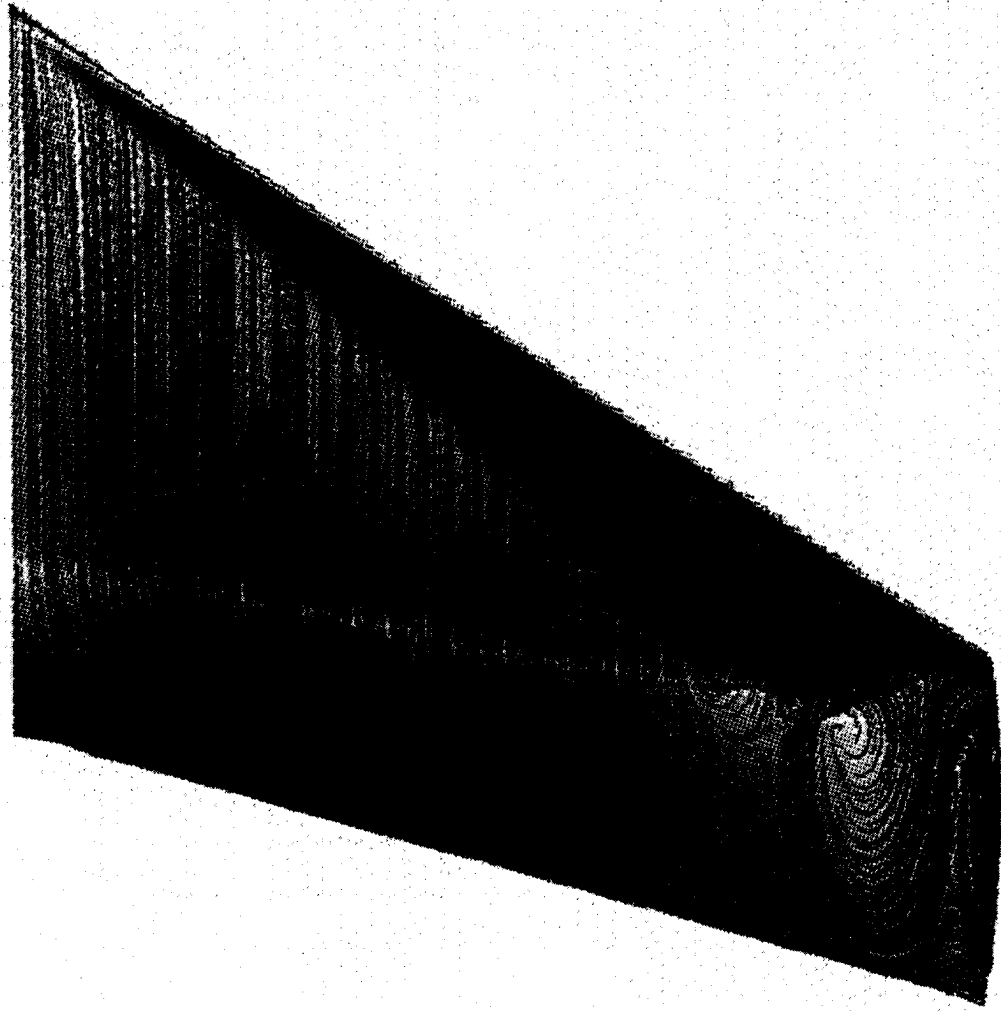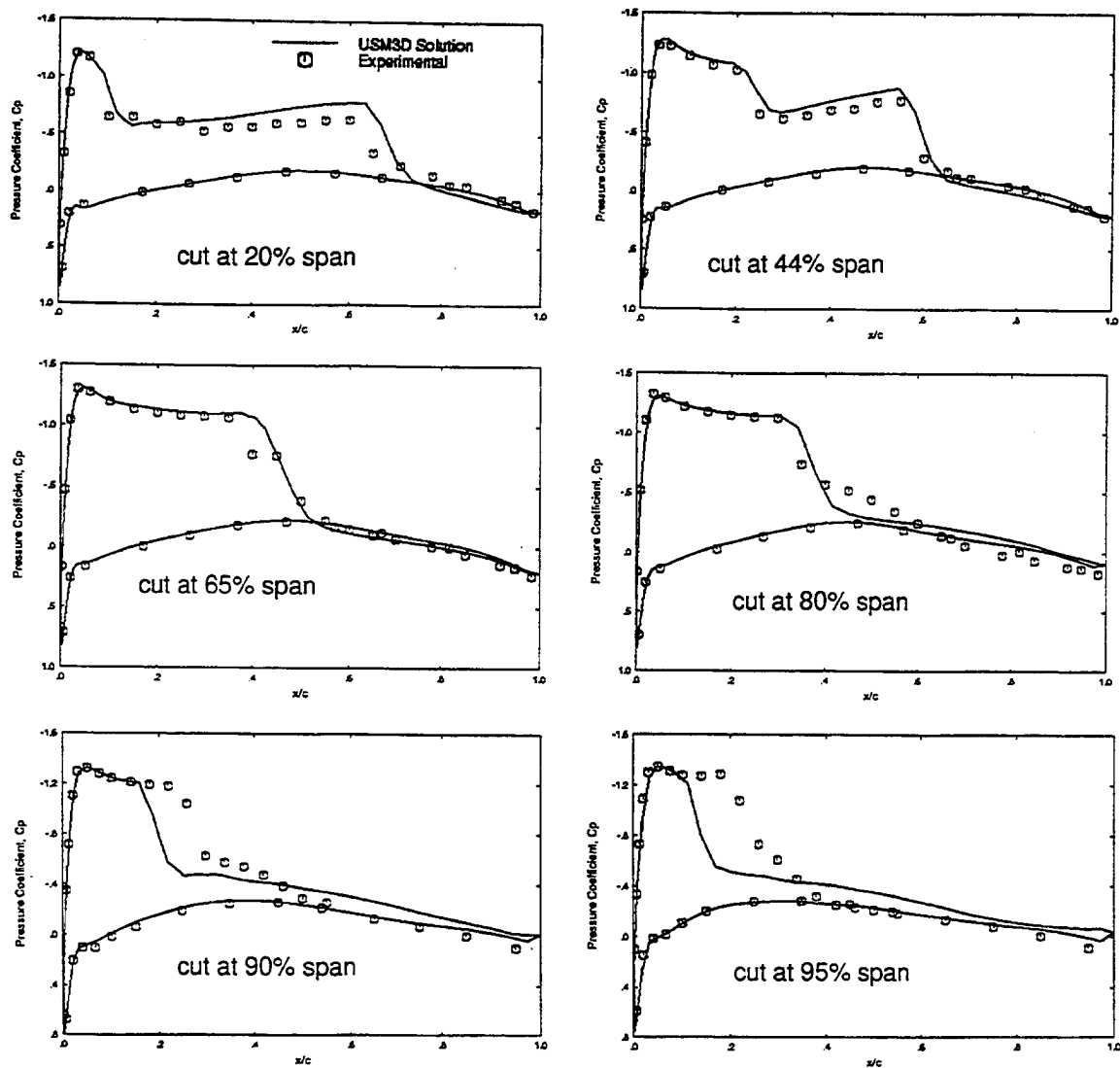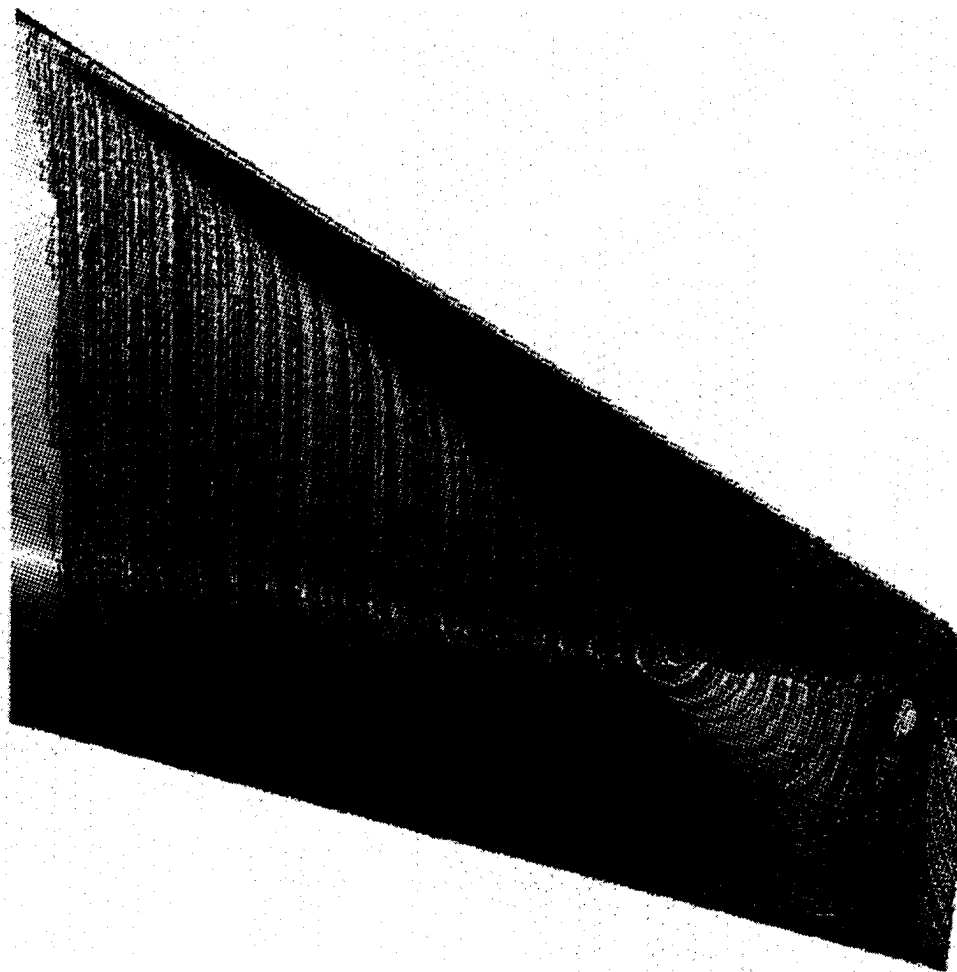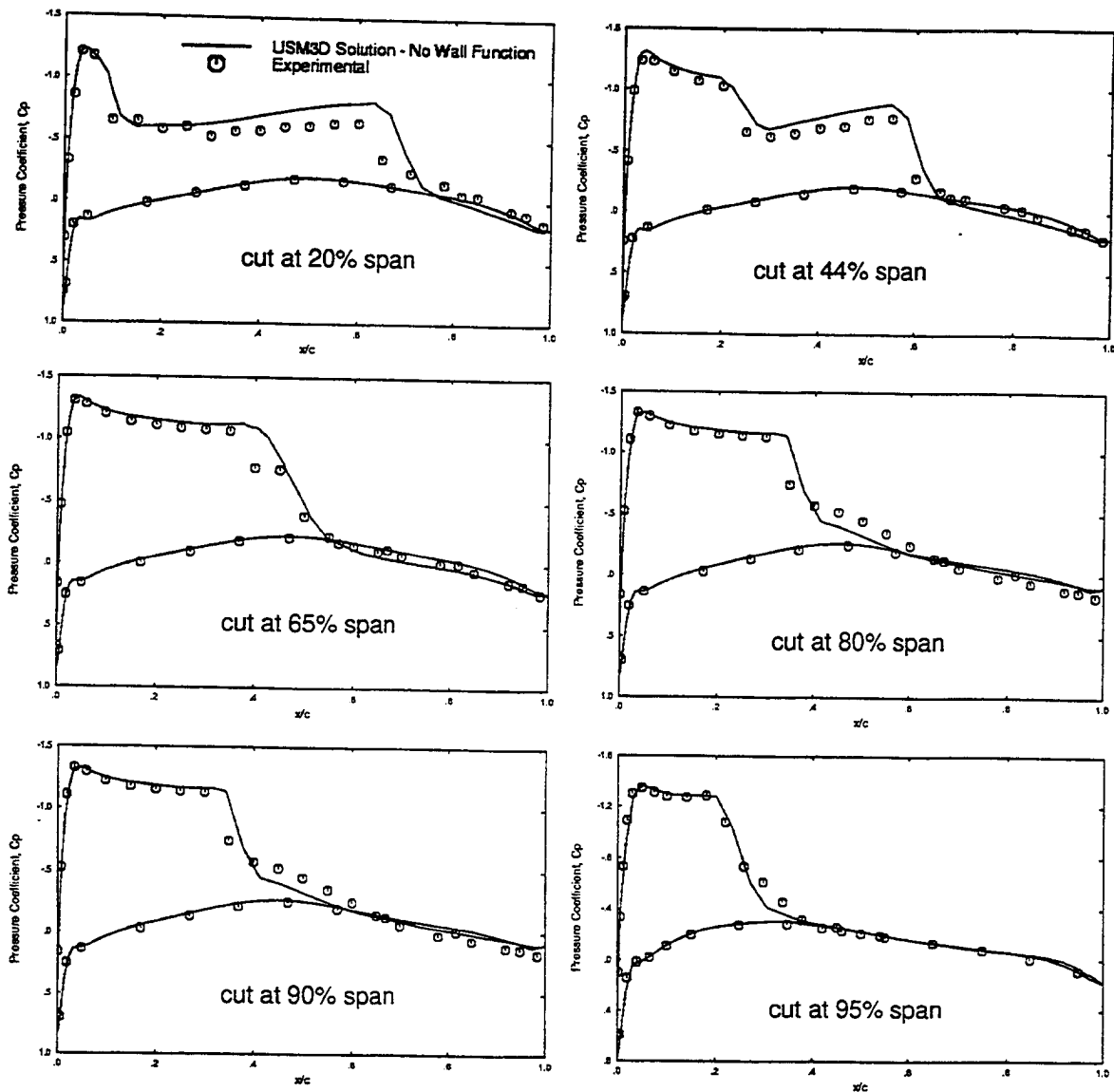wing (Mach 0.7, α=0.04 degrees, Re_c = 11.7 million, grid vv1).

51

Figure 78.   USM3D predicted particle traces confined to surface of ONERA M6 wing (Mach
0.84, α=5.06 degrees, Re$_c$=11.7 million, grid vv1).

Figure 79. USM3D predicted surface pressure coefficient at 6 spanwise cuts of ONERA M6 wing (Mach 0.84, α=5.06 degrees, Re_c = 11.7 million, grid vv1).

Figure 80. USM3D predicted particle traces confined to surface of ONERA M6 wing (Mach 0.84, α=5.06 degrees, Re$_c$=11.7 million, grid vv2).

Figure 81.   USM3D predicted surface pressure coefficient at 6 spanwise cuts of ONERA M6
wing (Mach 0.84, α=5.06 degrees, Re_c = 11.7 million, grid vv2).

4.5 Flow Solver Comparisons

In this section the efficiency and accuracy of the ONERA wing flow solutions from the three methods are compared. A summary of all ONERA wing flow solutions generated during this study is given in Table 5.

Table 5. ONERA Wing Run Matrix

Flow Solver	Grid	Mach	Angle of Attack	Re x 10^{-6}	Turb Model	iter	C90 CPU seconds /iter	memory req. MW	C_L pres	C_L visc	C_L tot	C_D pres	C_D visc	C_D tot
Cobalt	ne1	0.84	3.06	N/A	Euler	44,000	2.90	30.1	.2784	N/A	.2784	.0147	N/A	.0147
Cobalt	te1	0.84	3.06	N/A	Euler	40,000	2.24	21.9	.2781	N/A	.2781	.0177	N/A	.0177
Cobalt	te2	0.84	3.06	N/A	Euler	38,000	3.11	31.9	.2832	N/A	.2832	.0181	N/A	.0181
Cobalt	tv1	0.7	0.04	11.7	Spalart	26,500	7.97	60.9	.0050	0.000	.0050	.0103	.0035	.0138
Cobalt	tv1	0.84	3.06	11.7	Spalart	138,500	8.53	60.9	.5162	-.0001	.5161	.0446	.0054	.0500
Cobalt	vv2	0.84	5.06	11.7	Spalart		9.20	60.9						
USM3D	ne1	0.84	3.06	N/A	Euler	1,000	6.61	41.2	.2878	N/A	.2878	.0121	N/A	.0121
USM3D	vv1	0.7	0.04	11.7	Spalart/wf	3,600	29.39	63.4	.0036	-.0000	.0036	.0018	.0053	.0071
USM3D	vv1	0.84	5.06	11.7	Spalart/wf	3,100	29.44	63.4	.4447	-.0002	.4445	.0376	.0047	.0422
USM3D	vv2	0.84	5.06	11.7	Spalart	8,250	20.34	98.2	.4609	.0003	.4612	.0371	-.0034	.0337
NASTD	ne1	0.84	3.06	N/A	Euler	5,000	1.69*	3.5	.2876	N/A	.2876	.0131	N/A	.0131
NASTD	mv1	0.7	0.04	11.7	Spalart	9,839	17.76*	4.9	.0102	.0000	.0102	.0073	.0296	.0369
NASTD	mv1	0.84	5.06	11.7	Spalart	11,550	19.68*	4.9	.4529	-.0004	.4525	.0361	.0077	.0438
NASTD	mv1	0.84	5.06	11.7	SST	11,550	17.33*	5.7	.4493	-.0004	.4489	.0349	.0077	.0426

* Estimated based on ratio of 3.5 HP-735 CPU seconds to 1 CRAY C-90 CPU second.

The different grid topologies used with each flow solver for viscous computations precludes an equitable one-to-one comparison of flow solver accuracy and efficiency independent of the grid. However, such a comparison can be made for inviscid flow since each of the three methods can compute Euler solutions on tetrahedral grids. For this purpose, Euler solutions were computed with all three methods on grid ne1 at run conditions of Mach 0.84, and 3.06 degrees angle of attack. In Figure 82, the predicted surface pressure from the three methods is compared with experimental data. All three solutions agree relatively well with the experimental data. The Cobalt solution appears to be marginally better than the other two methods particularly near the suction peaks. However, the Cobalt solution also had the longest computer run time of the three methods. The memory and CPU requirements for each of the three methods are tabulated in Table 5. Both USM3D and Cobalt are cell centered methods and require approximately 600% more memory than the nodal based algorithm used in NASTD. The CPU requirements of Cobalt were significantly larger than USM3D and NASTD primarily due to the large number of iterations required to reach convergence. NASTD required the least amount of CPU of the three methods most likely due to the lower amount of work required by the nodal based scheme.

The results, obtained on the ONERA wing at Mach 0.84, Re=11.7 million, and 0.04 degrees angle of attack, provide the opportunity to compare the viscus prediction capability of the flow solvers in the absence of any flow separation. The predicted surface pressures from each of the methods is compared with the experimental data in Figure 83. Without any flow separation each of the three methods does a fairly good job of predicting the surface pressures.

The Cobalt solution is the worst of the three probably due to the poor grid quality. The integrated drag from each of the three methods is shown in Table 5. The predicted pressure drag from the 3 methods ranges from 0.0018 to 0.0103. Likewise the skin friction drag varies from .0035 to 0.0296. Unfortunately, without running the flow solvers on the same grid it is impossible to determine if this discrepancy is due to grid differences or to differences in the flow solver algorithms. The memory requirements of USM3D and Cobalt were similar at 60.9 MW for Cobalt and 63.4 MW for USM3D. The NASTD memory requirements were much lower at 4.9 MW. This is due to several factors including more efficient storage of structured grid data, nodal based scheme, and multi-zone. The run times for NASTD (after 6,000 iterations) and USM3D were roughly equivalent at 103.6 HP CPU hours (equivalent to 29.6 CRAY C-90 CPU hours) and 29.39 hours of CRAY C-90 CPU time. The run time for Cobalt was almost twice as long at 58.67 CRAY CPU hours.

The second set of run conditions, Mach 0.84, Re=11.7 million, 5.06 degrees angle of attack, provides a comparison of the different methods in a turbulent separated flow. In Figure 84, spanwise cuts of the predicted surface pressure from the NASTD and USM3D (without wall function) solutions are compared with experimental data. Considering the complexity of the flowfield, both solutions agree remarkably well with the experimental data. The NASTD results predict the shock boundary layer interaction slightly better showing slightly more smearing across the shock than the USM3D results. The NASTD results also match the experimental data slightly better in the separated regions of the flowfield. These differences could be due to the different grid resolutions of the two solutions. USM3D required 98.2 MW of memory compared to 5.7 MW for NASTD. The run times of the two methods were 46.6 CRAY C-90 CPU hours for USM3D and 220.99 HP 735 CPU hours (equivalent to 63.14 CRAY C-90 CPU hours) for NASTD.
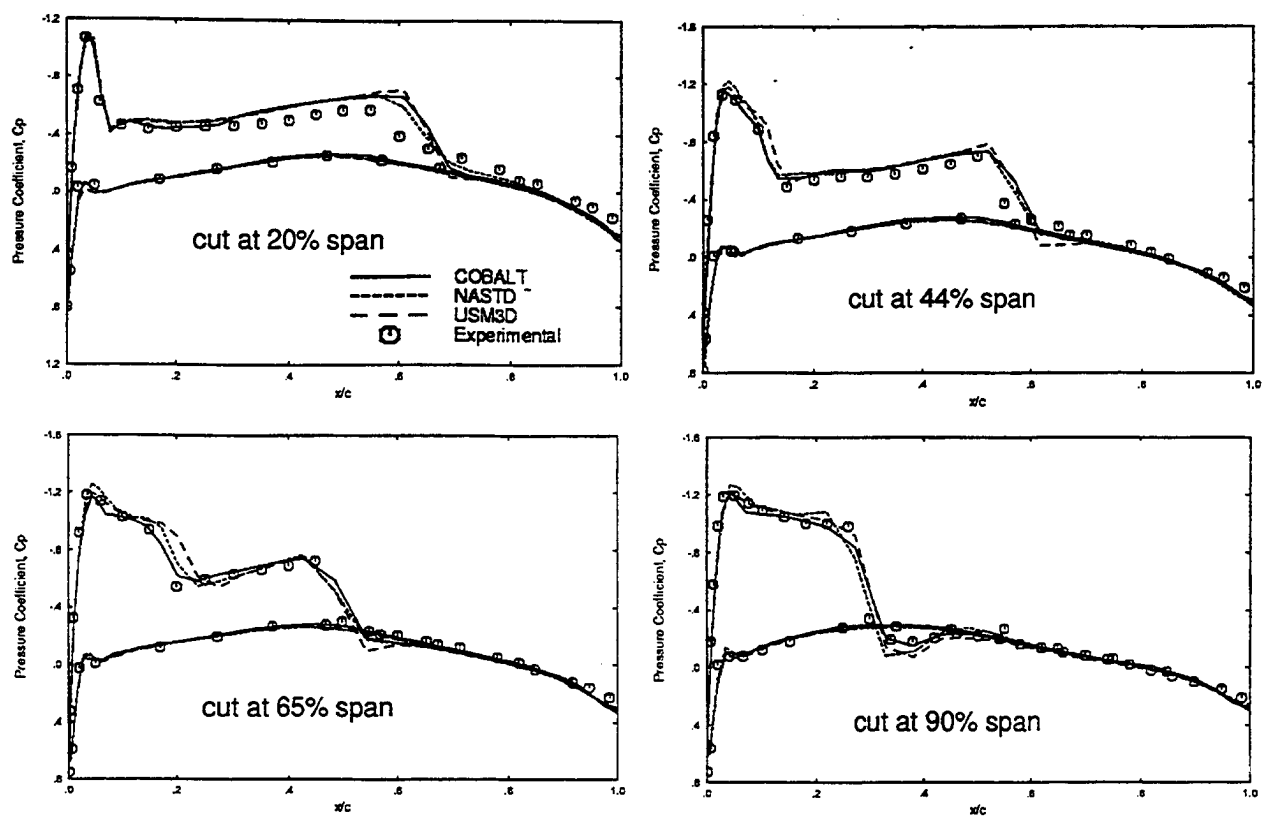
Figure 82.   Comparison of Euler flow solutions on ONERA M6 wing (Mach 0.84, α=3.04
degrees, Euler, grid ne1).
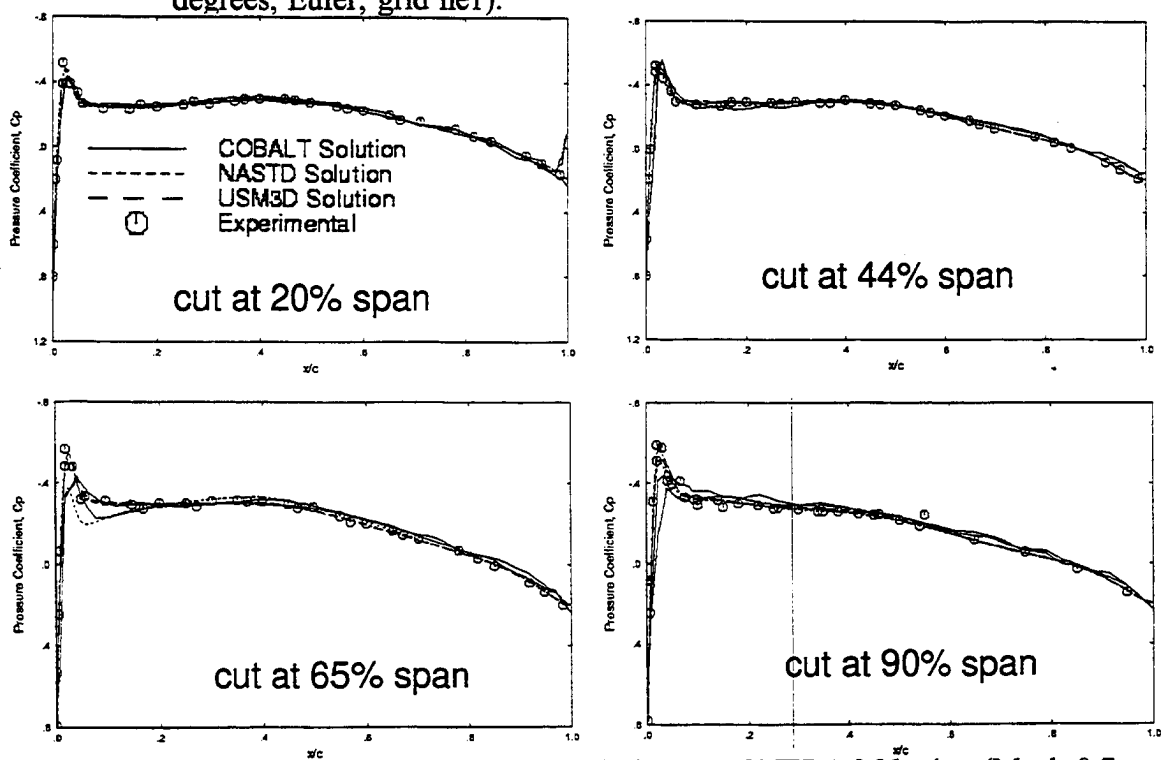
Figure 83.   Comparison of Navier-Stokes solutions on ONERA M6 wing (Mach 0.7, α=0.04
degrees, Re_c=11.7 million)
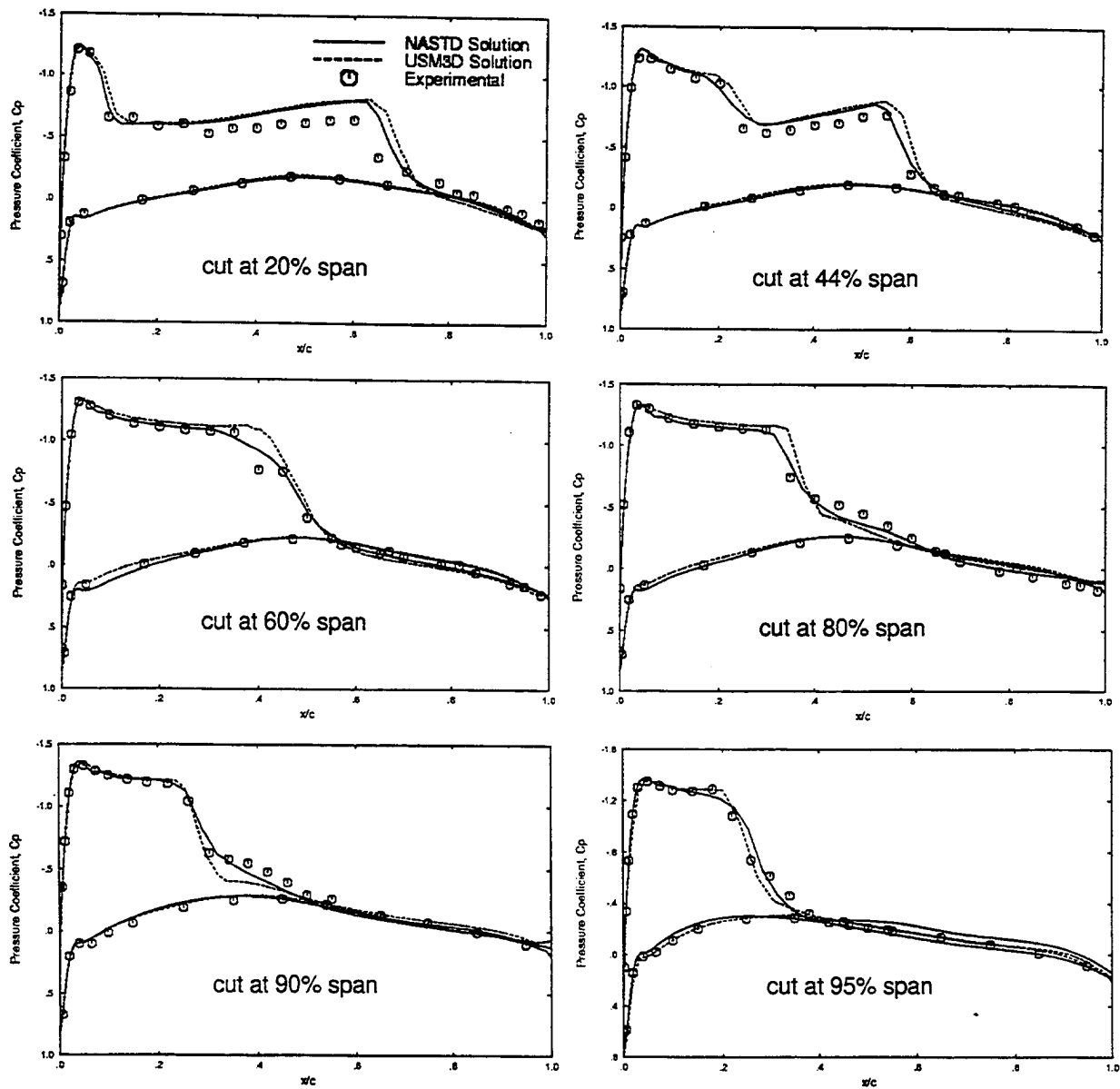
Figure 84.   Comparison of Navier-Stokes solutions on ONERA M6 wing (Mach 0.84, α=5.06 degrees, Re$_c$=11.7 million)

5. METHOD ASSESSMENT

5.1 Accuracy

A direct comparison of the relative accuracy of the three methods evaluated in this study is not possible since each method utilizes a different grid cell topology. The one direct comparison that was made, an Euler solution on the ONERA wing, did not show significant differences in the accuracy of the three methods. There was some variation in the accuracy of the three methods for viscous computations. The accuracy of Cobalt and NASTD was very similar for flat plates with Cobalt having slightly higher accuracy. The USM3D solutions without the wall function were the worst of the three methods. However, the USM3D solutions with a wall function offered the best accuracy. These results are inconsistent with previous results generated by the code author (1). Further study is required to determine the cause of this discrepancy.

All of the viscous unstructured grid methods evaluated in this report have the ability to provide accuracy approaching that of existing structured grid CFD methods provided adequate grid resolution and quality is employed. However, unstructured grid resolution and quality requirements are less well known than for structured grids adding an element of risk to the solution. The grid requirement guidelines developed in this report provides a starting point for the grid developer. Additional grid requirements for other grid types and mixtures of grid types need to be developed. In addition the effects of grid cell shape on solution accuracy for each flow solver need to be identified. Once these attributes are known, mixed cell grids such as those utilized by TETMESH/Cobalt should provide much better control over grid quality yielding a distinct advantage over the tetrahedral type grids.

The aspect of grid quality was not explored in this study but can have a substantial effect on the solution accuracy. Guidelines need to be developed to aid the end user in assessing the quality of the grid. This is particularly important for unstructured grids since it is almost impossible to asses the grid quality visually. These guidelines should eventually be used in concert with an unstructured grid adaptation method to remove the burden of grid quality assessment from the user by automatically assuring the grid meets the quality and resolution guidelines.

5.2 Efficiency

A large variation in flow solver efficiency was identified in this study. This was primarily a consequence of the different time integration and discretization schemes used by each method. Implicit time integration was found to be necessary for adequate solution convergence. The explicit time integration scheme in Cobalt was found to be unacceptably slow for viscous dominated flows since the low CFL numbers severely limited the convergence rate in the boundary layer. The implicit schemes used in NASTD and USM3D provided much better convergence. The point Jacobi implicit scheme in USM3D provided the fastest convergence of the three methods at the expense of more memory usage.

The memory requirements of Cobalt and USM3D were both very large primarily due to their unstructured data structures and the use of cell based schemes. USM3D has the largest memory requirements of the three methods. NASTD utilized memory much more efficiently

through the use of structured data structures in the viscous layer and a nodal based scheme. Future use of these methods on complex geometries may be constrained by their memory usage. The Cobalt and USM3D ONERA wing solutions run in this study approached the memory limits of currently available machines.

The largest contributor to the cycle time of a CFD solution is in the grid development time. The unstructured grids used by these methods offer the potential to drastically reduce this time over existing structured grid methods. However, current unstructured grid generation systems will require a great deal of development before they can match the capability and ease of use of existing structured grid generation systems. MACGS provided the largest array of capabilities and ease of use of the grid generation tools evaluated in this study. Unfortunately this system relies on zonal hybrid grid technology. This technology reduces the efficiency of the grid generation process since separate structured and unstructured grid blocks must be developed around the geometry. The VGRID tool provided the fastest griding times from start to finish of the evaluated packages. The mixed cell grids used by TETMESH should provide the greatest flexibility to the grid developer and thereby the fastest grid generation times. Unfortunately this efficiency was not realized because of usability issues discussed below.

5.3 Ease of Use

One of the most important attributes of a CFD solution method is its ease of use. Ease of use is a subjective issue. The primary virtues that contributed to ease of use in this study included quick learning curve, documentation, robustness, abundance of useful features, and intuitiveness of the approach. We had a great deal of expertise with the MACGS/NASTD software package prior to this study. This biases our ability to make an impartial assessment of the ease of use of these packages. MACGS/NASTD are therefore not evaluated for ease of use in this study.

Surprisingly few difficulties were encountered during this study given the relative immaturity of the methods. The few problems that were encountered usually happened when working outside the environment for which the method had been previously tested by the developers. Two examples are running USM3D without a wall function and running Cobalt on tetrahedral viscous grids. Continued development of these solvers should improve their applicability to a wider range of problems. Learning to use each of the flow solvers was very straightforward. The Cobalt documentation was excellent and provided a complete description of all features. USM3D did not come with any documentation other than the comments in the Fortran source code. A users manual would be a more convenient aid to the new user. Both Cobalt and USM3D are relatively new software tools and therefore do not have the large number of features and capabilities such as multiple time and spatial numerical schemes, large selection of boundary conditions, dissipation operators, or parallel processing capability that can be found on more mature CFD solvers. As development of these packages continues the number of features will continue to grow.

The greatest obstacle to a new user of any of these methods is the large learning curve for the grid generation tools. All of the grid generation packages required several weeks of study to achieve a basic level of knowledge. Documentation when available aided in the learning process. However, all of the grid generation tools could use improvements to the documentation.

The GRIDTOOL/VGRID documentation provided a good description of GRIDTOOL but did not include any information on VGRID or POSTGRID. The TETMESH documentation was very sparse. A complete description of all of the features in TETMESH with examples of their use would aid the new user considerably.

Both the GRIDTOOL/VGRID and TETMESH packages are relatively immature and as such do not include a large array of features that are essential in the production CFD environment. Capabilities such as direct links to CAD packages, ability to modify/repair geometry, complete control of grid distributions on the surface and in space were noticeably missing. Both of these packages also will only run on Silicon Graphics workstations which limits their usefulness.

Of the two packages the GRIDTOOL/VGRID offered the most capability. Once the process was learned, the sequence of events to generate a grid in GRIDTOOL/VGRID was intuitive and relatively straight forward with the exception of the jumps required between the GRIDTOOL, VGRID, and POSTGRID software tools. The user has good control over the grid distribution through the specification of point and line sources. The quality of the resulting grids was found to be very good. A unique restart capability in VGRID allows very large grids to be developed on relatively small memory machines.

The TETMESH software uses a unique approach to generate grids containing a mixture of prismatic and tetrahedral cells. The TETMESH grid generation process is straight forward for tetrahedral grids. For extruded prismatic grids however, the process was not intuitive requiring a number of steps to be performed in a specific order. Without documentation or online help it was very difficult to determine the appropriate steps.

During the course of this study several limitations were encountered that made TETMESH very difficult to use. The user does not have adequate control over the grid distributions on the surface mesh and almost no control over the distribution of the volume mesh. Boundary conditions cannot be specified or changed on the surfaces once the grid has been generated. TETMESH was found to require a large amount of memory and there were several instances when the program bombed while generating a mesh. The surface extrusion capability does not work in conjunction with a symmetry plane requiring the entire geometry to be modeled thereby exacerbating the large memory usage problem. The surface extrusion capability is very fragile. Several items can cause the extrusion to fail including a convex geometry or poor surface mesh. The tools that are available to help with these problems, such as normal smoothing, did not seem to help in the problems we encountered.

6. CONCLUSIONS/RECOMMENDATIONS

A systematic assessment of the strengths and weaknesses of three viscous flowfield simulation methods for unstructured grids has been performed. The methods evaluated represent the primary viscous unstructured griding approaches currently in use including tetrahedral, zonal hybrid, and grids containing a mixture of tetrahedral and prismatic grids. The strengths and weaknesses of each method have been identified through a systematic study of the flowfields about a flat plate and ONERA M6 wing. Solutions were generated over a range of run conditions allowing comparisons of a wide variety of flow field features including transonic and separated flows. Each of the methods were evaluated based on their relative efficiency, accuracy, ease of use, and robustness. Predictions of skin friction, velocity profiles, and surface pressure with theoretical and experimental data were used to evaluate solution accuracy. Flow solver efficiency was evaluated by comparing memory and processor requirements of each method.

The different approaches used by each of the software packages resulted in a unique set of advantages over the other methods. The mixed cell unstructured grid used by Cobalt/TETMESH provides a great deal of flexibility which has the potential to reduce grid generation cycle time and improve solution quality through improved grid quality. The MACGS/NASTD software package was found to be the most efficient of the methods. The use of structured grid data structures and a nodal based scheme gave NASTD the lowest memory usage of the methods and solution run times about equal to USM3D and almost half that of Cobalt. USM3D utilized a point Jacobi integration scheme in conjunction with wall functions to provide the fastest run times of the three methods. The GRIDTOOL/VGRID grid generation package was the easiest to use of the grid generation systems and provided the fastest grid generation cycle time.

Each of the methods were found to provide adequate accuracy for engineering analysis provided adequate grid resolution and quality are employed. A set of grid resolution guidelines was developed for grid wall spacing and number of points in the boundary layer. Additional guidelines are needed to define required grid resolution and quality for specific types of flow fields. In addition grid adaptation techniques need to be developed to automatically ensure grid quality and resolution.

Several improvements can be made to improve the usability of these unstructured grid methods. The biggest roadblock to future use of these systems is in the grid generation systems. The primary focus of future development should therefore be in improving these systems by developing better documentation and improved ease of use. Future flow solver method developments should focus on reducing memory requirements and improving efficiency.

7. REFERENCES

1. Pirzadeh, S., "Progress Toward A User-Oriented Unstructured Viscous Grid Generator", AIAA Paper No. 96-0031, January 1996.

2. Frink, N. T., "Assessment of an Unstructured-Grid Method for Predicting 3-D Turbulent Viscous Flows", AIAA Paper No. 96-0292, January 1996.

3. White, Frank, *Viscous Fluid Flow*, McGraw-Hill, New York, 1974.

4. "Experimental Data Base for Computer Program Assessment", AGARD Report # AR-138, May 1979.

5. Menter, F.R., "Zonal Two Equation k-ϖ Turbulence Models for Aerodynamic Flows," AIAA-93-2906, July 1993.

APPENDICES

Appendix A: Cobalt Solution Convergence Plots
Cobalt Flat Plate Solutions, Mach 0.1, Re=1.77x10⁶, Laminar Flow
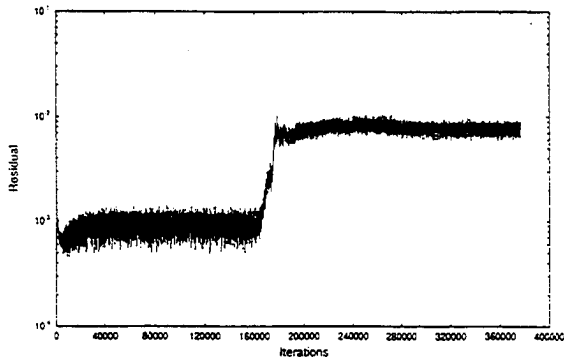
Figure A-1. Cobalt Residual History, Grid c-7
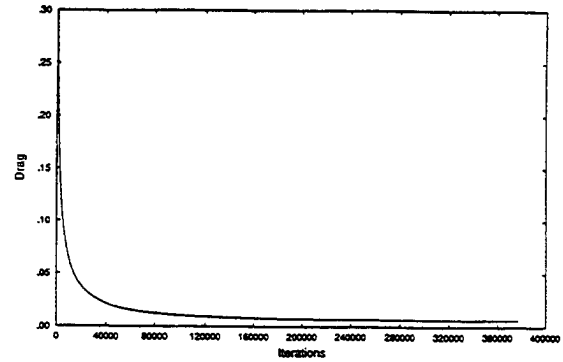
Figure A-2. Cobalt Force Convergence History, Grid c-7
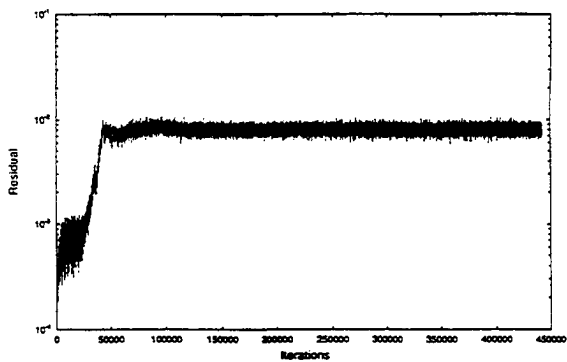
Figure A-3. Cobalt Residual History, Grid c-9
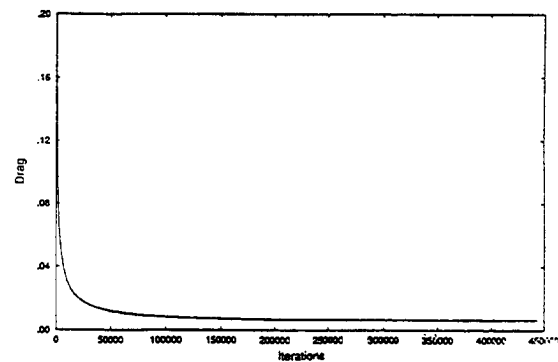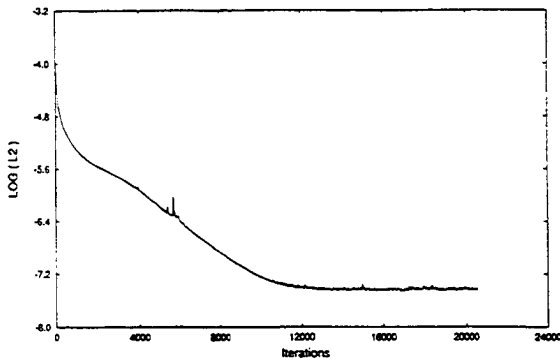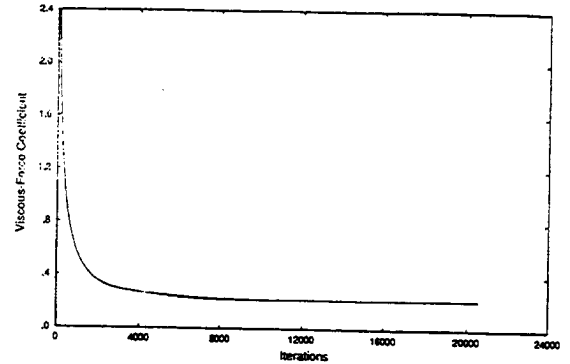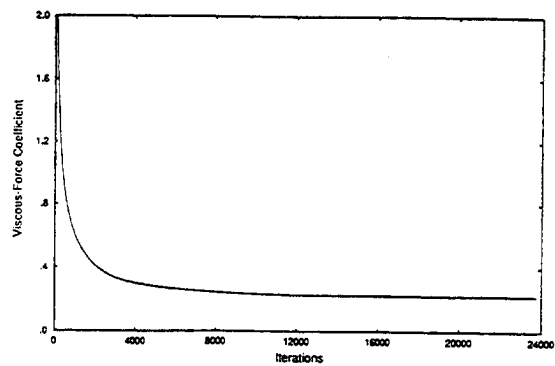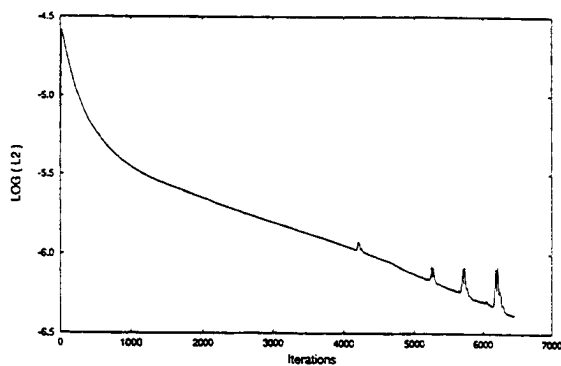

Figure A-4. Cobalt Force Convergence History, Grid c-9
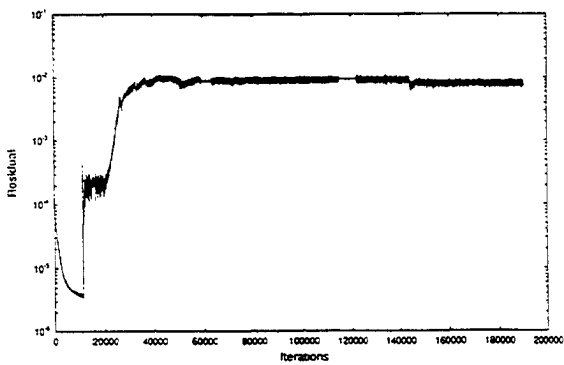
Figure A-9. Cobalt Residual History, Grid c-13
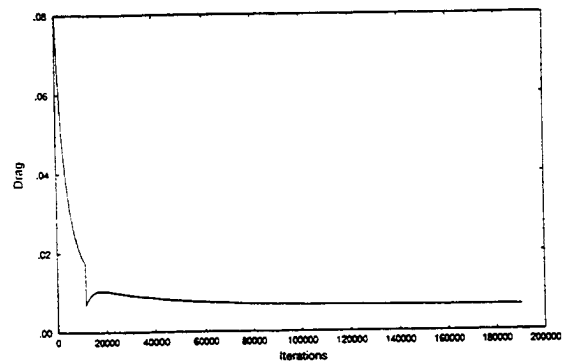
Figure A-10. Cobalt Force Convergence History, Grid c-13

65

Cobalt Flat Plate Solutions, Mach 0.1, Re=1.77x10^6, Turbulent Flow
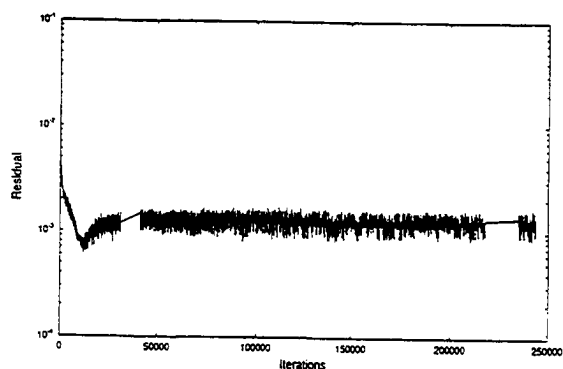
Figure A-11. Cobalt Residual History, Grid c-6
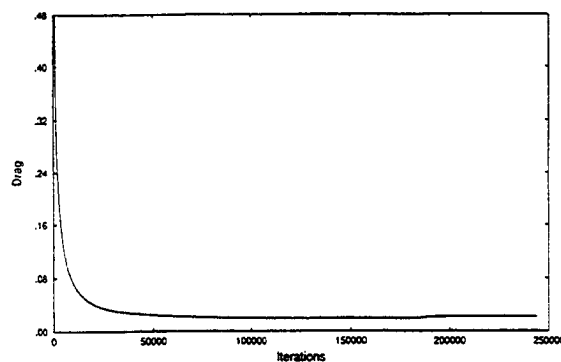
Figure A-12. Cobalt Force Convergence History, Grid c-6
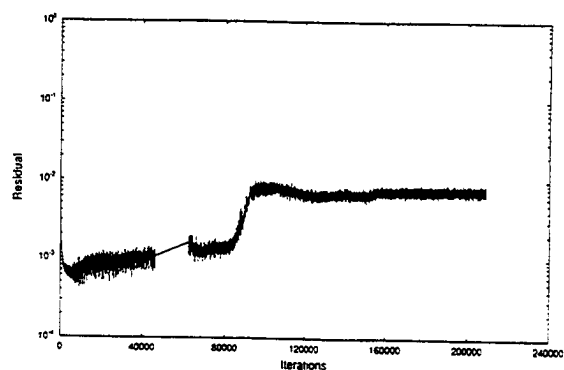
Figure A-13. Cobalt Residual History, Grid c-7
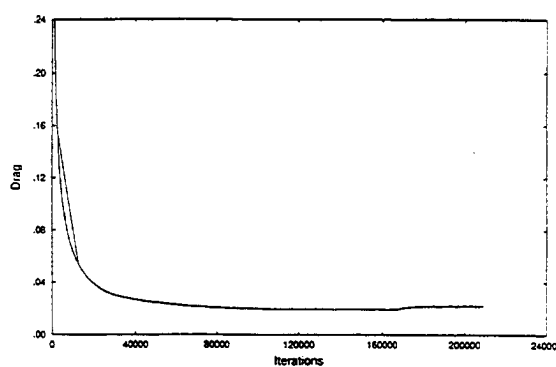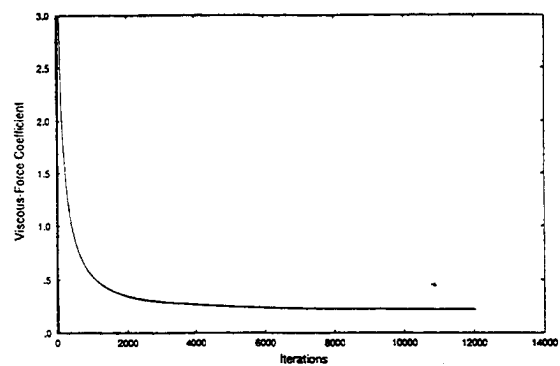

Figure A-14. Cobalt Force Convergence History, Grid c-7
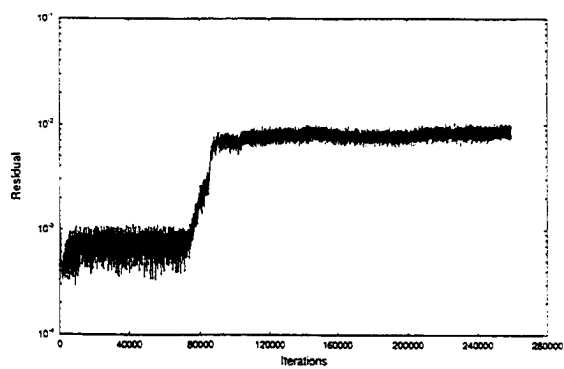
Figure A-15. Cobalt Residual History, Grid c-8
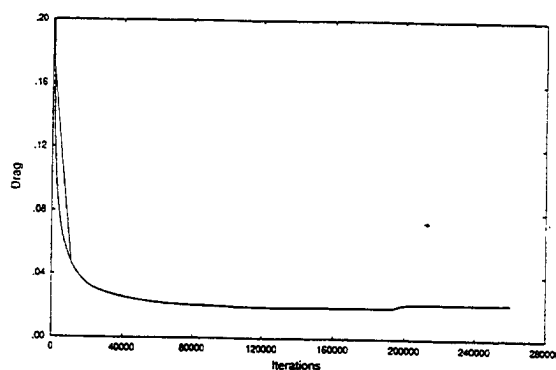
Figure A-16. Cobalt Force Convergence History, Grid c-8
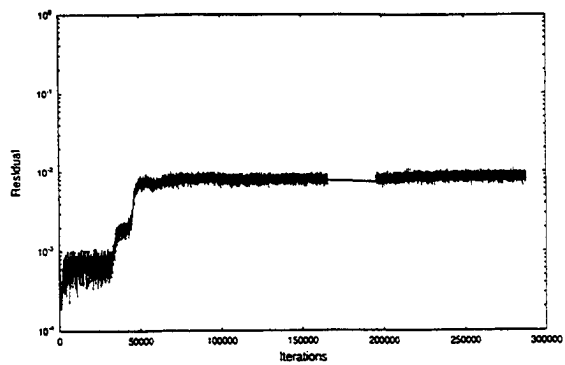
Figure A-17. Cobalt Residual History, Grid c-9
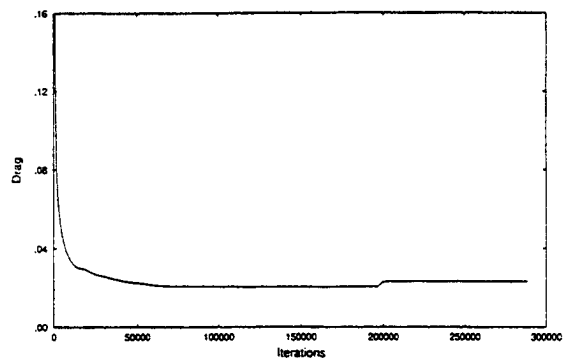
Figure A-18. Cobalt Force Convergence History, Grid c-9
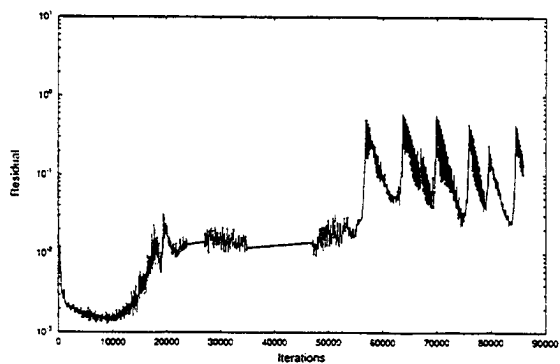
Figure A-19. Cobalt Residual History, Grid c-11
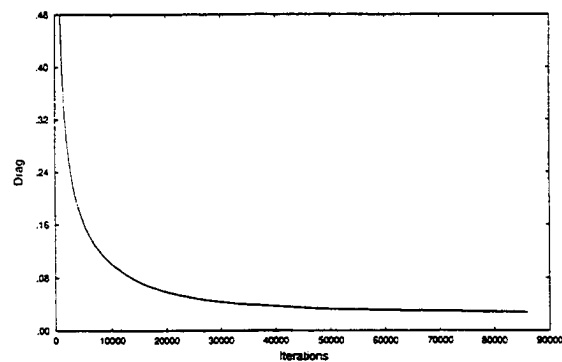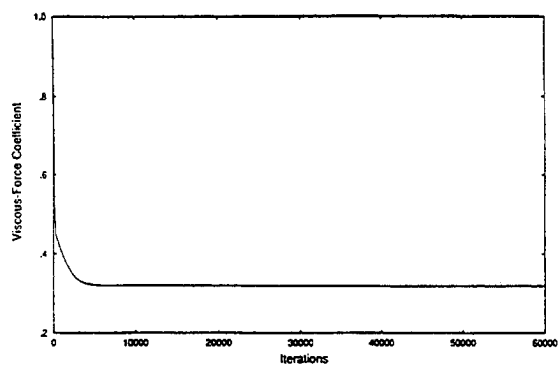

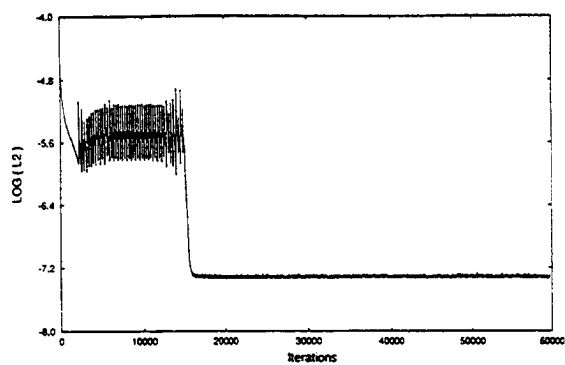Figure A-20. Cobalt Force Convergence History, Grid c-11
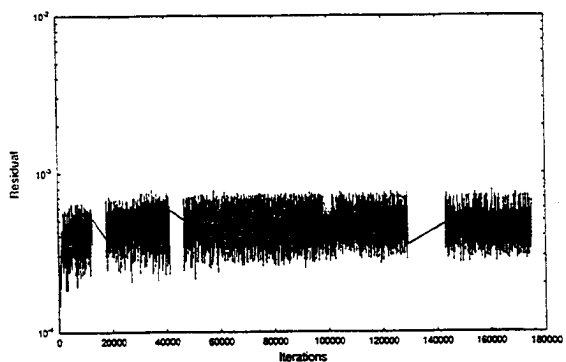
Figure A-21. Cobalt Residual History, Grid c-14
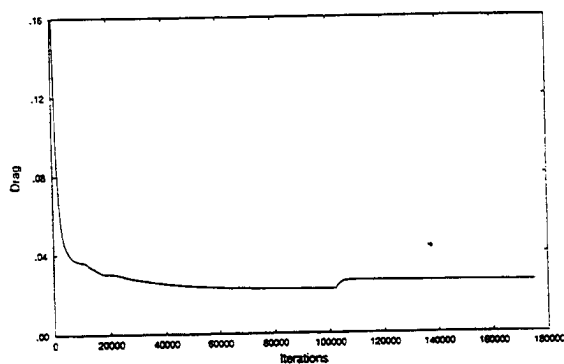
Figure A-22. Cobalt Force Convergence History, Grid c-14

67

# Cobalt Flat Plate Solutions, Mach 0.7, Re=12x10^6, Turbulent Flow
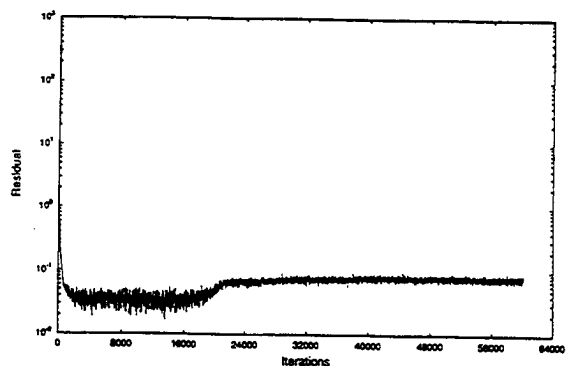
Figure A-23. Cobalt Residual History, Grid c-6
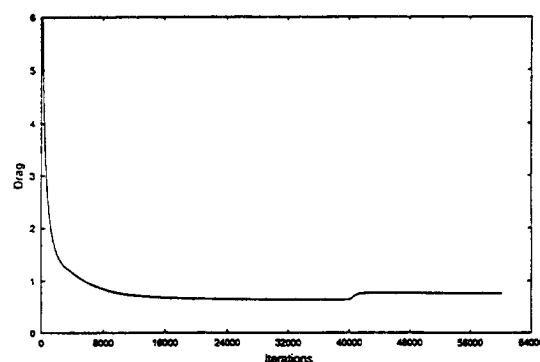
Figure A-24. Cobalt Force Convergence History, Grid c-6
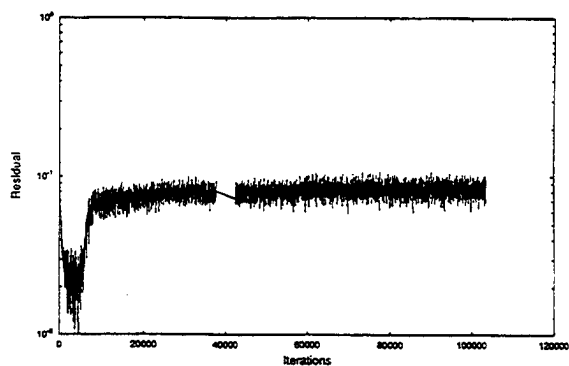
Figure A-25. Cobalt Residual History, Grid c-7
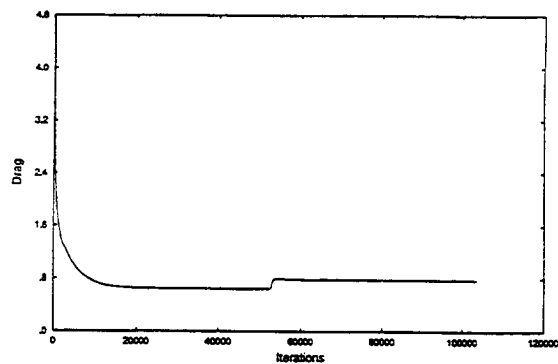
Figure A-26. Cobalt Force Convergence History, Grid c-7
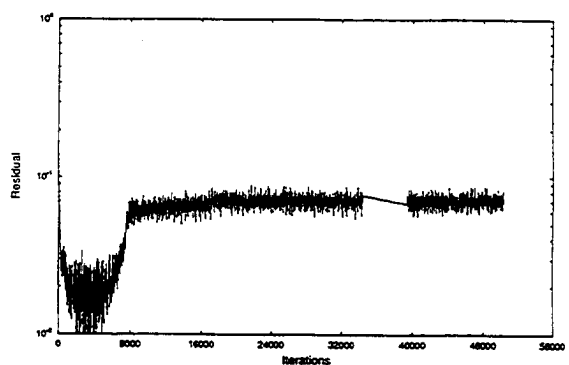
Figure A-27. Cobalt Residual History, Grid c-8
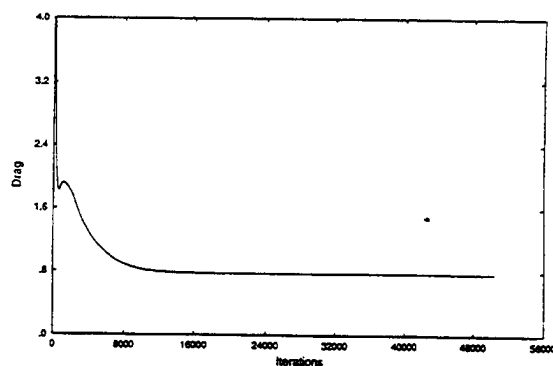
Figure A-28. Cobalt Force Convergence History, Grid c-8
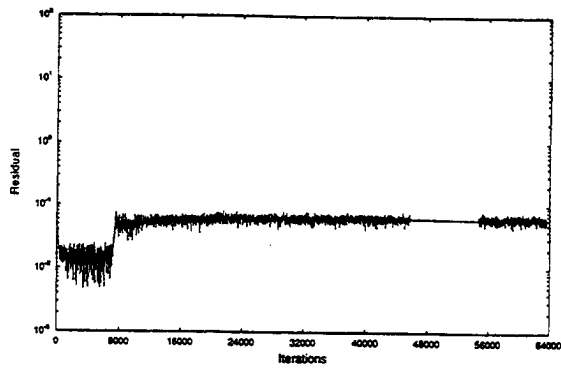
Figure A-29. Cobalt Residual History, Grid c-9
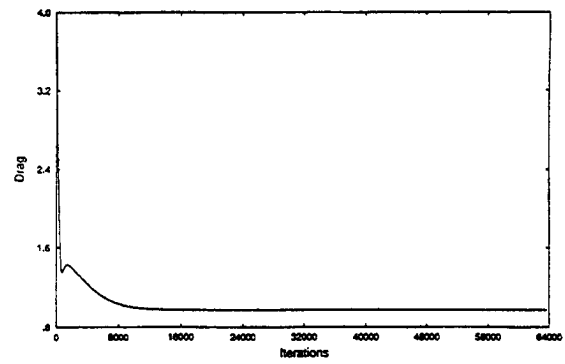
Figure A-30. Cobalt Force Convergence History, Grid c-9
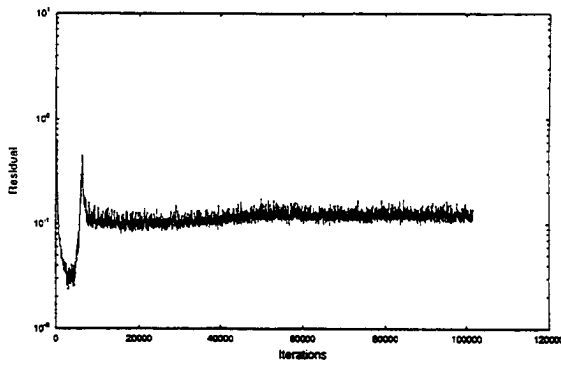
Figure A-31. Cobalt Residual History, Grid c-11
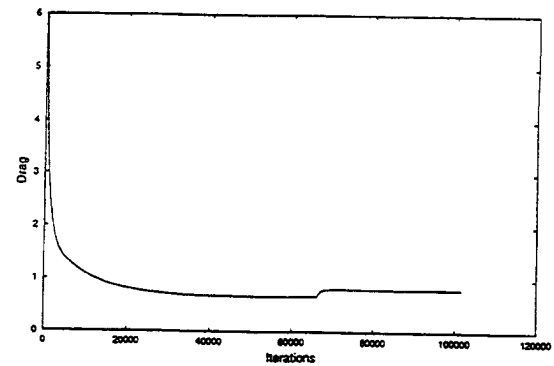
Figure A-32. Cobalt Force Convergence History, Grid c-11

Appendix B: NASTD Solution Convergence Plots

NASTD Flat Plate Solutions, Mach 0.1, Re=1.77x10^6, Laminar Flow
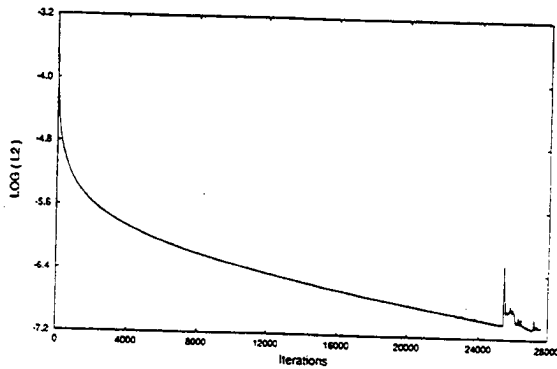
Figure B-1. NASTD Residual History, Grid n-6
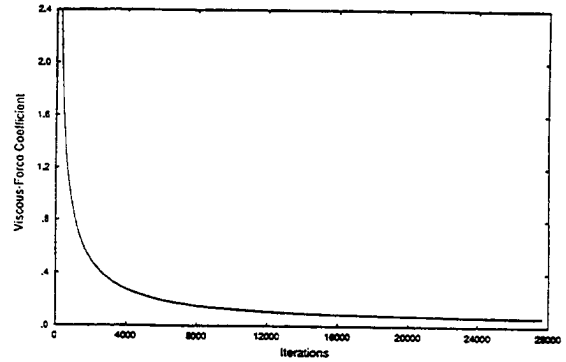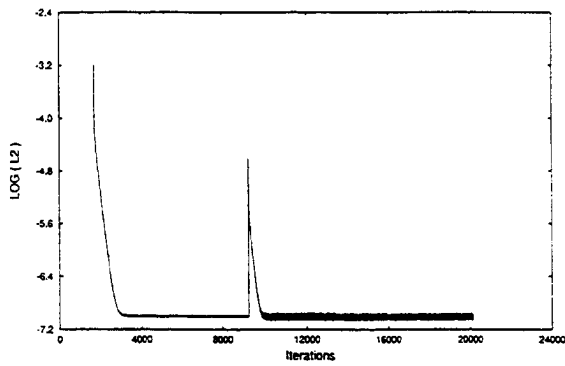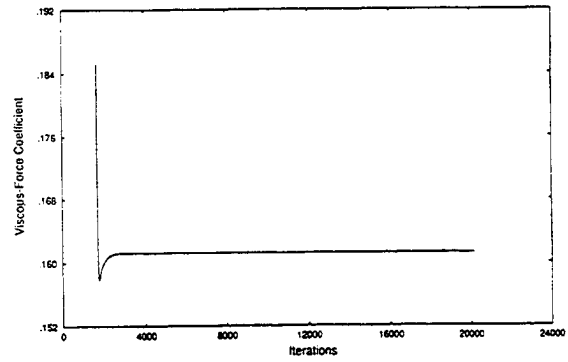

Figure B-2. NASTD Force Convergence History, Grid n-6
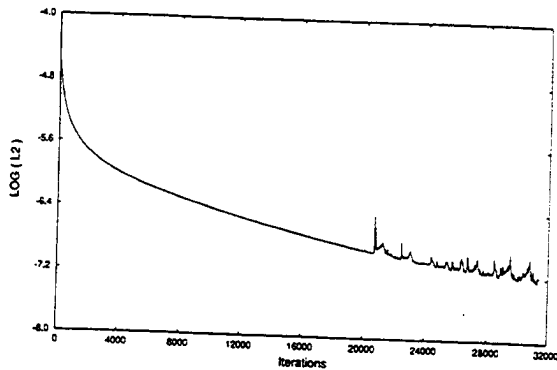
Figure B-3. NASTD Residual History, Grid n-9
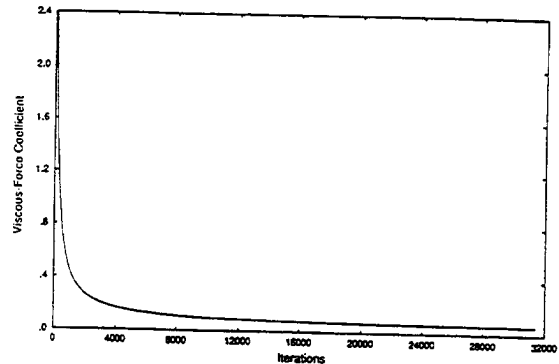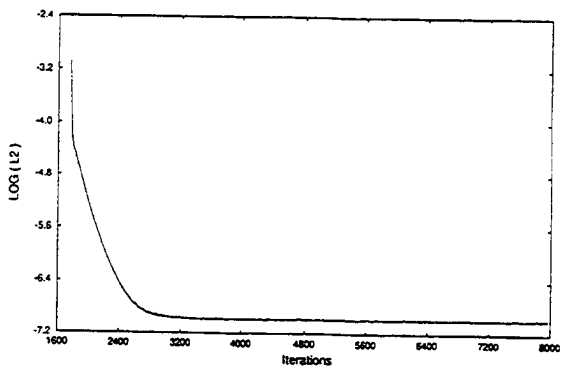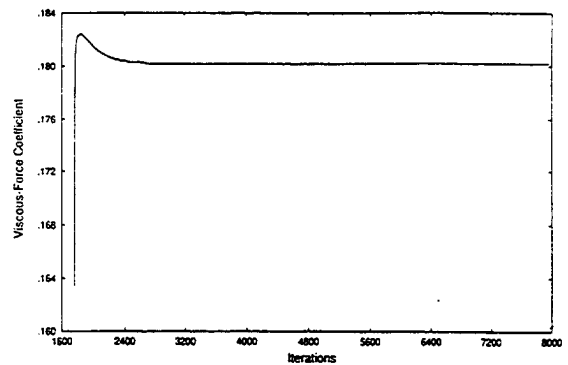

Figure B-4. NASTD Force Convergence History, Grid n-9
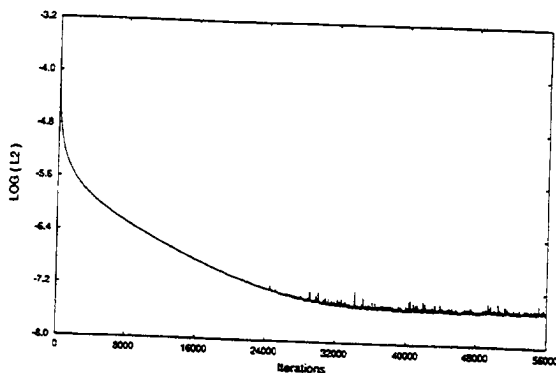
Figure B-5. NASTD Residual History, Grid n-11
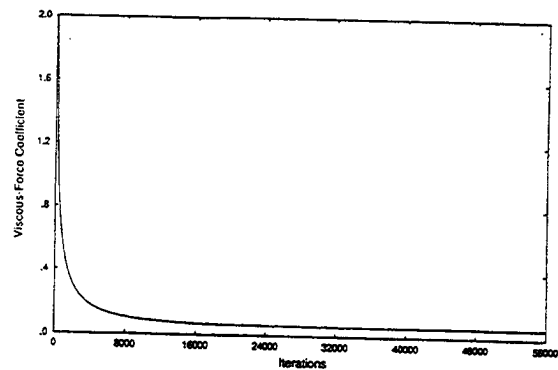
Figure B-6. NASTD Force Convergence History, Grid n-11

70
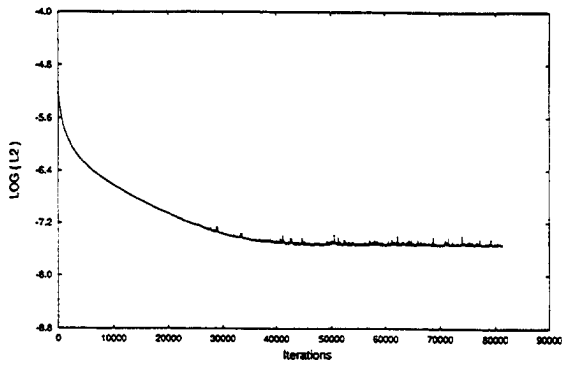
Figure B-7. NASTD Residual History, Grid n-12
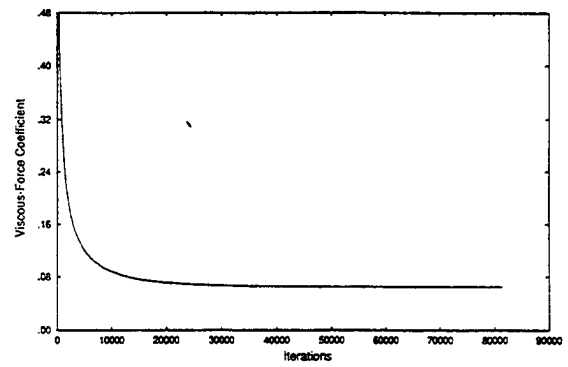
Figure B-8. NASTD Force Convergence History, Grid n-12
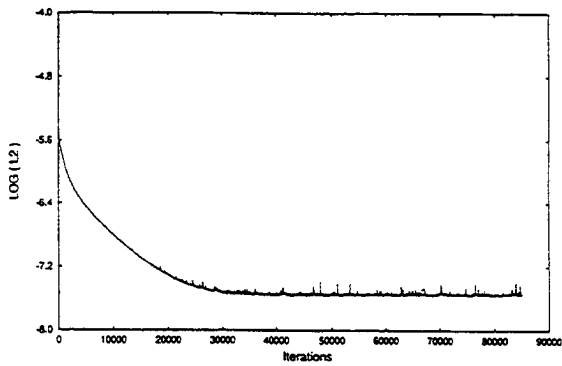
Figure B-9. NASTD Residual History, Grid n-13
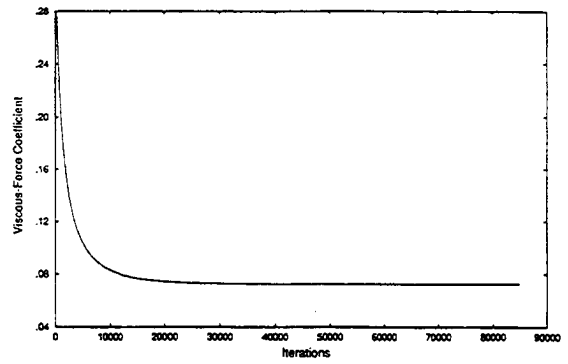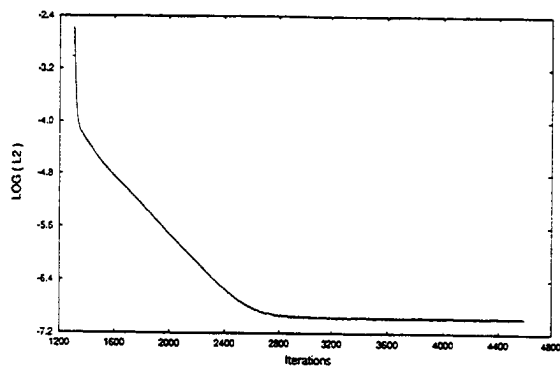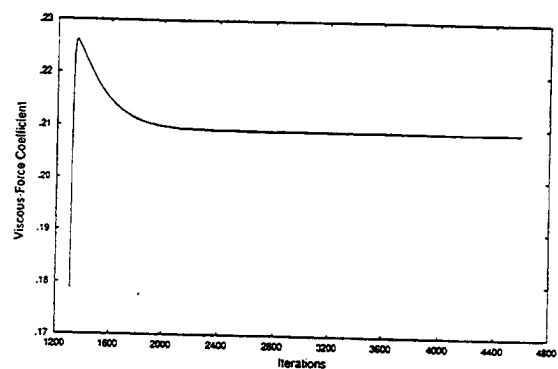

Figure B-10. NASTD Force Convergence History, Grid n-13

71

NASTD Flat Plate Solutions, Mach 0.1, Re=1.77x10⁶, Turbulent Flow
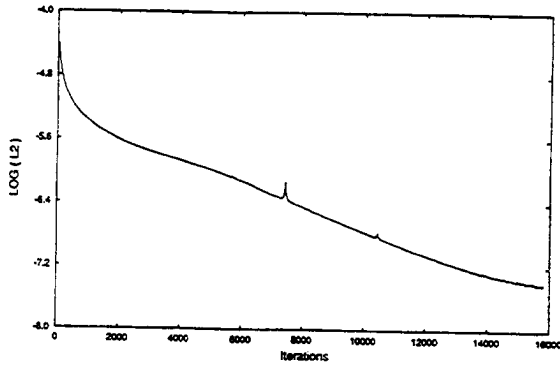
Figure B-11. NASTD Residual History, Grid n-4
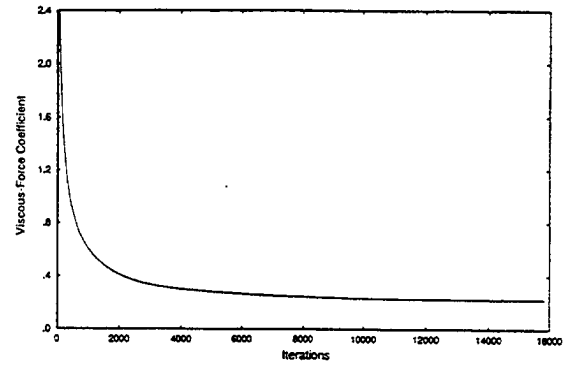
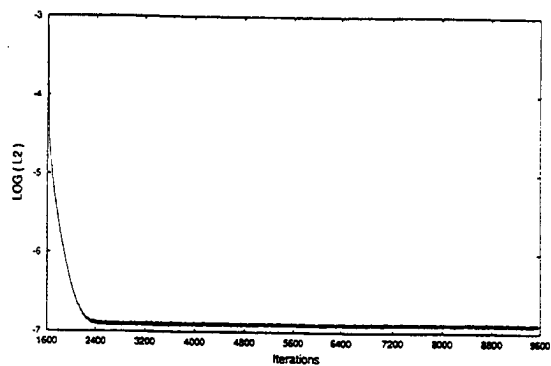Figure B-12. NASTD Force Convergence History, Grid n-4
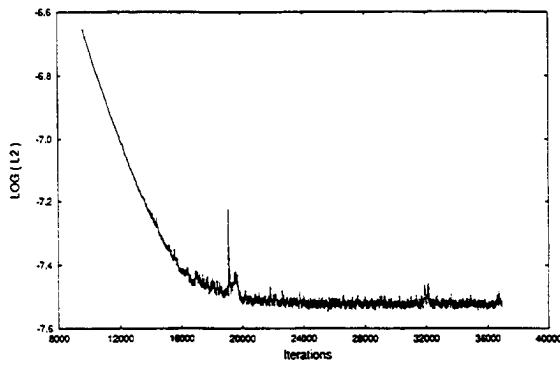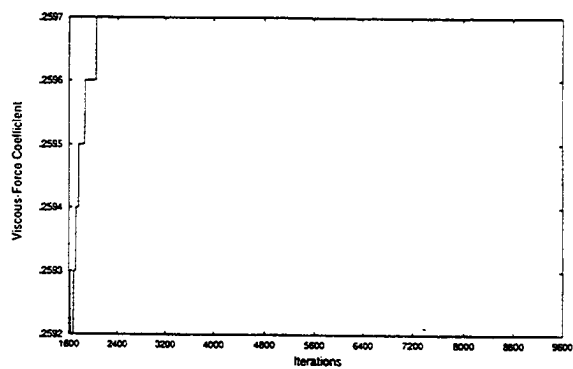

Figure B-13. NASTD Residual History, Grid n-6
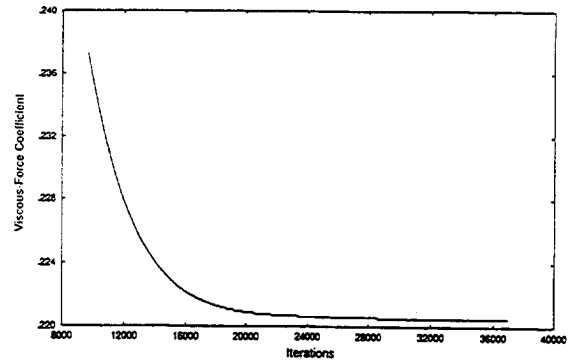
Figure B-14. NASTD Force Convergence History, Grid n-6

Figure B-15. NASTD Residual History, Grid n-7

Figure B-16. NASTD Force Convergence History, Grid n-7
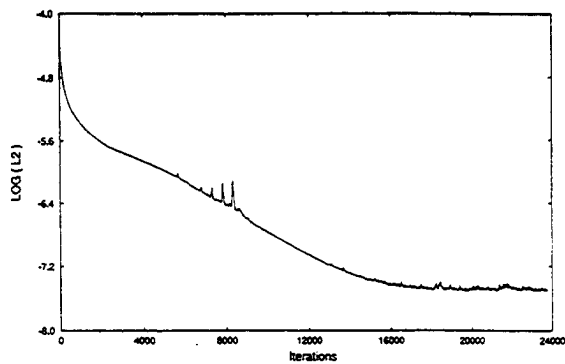
Figure B-17. NASTD Residual History, Grid n-8

Figure B-18 .NASTD Force Convergence History, Grid n-8

Figure B-19. NASTD Residual History, Grid n-9
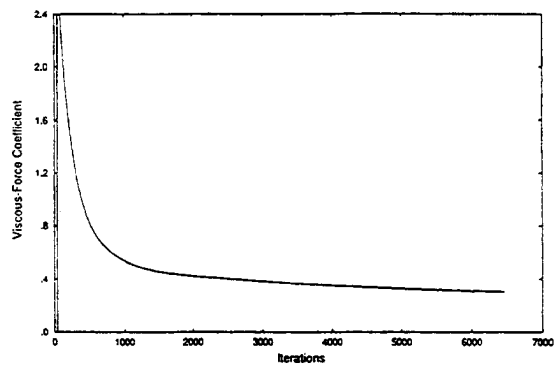
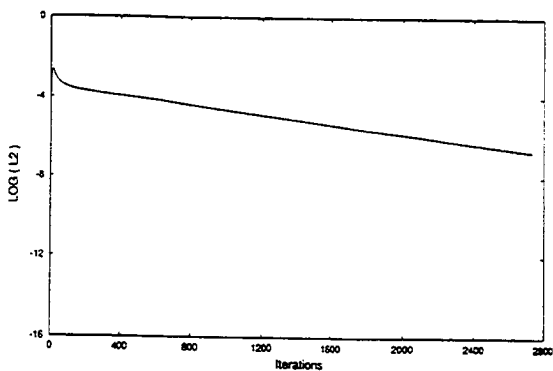Figure B-20. NASTD Force Convergence History, Grid n-9
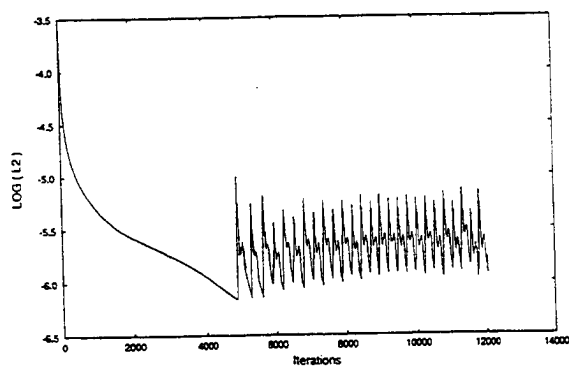

Figure B-21. NASTD Residual History, Grid n-11

Figure B-22. NASTD Force Convergence History, Grid n-11

73

Figure B-23. NASTD Residual History, Grid n-14 Figure B-24. NASTD Force Convergence History, Grid n-14

NASTD Flat Plate Solutions, Mach 0.7, Re=12x10⁶, Turbulent Flow
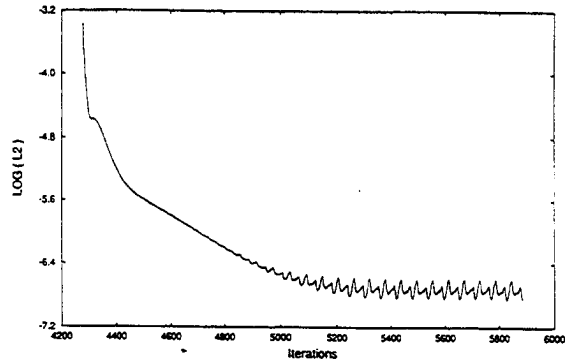
Figure B-25. NASTD Residual History, Grid n-2
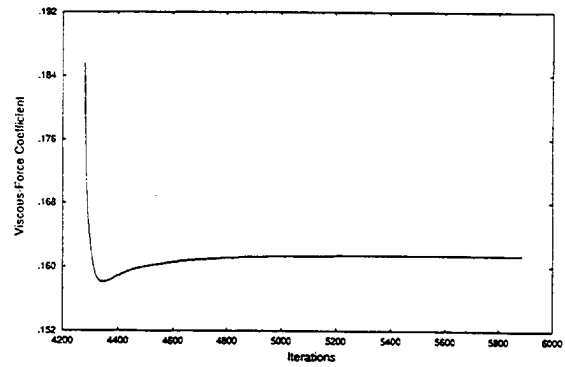
Figure B-26. NASTD Force Convergence History, Grid n-2

Figure B-27. NASTD Residual History, Grid n-6

Figure B-28. NASTD Force Convergence History, Grid n-6

Figure B-29. NASTD Residual History, Grid n-7

Figure B-30. NASTD Force Convergence History, Grid n-7

Figure B-31. NASTD Residual History, Grid n-8

Figure B-32. NASTD Force Convergence History, Grid n-8

Figure B-33. NASTD Residual History, Grid n-9

Figure B-34. NASTD Force Convergence History, Grid n-9

Figure B-35. NASTD Residual History, Grid n-11
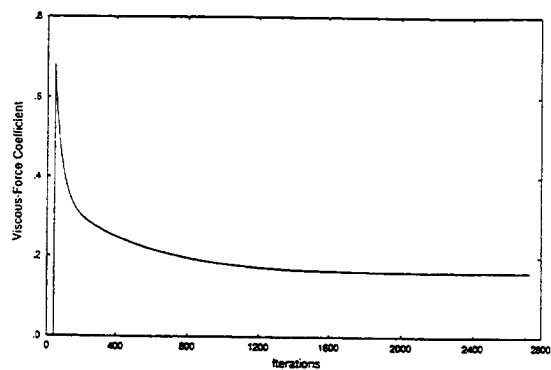
Figure B-36. NASTD Force Convergence History, Grid n-11

76

Appendix C: USM3D Solution Convergence Plots

USM3D Flat Plate Solutions, Mach 0.1, Re=1.77x10^6, Laminar Flow
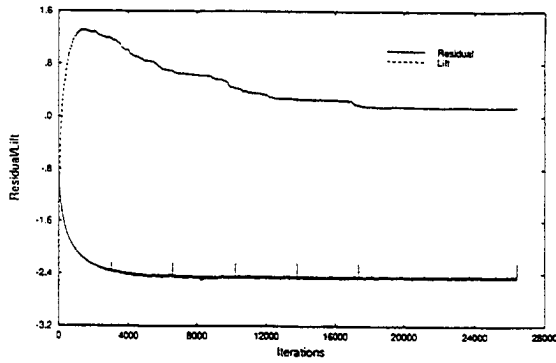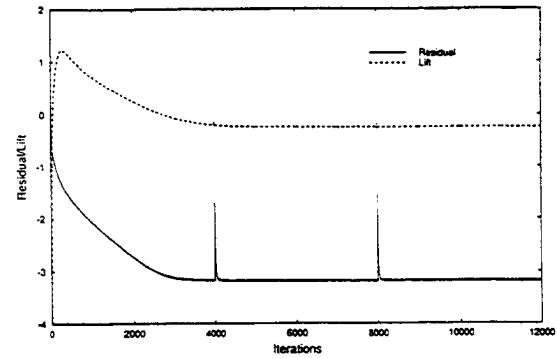

Figure C-1. USM3D Convergence History, Grid u-3

Figure C-2. USM3D Convergence History, Grid u-6

USM3D Flat Plate Solutions, Mach 0.1, Re=1.77x10^6, Turbulent Flow
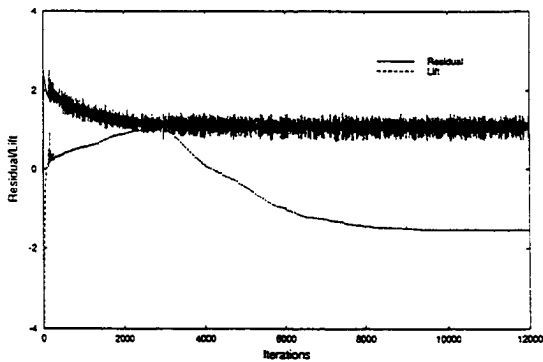
Figure C-3. USM3D Convergence History, Grid u-2

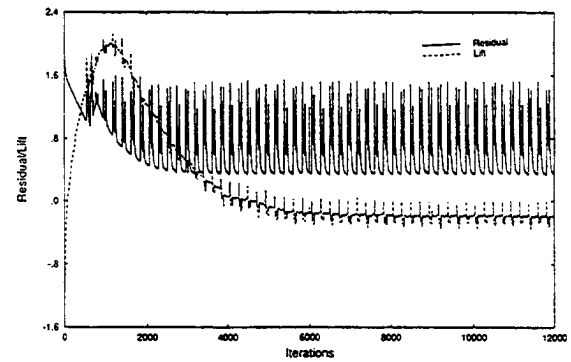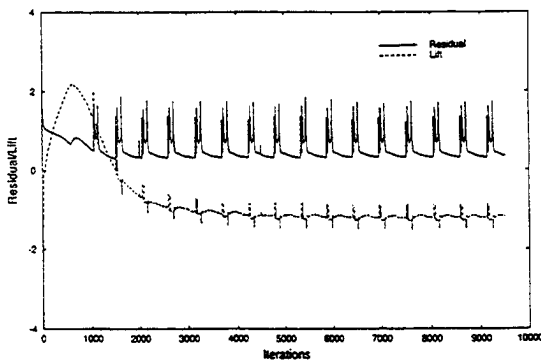Figure C-4. USM3D Convergence History, Grid u-3

Figure C-5. USM3D Convergence History, Grid u-4
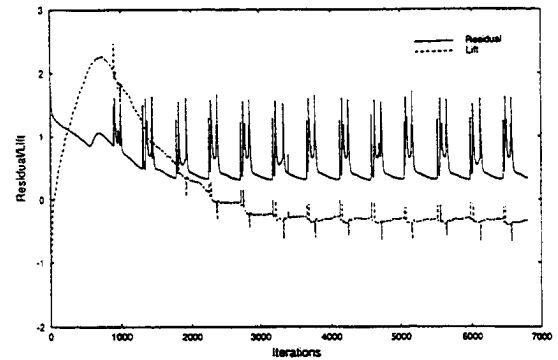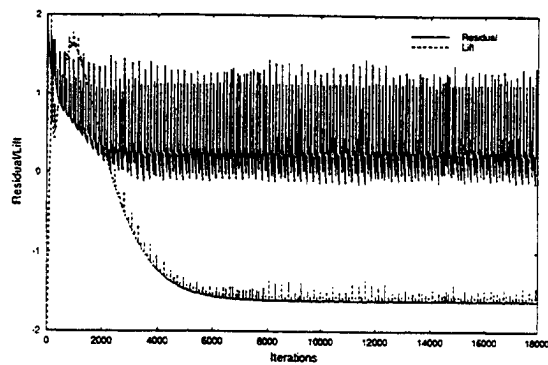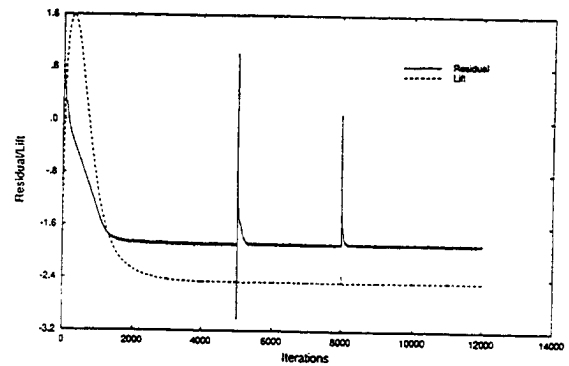

Figure C-6. USM3D Convergence History, Grid u-5

77

USM3D Flat Plate Solutions, Mach 0.7, Re=12x10⁶, Turbulent Flow

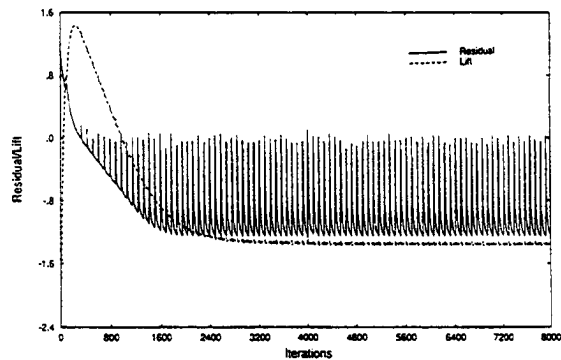Figure C-7. USM3D Convergence History, Grid u-1

Figure C-8. USM3D Convergence History. Grid u-3

Figure C-9. USM3D Convergence History, Grid u-6